Computer Aided Medical Procedures
(CAMP)
Prof. Dr. Nassir Navab

Dissertation

Improvement and Automatic Classification of IVUS-VH (Intravascular Ultrasound – Virtual Histology) Images

Arash Taki

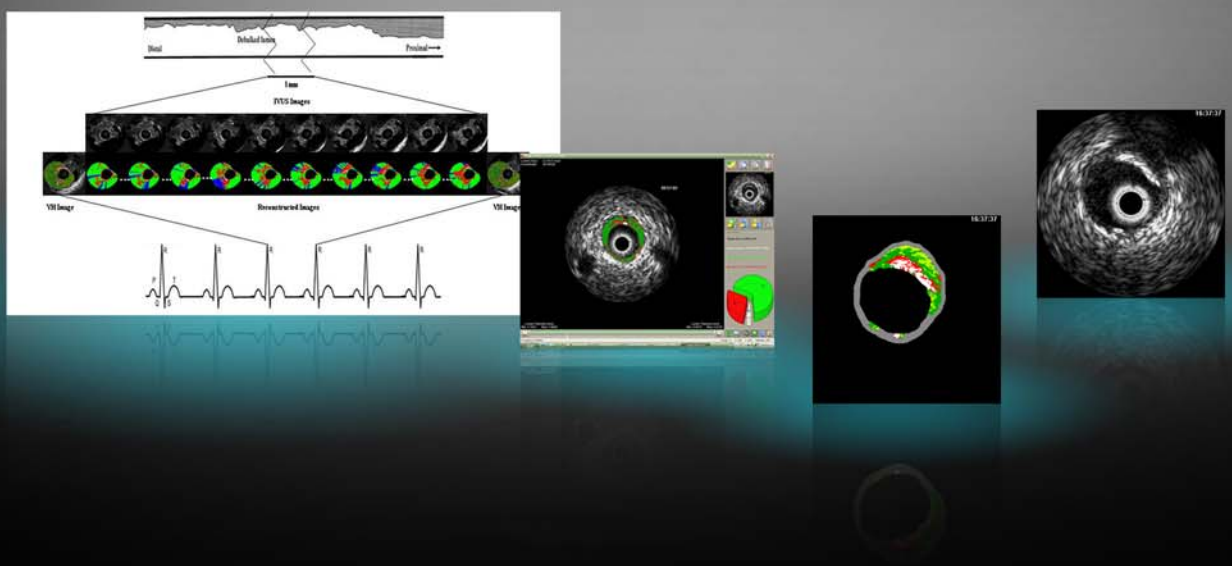

Fakultät für Informatik
Technische Universität München

TECHNISCHE UNIVERSITÄT MÜNCHEN

Chair for Computer-Aided Medical Procedures & Augmented Reality

Improvement and Automatic Classification of IVUS-VH (Intravascular Ultrasound – Virtual Histology) Images

Arash Taki

Vollständiger Abdruck der von der Fakultät für Informatik der Technischen Universität München zur Erlangung des akademischen Grades eines

Doktors der Naturwissenschaften (Dr. rer. nat.)

genehmigten Dissertation.

Vorsitzende: Univ.-Prof. Gudrun J. Klinker, Ph.D

Prüfer der Dissertation:

1. Univ.-Prof. Nassir Navab, Ph.D.
2. Assoc. Prof. S. Kamaledin Setarehdan, Ph.D.
   University of Tehran, Iran
3. Asst. Prof. Gozde Unal, Ph.D.
   Sabanci University Istanbul, Türkei

Die Dissertation wurde am 17.02.2010 bei der Technischen Universität München eingereicht und durch die Fakultät für Informatik am 18.08.2010 angenommen.

Acknowledgments

I would like to express my sincere gratitude to my PhD adviser Professor Dr. Navab for his guidance, support and encouragement during this research, as well as my entire period of studies at Technical University of Munich.

I am deeply grateful to Dr. Unal and Dr. Setarehdan, my supervisor at university of Tehran, for their invaluable support, creative ideas, detailed and constructive comments, throughout this research. The latter has been a source of inspiration throughout my post-graduate studies.

My thanks goes to Dr. Rieber and most importantly Dr. König, who were the motivating factor in choosing my subject matter and had a remarkable influence in this work; their generosity to share their data will long be remembered.

During this work I have collaborated with many colleagues, for whom I have deepest respect and, therefore, wish to extend my warmest thanks to Reza Mousavi, Olivier Pauly, Amin Katouzian, Ali Bigdelou and Holger Heterrich who all helped with their detailed reviews, constructive criticism and fruitful discussions.

Special thanks go to Sara Avansari and Alireza Roodaki for their sympathetic help and valuable input in this work.

Furthermore, I would like to thank Martina Hilla, for all her cooperation during my PhD program.

I would also like to thank to my sister and her husband, Elham and Dr Alireza Omrani, and specially my brother, Salar, who have supported me during my years of studies.

Last, but not least, I owe especial thanks to my parents for their patience and support during this thesis. Their understanding and support has been exceptional and I feel forever indebted.

Without any of the above this thesis would not have been completed.

Abstract

Heart attack and stroke are the major causes of human death and atherosclerotic plaques are the most common effect of cardiovascular disease. Intravascular ultrasound (IVUS), a diagnostic imaging technique, offers a unique view of the morphology of the arterial plaque and displays the morphological and histological properties of a cross-section of the vessel. Limitations of the grayscale IVUS manual plaque assessment have led to the development of quantitative techniques for analysis of characteristics of plaque components.

In vivo plaque characterization with the so called Virtual Histology (VH)-IVUS, which is based on the ultrasound RF signal processing, is widely available for atherosclerosis plaque characterization in IVUS images. However, it suffers from a poor longitudinal resolution due to the ECG-gated acquisition. The focus of this PhD thesis is to provide effective methods for image-based vessel plaque characterization via IVUS image analysis to overcome the limitations of current techniques. The proposed algorithms are also applicable to the large amount of the IVUS image sequences obtained from patients in the past, where there is no access to the corresponding radio frequency(RF) data. Since the proposed method is applicable to all IVUS frames of the heart cycle, it outperforms the longitudinal resolution of the so called VH method.

The procedures of analyzing grayscale IVUS images can be divided into two separated aspects: (i) detecting the vessel borders to extract the region called "plaque area". (ii) characterizing the atherosclerosis plaque composition. The latter one consists of two main steps: in the first one, known as feature extraction, the plaque area of the cross-sectional IVUS image is modeled using appropriate features. The second step based on learning techniques assists the classifier in distinguishing different classes more precisely and in assigning labels to each of the samples generated by feature extraction within the first step.

In-vivo and *ex-vivo* validation procedures were used, where the results proved the efficiency of the proposed algorithms for vessel plaque characterization via IVUS images. A graphic user interface (GUI) is designed as an effective image processing tool which enables cardiologists with a complete IVUS image processing tool from border detection to plaque characterization. The algorithms developed within this thesis leads to the enhancement of the longitudinal resolution of plaque composition analysis. In the final part of the thesis, this is shown analytically and is highlighted by presenting a three dimensional view of both the vessel and the distribution of different plaque components in the plaque area.

Keywords:

IVUS, Plaque Component Analysis, Longitudinal Resolution, Virtual Histology

Zusammenfassung

Herzinfarkte und Herzrhythmusstörungen sind die häufigste Todesursache und Arteriosklerose (Arterienverkalkung) ist die häufigste Ursache für Herzerkrankungen. Intravaskulärer Ultraschall (IVUS), eine diagnostische Bildgebung, bietet eine gute Betrachtung der Morphologie der Verkalkungen. Des Weiteren stellt es die histologischen und morphologischen Eigenschaften der Gefäßverbindungen dar. Die Limitation der manuellen Detektion in den IVUS Graustufenbilder führte zu der Entwicklung von quantitativen Methoden um die Ablagerungscharakteristik zu bestimmen.

Die in-vivo Verkalkungscharakterisierung mit der Virtual Histology (VH)-IVUS Technik basiert auf der Signalverarbeitung von RF Ultraschall und ist weit verbreitet für die Arterioskleroseanalyse. Eine große Limitation ist jedoch die Auflösung in axialer Richtung auf Grund der EKG synchronisierten Phasenaufnahmen. Das Kernthema dieser Dissertation ist es eine effektive Methode für die Charakterisierung der Gefäßverkalkungen mittels IVUS Bilddaten zu erforschen, um die herkömmlichen Analysemethoden zu verbessern. Der vorgeschlagene Algorithmus ist auch auf eine große Anzahl von retrospektiven Patinetendaten anwendbar, bei denen es noch keinen Zugriff auf die RF Technik gab. Da die Methode auf alle IVUS Bilder eines Herzzyklus anwendbar ist hat sie gegenüber den herkömmlichen Methoden der Virtual Histology einen klaren Vorteil in der axialen Auflösung.

Das Verfahren der Analyse der graustufen IVUS Bilder kann in zwei Aspekte untergliedert werden: (i) Erkennung der Gefäßgrenzen um die Verkalkungsfläche zu extrahieren und (ii) die Charakterisierung der Zusammensetzung der Verkalkung. Die Charakterisierung der Verkalkung geschieht in zwei Schritten: Im ersten Schritt, auch bekannt als Mustererkennung, wird die Ablagerungsfläche in den IVUS Schnittbildern mit entsprechenden Mustern modelliert. In einem zweiten Schritt wird nach einer Lernphase detailliert zwischen verschiedenen Klassen unterschieden und den Proben entsprechend markiert.

In einer Ex-vivo und in-vivo Validierung wurde die Methode auf Ihre Effektivität bei der Charakterisierung der Verkalkungen geprüft. Eine Benutzerschnittstelle wurde entworfen um die Bildbearbeitung für Kardiologen von der Formerkennung bis hin zur Verkalkungsanalyse effektiv darzustellen. Die in dieser Dissertation entwickelten und evaluierten Algorithmen führten zu einer Verbesserung in der axialen Auflösung bei der Verkalkungsanalyse. In dem letzten Kapitel wurde analytisch gezeigt, dass sowohl die Gefäßstruktur, als auch die Verteilung der Verkalkungen in drei Dimensionen angezeigt werden konnte.

Schlüsselwörter:

IVUS, Verkalkungsanalyse, Axiale Auflösung, Virtual Histology

Contents

Outline of the Thesis

This thesis is subdivided into five sections that consist of the following chapters :

CHAPTER 1: MEDICAL BACKGROUND

An introduction to medical basics is focused in this work and the clinical applications of several medical imaging modalities, esp. IVUS and Virtual Histology, used for atherosclerotic plaque assessment followed by a description of problem statement.

CHAPTER 2: TECHNICAL PRINCIPLES OF IVUS

A general review of ultrasound physics and technical principals of IVUS imaging.

CHAPTER 3: PLAQUE AREA DETECTION

A review of existing techniques for border detection and an introduction to algorithms employed in this work.

CHAPTER 4: STATE OF THE ART IN PLAQUE CHARACTERIZATION

A review of previous techniques used for IVUS plaque characterization.

CHAPTER 5: NEW APPROACHES FOR PLAQUE COMPONENT ANALYSIS

Four new algorithms presented based on image texture analysis methods for characterization of coronary plaque composition via IVUS images.

CHAPTER 6: VALIDATION

Implementing *in-vivo* and *ex-vivo* validation procedures and also presenting the enhancement of the longitudinal resolution of plaque composition analysis.

CHAPTER 7: CONCLUSION AND FUTURE WORK

A short summary followed by a discussion of four proposed algorithms for plaque analysis and future works.

Appendix

A. LIST OF PUBLICATIONS

All publications contributed to the scientific community during this work.

B. LIST OF ABBREVIATIONS

C. QUANTITATIVE ANALYSIS FOR CLINICAL REPORTS OF IVUS IMAGING

1. Chapter One: Medical Background

1.1. Biological Concerns

Despite significant advances in diagnosis and treatment, coronary atherosclerosis remains a major cause of death in developed countries [87] and almost twice as many people die from cardiovascular diseases than from all forms of cancer combined.

1.1.1. Biological Background

The coronary arteries are the vessels which supply the heart muscle with blood and therefore oxygen. The right coronary artery and the left main coronary artery are the two branches that come from the aorta to feed the back of the heart and its front respectively (figure 1.1). The left main coronary artery further splits up in the left anterior descending(LCD) and the left circumflex(LCX), to supply with blood the front of the heart and the left side and back of the heart [99].

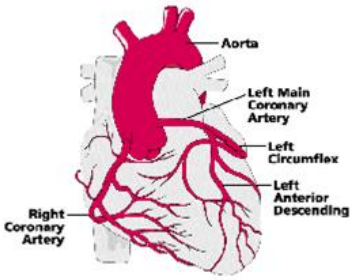

Figure 1.1.: Coronary arteries [99].

These coronary arteries mainly consist of three layers. The inner layer is intima, the middle layer is media, and the outer one is adventitia. These layers are observable in a cross-section of the artery (figure 1.2). Media consists of smooth muscle cells, with an approximate thickness of 100 microns. The adventitia is made up of mostly elastic and collagen fibers and fibroblasts. The intima has a variable thickness which is expressed as a ratio of media thickness. Ratios of 0.1 to 1 are considered normal [98].

1.1.2. Coronary Artery Disease

Atherosclerotic plaques are the most common effect of cardiovascular disease. Atherosclerotic plaques can either cause stable coronary artery stenosis leading to angina pectoris

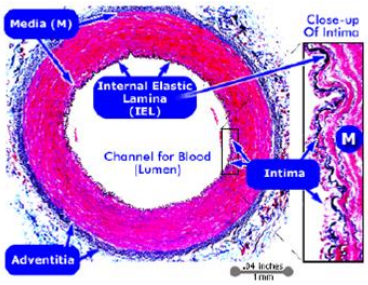

Figure 1.2.: Cross-section of a coronary artery which shows intima, media, and adventitia layers [88].

during exercise, or lead to acute coronary or vascular events such as myocardial infarction or stroke when they rupture.

The development of atherosclerotic lesions can be categorized in six classes based on the definition of the Committee on Vascular Lesions of the Council on Atherosclerosis of the American Heart Association[93]. Classes I-III are considered precursors of an established lesion and had already been seen in children and adolescents. Types IV-VI are classified as advanced atherosclerotic lesions [93].

Atherosclerosis takes place due to an activated endothelium, mainly in areas with pre-existing intima thickening. An activated endothelium is characterized by a raised adhesiveness for monocytes due to over-expression of adhesion molecules, an enhanced permeability to lipoproteins or functional imbalances of pro- and anti-thrombotic factors, growth stimulators and inhibitors, and vasoactive substances.

1.1.3. Lesions Associated with Coronary Artery Disease

There are different types of plaques responsible for causing coronary atherosclerosis. For years, rupture of vulnerable plaques was addressed as the most important sources of coronary thrombosis. But other types of plaques and lesions also exist in the literature [91]. Three different plaque etiologies associated with coronary thrombosis is shown in table 1.1. In the following sections these lesions will be discussed in detail.

Rupture of Vulnerable Plaque

The rupture of vulnerable plaques is the main cause of acute coronary syndrome [91], [92]. Acute Coronary Syndrome (ACS) (or Myocardial Infarction (AMI) /unstable angina) occurs when the supplied oxygen from the coronary arteries is less than the myocardial demand. It usually happens due to atherosclerotic coronary artery disease (CAD). In this case, when the atheromatous plaque builds up on the wall of the coronary arteries, the lumen of the artery will be probably compromised.

Stenotic plaques which compromise the coronary arteries luminal surface area by more than 60-70 percent used to be clinically significant and hence, a patient with this condition used to be marked as high risk for ACS. However, many researches have shown that in some cases the AMI occurs due to the occlusion of coronary arteries without any significant stenosis. It means sometimes plaques causing severe stenosis are not the cause of

Table 1.1.: Lesions Associated with Coronary Thrombi

Lesions Associated with Coronary Thrombi	**Characteristics**
Plaque Rupture	A necrotic Lesion with a luminal thrombus containing core encapsulated by a thin fibrous cap infiltrated by macrophages and T cells.
Plaque Erosion	Thrombosed arterial segment without an area of rupture.
Calcified Nodule	Fibrous-rich calcified lesion with little or no necrotic core containing a luminal thrombus without obvious rupture of the lesion.

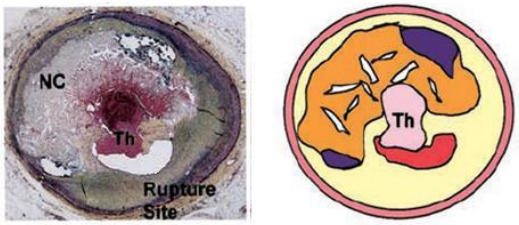

Figure 1.3.: Rupture of vulnerable plaque [92].

AMI [2].
The plaque at a high risk of rupturing was suggested by the researchers in place of stenosis plaque as the immediate precursor of most of the culprit plaques for ACS stenotic [42]. This, indeed, was the first step in the development of the concept of Vulnerable Plaque (VP). The VP is the ”short-term precursor” to the culprit plaque, which triggers clinical ACS.
Although the lipid core encased in fibrous ”cap” plaques may compromise the lumen of the coronary, based on histopathological studies of ”culprit” plaques, approximately 60 to 70 percent of AMIs are caused by plaque rupture, with release of the thrombogenic core of lipid and necrotic debris [17] , [22]. Based upon these findings, VPs are defined as plaques at high risk for rupture, or for having the surface of their fibrous cap denuded in either case leading to thrombus formation. This may weaken the routine method of clinical decision-making based on determining the stenosis because it would be unreliable due to an ignoring of the major cause of AMI. VPs are supposed to have three histologic hallmarks compared to stable ones: a larger lipid core, a thinner fibrous, and many inflammatory cells.
In addition to the above definition, VP can be described as any plaque that might cause clinically significant CAD. In this definition, any plaque vulnerable to rupture or denudation is defined as VP. While covering the previous definition of VP, many other plaques are

marked as VP (figure 1.4).

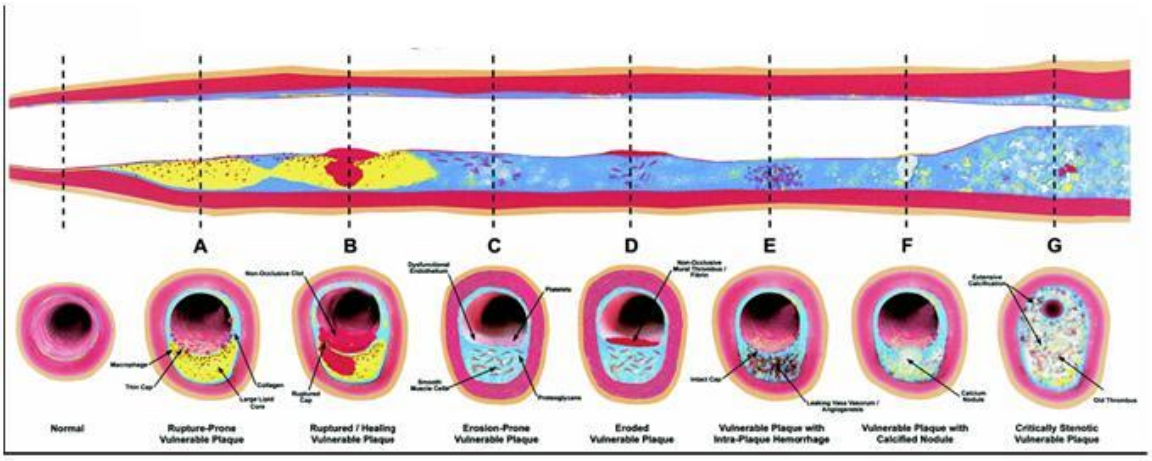

Figure 1.4.: Different types of vulnerable plaque [45].

Plaque A is the main cause of culprit lesions and represents the previous definition of VP [45]. To complete the definition, VP criteria are expanded as follows: Major criteria include: active inflammation (monocyte/macrophage +/- Tcell infiltration), thin cap with large lipid core, endothelial denudation with superficial platelet aggregation, fissured plaque, and more than 90 percent stenosis. Minor criteria include: superficial calcified nodule, glistening yellow appearance, intraplaque hemorrhage, endothelial dysfunction, and outward (positive) remodeling.
Plaque Erosion: Plaque erosion is referred when a thrombosed arterial segment fails to show an area of rupture after serial sectioning [91]. The exposed intima at the plaque thrombus interface consists predominantly of smooth muscle within a proteoglycan-rich matrix with minimal inflammation. Typically, the endothelium is absent at the erosion site. The development of erosion may be the sequel to repeated episodes of focal vasospasm; however, to date, there has been no direct evidence to support this hypothesis.

Calcified Nodule: This term refers to a fibrous-rich calcified lesion with little or no necrotic core containing a luminal thrombus without obvious rupture of the lesion [91], [93]. There are superficial, dense, calcified nodules within the intima, which appear to be erupting through fibrous tissue into the lumen, possibly causing the thrombus. The calcified nodules are associated with osteoclast-like cells.

Thin Cap Fibroatheroma (TCFA): TCFA is defined by a lesion composed of a lipid-rich core in the central portion of an eccentric plaque. The central core contains many lipid-laden macrophage foam cells derived from blood monocytes in a thin, friable fibrous cap. To be more specific, TCFA can be further defined as a lesion containing a fibrous cap less than $65mm$ thick and infiltrated by macrophages. The $65mm$ thickness in cases of vulnerable plaque was chosen as a criterion of vulnerability because of arteries with ruptured plaque.

1.2. Introduction to Techniques for Identifying Vulnerable Plaques

1.2.1. Introduction

There have been huge efforts to develop clinically useful imaging techniques for identifying "VP" and other lesions over the last 15 years. In this section, the most accepted proposed methods in developing diagnostic approaches for imaging vulnerable plaques are reviewed. The broad technological and clinical research on both the invasive techniques (such as intravascular angioscopy, intravascular thermography, optical coherence tomography, Raman spectroscopy, near infrared spectroscopy) and the non-invasive techniques (ultrafast computed tomography, nuclear imaging including positron emission tomography, ultrasound-based imaging techniques including elastography),will also be reviewed. The techniques which will be discussed in more details in the following sections, are as listed :

Non-invasive techniques:

- X-ray angiography
- Ultrafast Computed Tomography (UCT)
- Nuclear scintigraphy
- Magnetic Resonance Imaging (MRI)

Invasive techniques:

- Intravascular angioscopy
- Intravascular thermography
- Spectroscopy
- IVUS
- IVUS-Palpography
- IVUS-VH
- OCT

1.2.2. Non-Invasive Techniques

X-Ray Angiography

The basic principle of X-ray angiography is the same as a conventional X-ray: As X-rays pass through the body to impress an image intensifier; they are attenuated at different levels. These differences in X-ray attenuation constitute the resulting image, which can be useful while being used in addition to angiography.

Figure 1.5.: Biplanar X-Ray Angiography (Siemens HICOR).

Ultrafast Computed Tomography

In computed tomography (CT), different views of the same organ are acquired by moving the X-ray beam in a circularly movement around the body.
Ultrafast CT (UCT) (also known as electron beam computed tomography or EBCT, helical CT, or spiral CT) is a CT method which is able to quantify the amount of calcium in the coronary arteries, and thus has been primarily investigated as a tool of predicting the risk of coronary artery disease.

Nuclear Scintigraphy

In nuclear scintigraphy radioactive tracers are injected to the body organs and the emitted radiation from these tracers is used to acquire an image. Radioactive labeled molecules will be bound to the atherosclerotic rupture-prone lesion which in turn will provide useful information about the severity of the plaques.
The ability of nuclear scintigraphy is limited for the present. The radiotracers which may be specific for lipid core, macrophage density or thrombus and able to predict clinically significant events do not exist as yet.

High-Resolution Magnetic Resonance Imaging (MRI)

MRI can identify plaque components on the basis of biophysical and biochemical parameters, such as chemical composition and concentration, water content, physical state, molecular motion, or diffusion. And hence, it has emerged as the potential, leading, non-invasive, *in vivo* imaging modality for atherosclerotic plaque characterization.
MRI is based on a small magnetic field (a magnetic moment) of hydrogen nucleus. These magnetic moments align in a larger magnetic field. This allows them to display the phenomenon of nuclear magnetic resonance (NMR). MRI is a imaging technique for displaying NMR.

1.2.3. Intravascular (Invasive) Techniques

Angiography

Angiography has so far been the gold standard for identifying coronary and carotid artery lesions. It provides the practitioners with information about the severity of luminal narrowing and hence, enables the diagnosis of atherosclerotic disease. Angiography may show severe lesions, plaque disruption, luminal thrombosis, and calcification. It also serves as a decision making tool to direct therapy such as percutaneous coronary interventions or coronary artery bypass surgery. Although we can assess the lumen boundaries using angiography, no information is given on plaque burden, its delineation and components. Besides, it does not provide useful information about the vessel wall or atherosclerotic plaque composition such as the vulnerable lipid-rich plaques or other histopathological features [87]. But it is able to detect complex lesions. The problem is that angiography is a crude technique in which the presence and burden of vulnerable lesions and it is unable to detect the majority of ulcerated plaques as they are not big enough. Also, while diffuse atherosclerotic disease may narrow the entire lumen of the artery, angiography may underestimate the degree of local stenosis. About 70% of acute coronary occlusions are in the areas where the angiography results seem to be normal [1]. One important parameter in angiography is the time interval between the angiogram and the MI (myocardial infarction) as both time and interim therapy can influence atherosclerosis. Although, angiography has a low discriminatory power to identify the vulnerable plaque, if a disrupted ulcerated plaque is seen on angiography, additional rupture prone plaques may be expected. See figure 1.6 for an angiography image with a dissected flap within the lumen. An angiography device is depicted in figure 1.7.

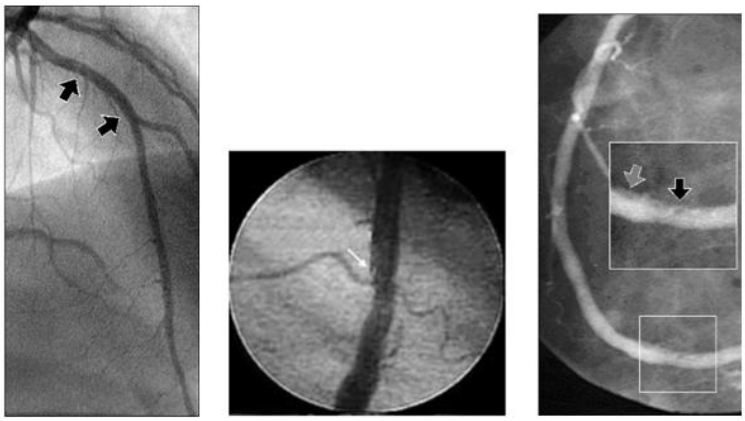

Figure 1.6.: An angiography image indicating a rupture plaque [1].

Intravascular Angioscopy

Intracoronary angioscopy, as the first intravascular imaging device, is based on a fiberoptic transmission of visible light. It facilitates direct visualization of the plaque surface, color of the luminal surface, presence of thrombus, and macroscopic features of the arterial wall. Angioscopy is able to detect vulnerable plaque features, such as ruptured caps

Figure 1.7.: Siemens Artis Zeego angiography device

and red discoloration (intra-plaque hemorrhage). Using this technique, the old thrombus or the normal appearance of the vessel surface is reflected as white. A red surface may indicates a fibrin or erythrocyte-rich thrombus and lipid-rich core and the thin fibrous cap is yellow in color. These yellow plaques are not detectable by angiography.
However, this technique has several drawbacks, one being the limited part of the vessel tree, angisocopy is able to investigate and that is due to the size of its device. One of the limitations of angioscopy is that the inability to examine the different layers within the arterial wall remains. Also, to make the visualization clear, the vessel has to be occluded and the remaining blood flushed away with saline. See figure 1.8 for angioscopy results.

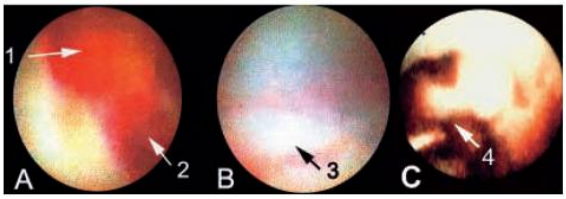

Figure 1.8.: Angioscopy results: A) A red thrombus on plaque 1 and blocking of a part of lumen 2, B) After removal of thrombus, C) Post angioplasty angioscopy [1].

Thermography

Thermography is a catheter-based technique which detects heat released by the cells of atherosclerotic plaques. Atherosclerosis is an inflammatory disease and any temperature difference in activated inflammatory cells may reflect and predict plaque disruption and thrombosis. The idea behind Thermography is the fact that vulnerable plaque is a very active metabolic area and higher temperature could be found, due to the heat released by activated macrophages either on the plaque surface or under a thin cap. While in many researches most atherosclerotic plaques showed higher temperatures compared to healthy vessel wall, the independent role of thermography is limited because the structural definition obtained from high resolution imaging techniques is required. The necessity of

a proximal balloon to provide a blood-free field is one of the limitations of this new technique. Also, plaque temperature may be affected by inflammation and variable blood flow in the lumen making the results unreliable. Another limitation to this technique is being unable to provide information on eroded but non-inflamed lesions.

Raman Spectroscopy

Spectroscopy is an optical technique which uses the reflected light from the plaques to determine the chemical composition of the tissue. Different chemical compositions scatter different wavelengths (and energies) so each tissue, due to its chemical composition (lipid, collagen, calcium, etc.), has a unique pattern of light absorbance. To apply this property and detect the chemical composition, many approaches are under development.
Raman spectroscopy collects light scattered by tissue when illuminated with high-energy laser. While most of this scattered light is at the same wavelength as the incident light, some are at different wavelengths. The amount of the wavelength shift which is called Raman shift depends on the characteristics of the molecule. Using this wavelength difference, Raman spectroscopy has a high molecular sensitivity but its tissue penetration is as low as 0.3 mm.

Optical Coherence Tomography (OCT)

Optical coherence tomography (OCT) is a useful technique which can provide images with ultra-high resolution. It measures the intensity of reflected light and compares it with a reference. The reference is obtained by a mirror reflection on an arm. The mirror is dynamically translated in order to achieve cross correlation at incremental penetration depths in the tissue. The measured intensity represents backscattering at a corresponding depth [1]. In figure 1.9 an OCT device is shown.

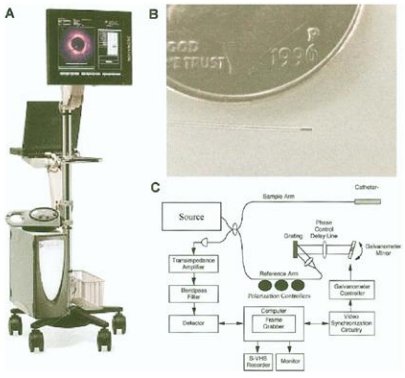

Figure 1.9.: A) OCT device (Lightlab (Westford, Massachusetts) imaging engine), B) OCT catheter and C) Schematic of OCT system [70].

OCT results in high resolution images for future diagnosis. The axial resolution of OCT is dependent on the bandwidth of the source or the range of wavelengths within the beam.

Based on histology, the OCT image interpretation is as follows: A lipid pool generates decreased signal areas with poorly delineated borders, a fibro-calcific plaque which shows a sharply delineated region with a signal-poor interior and a fibrous which plaque produces a homogenous signal rich lesion. It also provides useful information about structural details like thin caps or tissue proliferation [6].

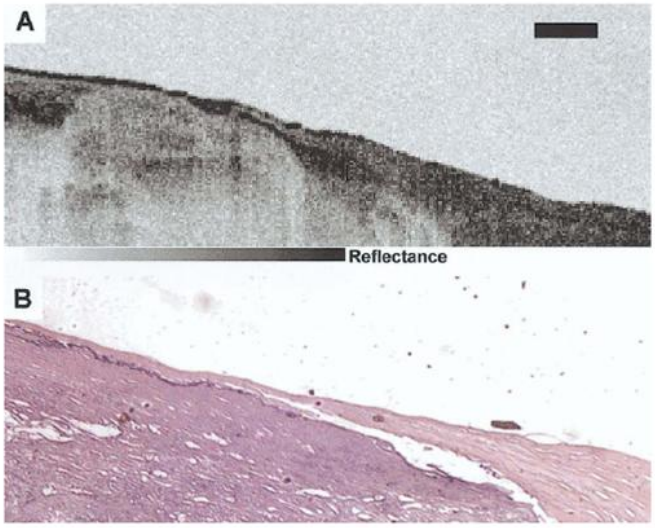

Figure 1.10.: (A) The OCT image. (B) The histopathology normal, native, in vitro human artery [6].

OCT Applications: Post-mortem studies demonstrated the accuracy of OCT in comparison with histology. The intravascular application of OCT has proven feasible in the animal model. These studies showed that OCT can detect both normal and pathologic artery structures. Recent experimental data suggest the possibility of detection of macrophages in atherosclerotic plaques. Detection of macrophage accumulation with OCT is based on the hypothesis that plaques containing macrophages have a high heterogeneity of optical refraction indices that exhibit strong optical scattering. Optical scattering results in a relatively high variance of the OCT signal intensity that can be expressed as normalized standard deviation (NSD) of the OCT signal. The analysis of NSD of OCT raw data reveals a high, positive correlation between OCT and fibrous cap macrophage density ($r=0.84$, $P<0.0001$) in vitro.
Most coronary structures that were detected by IVUS could also been visualized with OCT. Intimal hyperplasia and echolucent regions, which may correspond to lipid pools, were identified more frequently by OCT than by IVUS [68]. There are several potential applications of OCT. With its high resolution and unique characteristics, it is a powerful modality for detection of vulnerable coronary plaque. The most frequent variant of a vulnerable plaque is characterized by a lipid pool, a thin fibrous cap, and increased macrophage infiltration each of which can be detected by OCT. Another potential application of OCT is as an adjunct to PCI. Detailed structural information before and after coronary intervention can be evaluated with greater accuracy compared with intravascular ultrasound.

Over the past decade, the number of interventional devices and techniques has increased significantly. Precise plaque characterization optimizes the choice and evaluation of this percutaneous therapies.

TCFA Detection with OCT: OCT is now being introduced for *in vivo* human imaging at a resolution higher than any current imaging technology which allows for the identification of TCFA. OCT was shown to identify structural features such as lipid collections, thin intimal caps, and fissures characteristic of plaque vulnerability. OCT has also been directly compared with high-frequency intravascular ultrasound, the current clinical technology with the highest resolution. The superior resolution of OCT has been confirmed both quantitatively and qualitatively.
OCT has several limitations, first of all the low penetration depth may hinder studying large vessels and also the light absorbance by blood which currently needs to be overcome by saline infusion or balloon occlusion.

Introduction to Intravascular Ultrasound (IVUS)

Over the past few years, intravascular ultrasound (IVUS) technology has become very useful for studying atherosclerotic disease. IVUS is a catheter-based imaging technique providing real-time high-resolution images of the vessel wall and lumen.

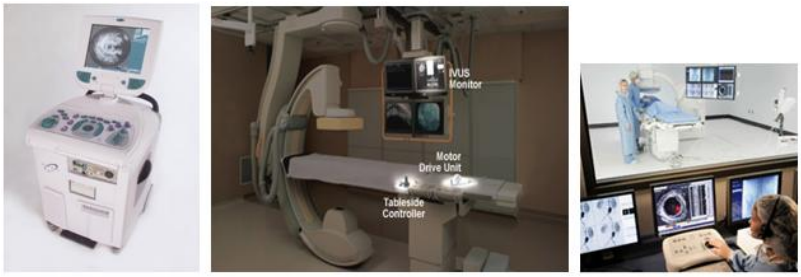

Figure 1.11.: IVUS device, from left to right: $Galaxy^TM$ IVUS imaging system, iLab® Ultrasound imaging system and Volcano IVUS Imaging $s5i^{TM}$ System

IVUS is useful in the evaluation of coronary disease due its characteristics. Sound waves bounce back with varying intensity and different time delays according to the density of the plaques they have encountered, and hence, grant the identification of plaque composition - fibrous, fibro - fatty, calcified or mixed (see figure 1.12). The time delay of reflected ultrasound waves is translated into spatial image information while, the intensity is converted to an intensity map encoded by a gray-scale. The displayed intensity for each target object is proportional to the amount of sound energy returned. Dense targets such as calcified plaques are bright white in the IVUS image and the least dense plaques such as the medical layer in the vessel appear black.
The 2D image is then obtained from the variation of the angular position of the imaged line over 360 degrees. Its features are detected based on the echogenecity and the thickness of the vessel. Depending on the distance from the catheter the axial resolution is approximately 150 microns and the lateral is 300 microns.

IVUS allows for precise measurement of the plaque burden by visualizing plaque topography. IVUS also shows the shape of the lumen as well as the thickness of layers of the wall.

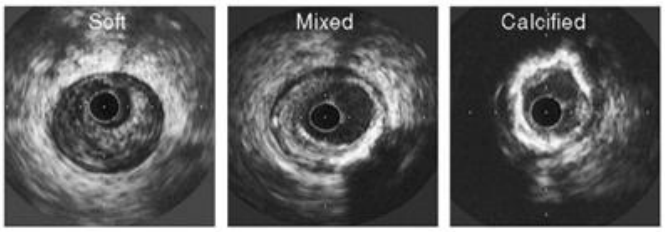

Figure 1.12.: Soft, mixed fibrous and calcified and calcified plaques identified using IVUS images [61].

Clinical Applications of IVUS IVUS should be considered supplemental to angiography, not as an alternative and should be used as an adjunct to angiography. The clinical use of IVUS for physicians is when angiography results are opaque and equivocal. IVUS allows measurements of cross-sectional area (CSA) and minimum lumen diameter (MLD), which can only be approximated with angiography. The most likely applications of IVUS is listed in table 1.2 and discussed in details in the following [61], [14].

Table 1.2.: Clinical applications of IVUS:

Clinical Applications of IVUS
Angiographically normal coronary vessels
Angiographically indeterminate lesions
Unstable plaque and thorombi
Left main coronary disease
Transplant coronary disease
Stenting of smaller vessels

Angiographically Normal Coronary Vessels: IVUS is able to detect occult disease in the patients with angiographically normal coronary arteries. 10% to 15% of patients undergoing catheterization for suspected coronary disease are shown as normal in angiography. Angiography usually underestimate disease burden as it has been shown that coronary disease is usually diffuse, not focal.

Angiographically Indeterminate Lesions: Angiographers mostly encounter lesions that elude accurate characterization using multiple radiographic projections. In some lesions (for example ostial and bifurcation) the stenosis may be opaque due to the overlapping of contrast-filled structures. By using IVUS in ambiguous lesions and because of its tomographic perspective, lesion quantification is possible without radiographic projection.

Unstable Plaque and Thrombi: An important application of IVUS may be the identification of atheromas at risk of rupture. As mentioned in previous sections, acute coronary syndromes frequently develop in minimally diseased vessels rather than high-grade stenoses. The appearance of thrombi in IVUS images has been studied in some researches and further studies are still required.

Left Main Coronary Disease: Assessment of the left main coronary disease by angiography leads to a difficult clinical problem. Aortic cusp opacification or "streaming" of contrast which may obscure the ostium, the short length of the vessel which may leave no normal segment for comparison and the distal left main artery which may be concealed by bifurcation or trifurcation are the main factors of the inability of angiography in the left main coronary disease diagnosis. These problems could be overcome using IVUS.
This can be reached by placing the ultrasound transducer distal to the left main vessel, while a slow pullback to the aorta is performed with the guiding catheter disengaged.

Transplant Coronary Artery Disease: IVUS is an optimal method for detecting coronary disease a year after transplantation. Based on medical studies, while angiography detects coronary disease in 10% to 20% of patients one year after transplantation, IVUS detects abnormal intimal thickening in about 50% of patients demonstrating the ability of IVUS in detecting this disease.

Stenting of Smaller Vessels: While angiography may underestimate vessel size in smaller vessels, IVUS allows direct and accurate vessel measurements at the lesion site. It is important because post-stent restenosis rates are higher in these vessels and small increases in stent area can decrease the rate of restenosis. IVUS usage in smaller vessels comes from its characteristics. For example, IVUS allows a more aggressive stent strategy, and hence, CSA is increased and restenosis rates are decreased. It also shows the edge tears from other vessel injuries which needs further intervention.
It has been observed that the occurrence of restenosis has an inverse relationship to the post-procedure in-stent lumen CSA.

IVUS Image Interpretation: In figure 1.13 a typical IVUS image is shown. In the image, the more dense elements are shown as brighter white while the less dense elements are shown as darker. It is important to notice that most plaques are eccentric which means there is more plaque on one side of the vessel than the other. At the center of the IVUS image, the catheter can be seen as a white bright circle.

Lumen appearance: Assessment of luminal dimensions is of great importance due to its effects on therapeutic decisions and so it represents one of the most important applications of IVUS. The lumen area can be determined by planimetry of the leading edge of the blood-intima acoustic interface. In vessels without atherosclerosis, IVUS measurements of lumen have a close correlation with angiography measures. But in diseased arteries, the correlation is moderate.

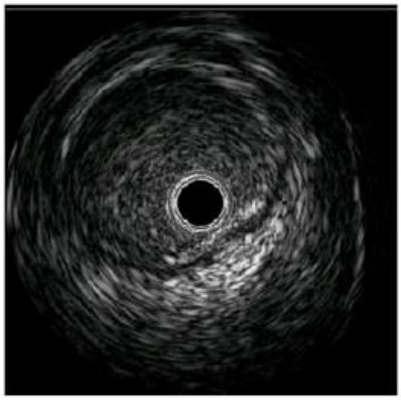

Figure 1.13.: Typical IVUS image.

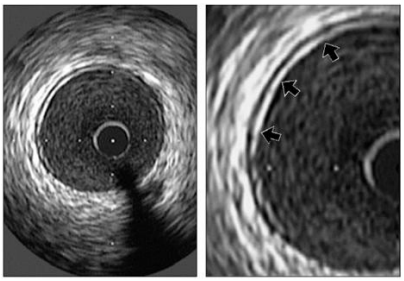

Figure 1.14.: Normal anatomy by IVUS. In magnified image (right), thin intimal leading edge is highlighted by arrows [61].

In such cases, the shape of lumen is extremely complex and angiography is unable to show it. This is probably due to an irregular, noncircular cross-sectional profile.

Normal Arterial Appearance: The appearance of normal coronary arteries has been categorized in many studies based on the characteristics of ultrasound reflections. Two tissue interfaces are observable, one at the border between blood and the leading edge of the intima and a second at the external elastic membrane (EEM), which is located at the media-adventitia border. See figure 1.15.

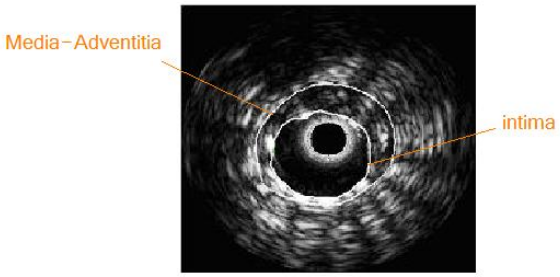

Figure 1.15.: Intima and media-adventitia borders

In high-quality images, the tunica media can be visualized as a distinct layer but the trailing edge of intima is not easily definable. Also the outer border of adventitia is not distinct and merges into the surrounding tissues. In normal arteries, the intima is thin, consisting mostly of endothelial cells and connective tissue, with a relatively small difference in the impedance from blood. In about half of the normal coronary images, the intima cannot be visualized as a distinct layer.

Characterization of Atherosclerosis: As mentioned above, IVUS is a useful method for studying the morphology of atherosclerosis *in vivo*. Below the plaque components and its appearance in IVUS images are described.

Plaque Components: All plaques with lower density than calcified plaques are called "soft plaque". However, the more specific terms "fibrous" and "fibro-fatty" are better terms than "soft plaque". Lipid-laden lesions appear hypoechoic, fibromuscular lesions generate low-intensity or "soft" echoes, and fibrous or calcified tissues are relatively echogenic.

Lipid-laden or fibromuscular lesions may exhibit a prominent echogenic fibrous cap, although most fibrous caps are too thin to be resolved by IVUS. Most of the plaques are a mixture of different types: fibrous, fibro-fatty and calcified as mentioned before.

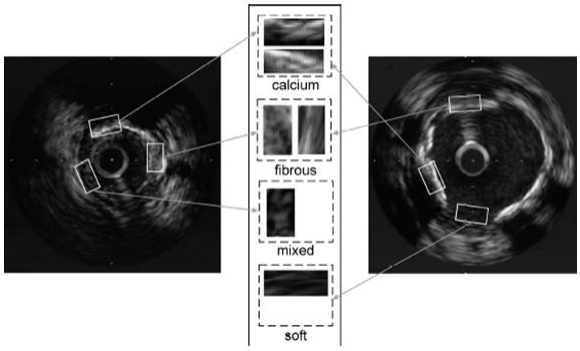

Figure 1.16.: Typical IVUS images presenting different kind of tissues [89].

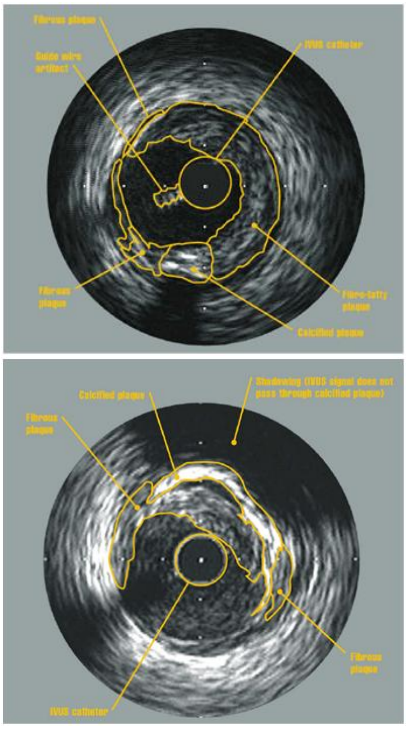

Figure 1.17.: Mixed plaque [14].

Two kinds of false imaging are associated with dense plaque formations (calcified plaques): reverberations and shadowing. Reverberations are the result of multiple copies of dense plaques. Shadowing appears as a black wedge-shaped area radiating outward from the calcified tissue [53].

Introduction to Virtual Histology (VH-IVUS)

Despite its usefulness in diagnosis, gray-scale IVUS imaging is somehow limited in regard to this analysis of plaque composition. Studies have so far demonstrated the potential to identify calcified plaques using IVUS images[43]; however, the identification of lipid pools

is hampered by relatively low sensitivity and specificity. Besides, calcified and dense fibrotic tissues are not easily differentiable in IVUS images due to the echoreflections. Virtual Histology is another sophisticated attempt for detailed tissue characterization and thus the recognition of lipid-rich, atheromatous cores in potentially vulnerable plaques [43]. VH-IVUS can distinguish between areas with low echoreflections, which can be beneficial in addition to IVUS imaging.

VH technique is based on backscatter analysis and mathematical modeling of the radiofrequency signals produced by the intravascular ultrasound unit. It provides a color-coded tissue map of plaque composition superimposed on cross-sectional images of the coronary artery obtained by IVUS. In figure 1.18 an IVUS image and the related VH-IVUS colored image is shown.

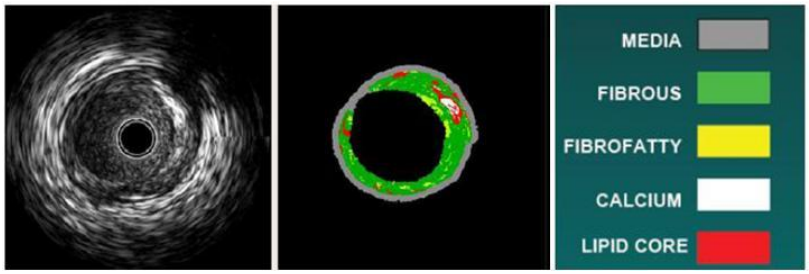

Figure 1.18.: IVUS image,VH-IVUS result and color map [100].

VH has demonstrated the potential to provide detailed quantitative information on plaque composition and morphology. It has been so far validated in studies of explanted human coronary segments[58]. In figure 1.19 Volcano VH^{TM} device is displayed.

Plaque Components: As discussed in the beginning of this chapter, many different cell and tissue types are commonly found in atherosclerotic plaques. But based on the resolution of VH-IVUS images, and to simplify images, plaque components are grouped into four basic tissue types during VH-IVUS imaging (see figure 1.18.c). These tissue types are displayed in table 1.3 [43].

VH Applications: Adaptive intimal thickening, pathologic intimal thickening, fibro-atheroma, TCFA and fibrocalcific plaques as discussed previously can be diagnosed using VH-IVUS images. VH-IVUS defines fibroatheromata as having a confluent necrotic core of more than 10% of the total plaque volume in mainly fibrous and/or fibrofatty tissue. TCFAs identified by VH-IVUS can be further sub-classified on the basis of certain characteristics such as necrotic core percentage of the tissue that increase the risk of sudden cardiac death, as determined by analyses of post-mortem data[43]. Different VH applications are presented in table 1.4.

Figure 1.19.: The Volcano s5 imaging system(VH^{TM} IVUS) [100].

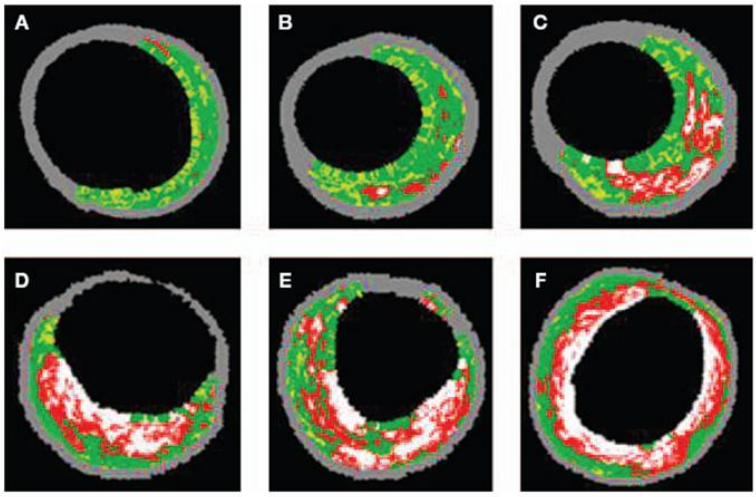

Figure 1.20.: Current coronary plaque classification in VH-IVUS images. (A and B) intimal thickening and (C, D, E and F) more vulnerable lesions, such as fibroatheroma. (D) In a thin-cap fibroatheroma, the necrotic core is proximal to the surface of the plaque (E) Thin-cap fibroatheroma presenting with several layers of necrotic cores suggests previous ruptures.

Table 1.3.: VH-based Plaque Components

Tissue type	Definition
Fibrous tissue	Fibrous tissue is represented as dark green pixels in VH images. This tissue type is characterized by bundles of collagen fibers with little to no lipid accumulation in or around the fibrous area. As we discussed in IVUS section, this type is displayed as bright white in IVUS images.
Fibrofatty tissue	Fibrofatty tissue is displayed in VH-IVUS by yellow or light green pixels. This tissue is characterized by loosely packed collagen fibers (fibrous tissue) and proteoglycan, and can be cellular, with or without interspersed foam cells.
Necrotic core (lipid core)	The necrotic core is represented by red pixels in VH-IVUS which refers to a tissue being characterized by a high concentration of extra cellular lipid within a necrotic core that is made up of remnants of dead, lipid-filled smooth muscle cells, foam cells, trapped red blood cells and fibrin.
Dense calcium	The dense calcium is represented by white pixels in VH-IVUS. This tissue is characterized by compact calcium crystals, as seen on histological specimens

Table 1.4.: VH Applications

Application	Description
Intimal thickening	Intimal thickening can be diagnosed by predominantly of fibrous tissue, which is identified as a green pixel or group of pixels in VH images.
Pathologic intimal thickening	A large group of green pixels in VH images (fibrous tissue) can identify pathologic intimal thickening
Fibroatheroma	Fibroatheroma can be identified by necrotic tissue, which is displayed in VH images by red pixels. It can contain calcified tissue or not.
Thin-cap fibroatheroma	Thin-cap fibroatheroma is identifiable by NC>10% and no evidence of fibrotic tissue between lumen area and NC area.
Fibrocalcific plaque	Fibrocalcific plaque is identified by fibrous plaques with dense calcium (>5% of plaque volume) Single or multiple layers of calcium

1.3. Problem Statement

Lesion components respond differently to pharmaceutical and interventional therapies. Lesions containing a high proportion of collagen fibers (hard plaques) respond well to clinical interventions such as angioplasty, atherectomy, and stent deployment. Lipidic or soft plaques are relatively unstable, small in size, and prone to rupture. Soft plaques have been implicated in acute ischemic syndromes, such as plaque rupture, which can lead to thrombus formation and sudden cardiac death but they are more likely to regress with diet and drug therapy [90]. Focal calcifications often form the initiation site of dissection after balloon angioplasty and specific patterns of calcification strongly correlate with the risk of major post-angioplasty dissection [90]. Moreover, directional atherectomy is less effective in the presence of extensive superficial calcification and is often efficacious in non-calcified arteries and rotational atherectomy is reported to preferentially ablate calcified atherosclerotic plaque components [90]. Thereby, understanding plaque composition is a vital step in the evaluation of coronary arteries. Accurate characterization of plaque lesions helps the clinician to choose the appropriate clinical intervention and assess the effects of therapy. In addition, characterization of plaque could provide valuable information in longitudinal studies of atherosclerosis following drug therapy, in understanding the process of vascular remodeling, or in the assessment of heart transplant patients during clinical follow-up [90].

Due to the importance of plaque characterization, different techniques have been developed over the last twenty years and some methods are yet to come. Among the methods that had been discussed in previous section, VH and OCT seem to be more useful in diagnosis. Although these two novel methods are extremely valuable, their accuracy is still vague. Additional steps should be taken to provide physicians with a complete accurate

tool.
To be more specific, if some of the limitations of VH are eliminated, it could be one of the best techniques in the field. VH applications and accuracy has been examined thanks to many researchers which will be more discussed in Chapter 3. Also its limitations are specified.
One of the limitations of VH is the ECG-gated acquisition. In principle, the heart is relatively at rest in the end-diastolic point (peak R-wave), and, in most ECG-gating methods, this moment is chosen to acquire an image (see figure 1.21). Capturing only one frame per cardiac cycle significantly decreases the longitudinal resolution of IVUS imaging. In order to accurately calculate plaque compositions, the smallest longitudinal spacing between the acquired IVUS images is crucial [60] , [66].
An IVUS based characterization method supported by image processing techniques could further provide the crucial information which VH is not able to. Although image based characterization techniques can be found in literature, the synchronization between VH and IVUS image-based characterization would increase the applicability of VH. Also a method which is validated and trained based on VH images can extend the accuracy of such techniques.
Thus, an IVUS image based technique, which is proposed in this thesis, will enhance the use of VH technique among physicians.

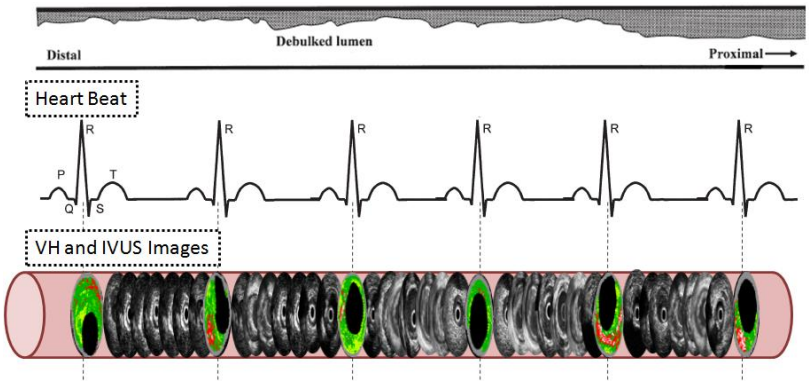

Figure 1.21.: ECG-gate acqusition in VH

2. Chapter Two: Technical Principles of IVUS

2.1. Introduction

As discussed in the previous chapter, IVUS has undergone many medical practice changes since its advent. So far, several clinical applications have been suggested for IVUS and their acceptability has been studied. Although for the physicians the clinical results are vital, from an engineering point of view the physics and idea behind IVUS is at the centre of attention .Hence, in this chapter the basic physics of ultrasound is discussed for further understanding of the IVUS technique.

2.2. Physics of Ultrasound

Ultrasound is high-frequency sound which is described by its wavelength or frequency. Sound waves which are audible for human are in the range of 20Hz to 20kHz, whereas ultrasound waves used in medicine are high frequency waves between 2 and 15MHz [86]. Originally, waves with a frequency more than 20 kHz are described as ultrasound.

Basically, in different mediums, the speed of sound wave is different. The speed of sound in a medium is calculated as follows:

$$c = \sqrt{\frac{1}{k.\rho}} = \lambda.f \tag{2.1}$$

c is the speed of the sound, k and ρ are compressibility and density of the tissue and λ and f are wavelength and frequency respectively.

But ultrasound systems usually use an estimation of 1540m/s for all mediums which is the average speed of ultrasound in the body. Although it may result in little errors in estimated distances in different mediums, this estimation has been advantageous in most systems.

2.2.1. Ultrasound Generation

To generate ultrasound waves, vibration should take place within a medium. For this purpose, a transducer which converts electrical energy into mechanical energy is used (figure 2.1). Piezoelectric materials are capable of providing such conversion. Piezoelectric materials vibrate at the same frequency as the frequency of the voltage applied to them. The resonant frequency of a transducer is the frequency at which the transducer works more efficiently and is related to the thickness of the piezoelectric material. Resonant frequency is the frequency that results in the most vibration of the material. It is reached when reflected waves of the front and back of the material reinforce each other.

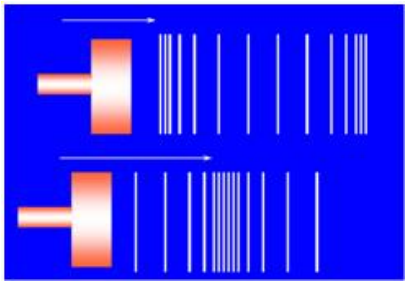

Figure 2.1.: Generating ultrasound waves [86].

An array of transducers is used in most systems which consists of small transducers in a row to provide more widespread waving (figure 2.2)

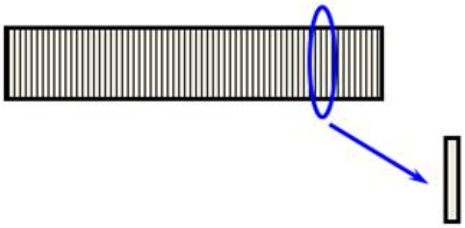

Figure 2.2.: An array of transducers [86].

2.2.2. Pulsed Ultrasound

Sending ultrasound waves continuously will make it impossible to predict the distance of different boundaries as the information about each boundary. This problem is solved using pulsed ultrasound. When pulses are produced, they travel within the medium and reflect. Typically short pulses are used to provide the chance of differentiating between close boundaries. A pulse is usually composed of different frequencies and amplitudes (figure 2.3).

2.2.3. Interaction of Ultrasound with Surfaces

Reflection

When an ultrasound wave meets a surface between two adjacent mediums, a part of the energy is reflected backward. The factor that is associated with the amount of reflected energy is called the acoustic impedance between the two materials:

$$Z = \rho c \tag{2.2}$$

Where ρ is the density of the material and c is the propagation speed of the sound. Acoustic impedance is the medium resistance against sound waves in the medium and depends on the density and compressibility of the medium. The key factor in reflection is the difference

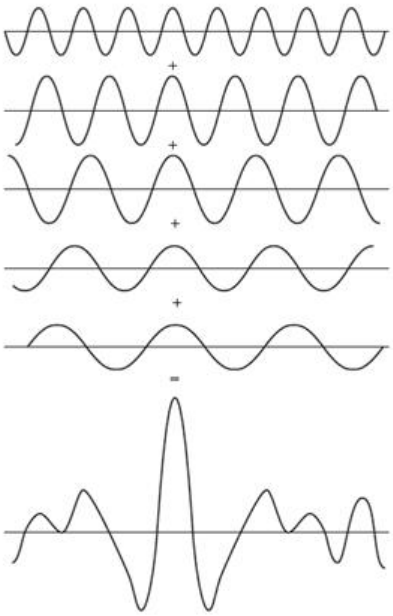

Figure 2.3.: A typical ultrasound pulse composed of signals with different frequencies [86].

between acoustic impedance of the two materials. In table 2.1 acoustic impedance of some materials are reported. The greater the difference in acoustic impedance, the greater is the proportion of reflected energy (figure 2.4). However, if there was no difference in acoustic impedance, there would be no reflection.

Another important factor in reflection is the angle of incidence (figure 2.5). Due to the incidence angle, the reflected and refracted waves are calculated using the following equations:

$$R_i = [(Z_2 Cos(\theta_i) - Z_1 Cos(\theta_t))/(Z_2 Cos(\theta_i) + Z_1 Cos(\theta_t))]^2 \tag{2.3}$$

$$T_i = (4 Z_1 Z_2 Cos(\theta_i) Cos(\theta_t))/(Z_2 Cos(\theta_i) + Z_1 Cos(\theta_t))^2 \tag{2.4}$$

Where θ_i is the incidence angle, θ_r is the reflected angle and θ_t is the refracted angle.

Attenuation

Attenuation is the energy loss of sound waves as they travel through the material. The deeper the wave travels in the body, the weaker it becomes. The loss of energy will further impress the energy of the reflected waves. Attenuation is the result of three factors: reflection, absorption and scattering. Absorption is the process in which, ultrasound energy is converted into heat. Scattering from small or rough structures may prevent the waves from returning to the transducer and hence get lost. These factors together may result in lower energy of the reflected beams.

Table 2.1.: Acoustic impedance in different materials [57].

Material	$Impedance, Z(kgm^{-2}s^{-1})$
Air	0.0004×10^6
Blood	1.61×10^6
Brain	1.58×10^6
Fat	1.38×10^6
Human soft tissue	1.63×10^6
Kidney	1.62×10^6
Liver	1.65×10^6
Muscle	1.70×10^6
Skull Bone	7.80×10^6
Water	1.48×10^6

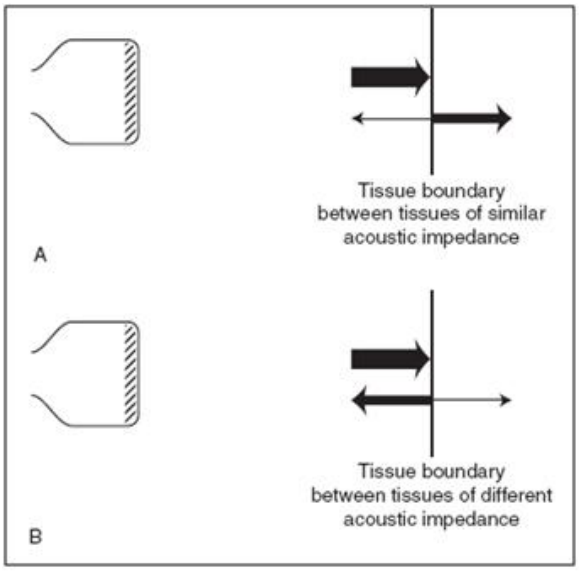

Figure 2.4.: Role of acoustic impedance in reflection [86].

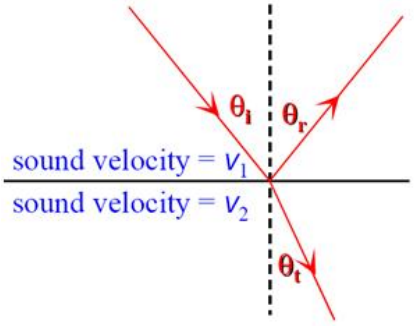

Figure 2.5.: Angle of reflection [86].

The intensity loss of the waves while travelling through the material is proportional to the intensity itself and distance they travel:

$$\Delta I = -\mu I \Delta x \tag{2.5}$$

Where μ is the attenuation constant depends on the material characteristics. μ itself depends on tissue viscosity (η) and density (ρ) and ultrasound frequency (ω) and speed (c):

$$\mu = \frac{2\eta\omega^2}{3\rho c^3} \tag{2.6}$$

According to equation 5, the attenuation depends on μ (figure 2.6).

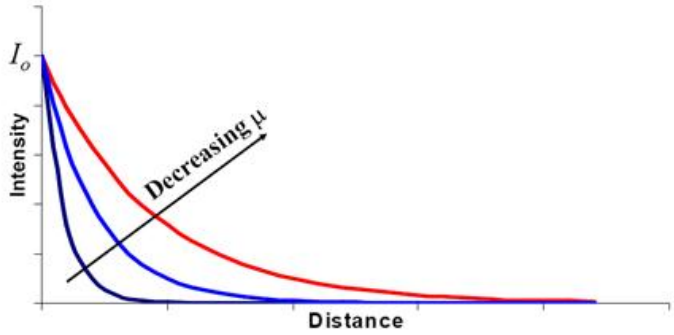

Figure 2.6.: Attenuation in different materials [86].

2.2.4. Forming Image

Those reflected and scattered waves returned to transducer are used for ultrasound imaging. Doubtlessly, the goal of any ultrasound system is to make the similar tissues look alike and different ones look different.

When reflected waves (hereafter backscatter signal) reach the transducer, they make it vibrate. This vibration is further converted into electrical energy by piezoelectric element. The amplitude of the reflected waves is a key element of distinction between different materials. Simultaneously, boundary depth is detectable based on the time delay of reflected waves.

There are different modes for providing images from backscatter signal. In A-mode which is used for eye images, a short pulse is send out and the echoes and their time delay are measured (figure 2.7)

If different amplitudes are displayed as spots with varying brightness, the display type is called B-mode. By moving the transducer slightly so that the path of new waves are adjacent to the previous ones, a B-mode image can be produced (figure 2.8). As mentioned before most systems now use an array of transducers which may provide B-mode images without any need for transducer movement.

Another display mode, M-mode, is a composition of A-mode and B-mode. In M-mode scan, different A-mode scans are obtained in different times where transducer is stationary.

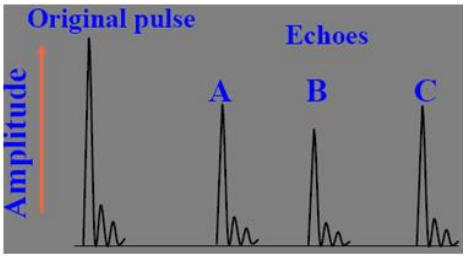

Figure 2.7.: A-mode representation of backscatter ultrasound [86].

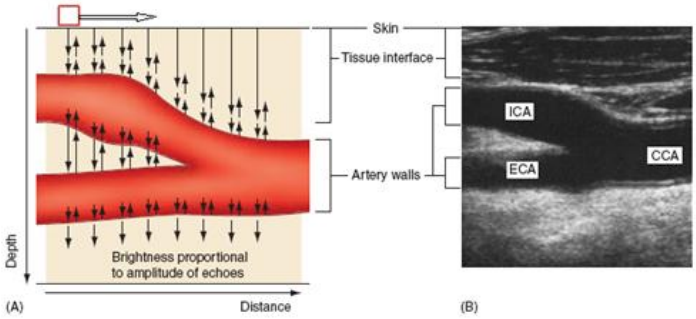

Figure 2.8.: B-mode imaging method: (A) and displayed in brightness mode in adjacent scan lines, (B) a B-mode image is produced [86].

2.2.5. Image Resolution

The resolution of a system is identified by its ability to distinguish between two adjacent objects. With regard to ultrasound images, three different planes of resolution are considered: axial (along the beam), lateral (across the image) and slice thickness (figure 2.9).

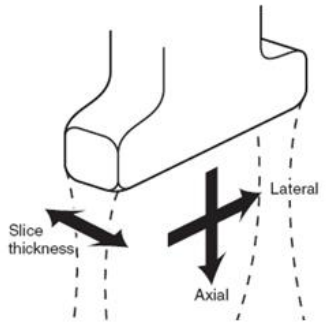

Figure 2.9.: Different planes of resolution [86].

The axial resolution is the capacity of the ultrasound technique to separate the spatial position of two consecutive scatterers through its corresponding echoes. As can be seen in figure 2.10.a an ultrasound pulse $P1$ with width $d1$, frontally affects a linear scatterer array. Echoes from these scatterers form a "train" of pulses temporally distanced $t_{oi} = 2\frac{|R_i|}{c}$, being R_i the i^{th} relative emitter-scatterer distance and c the pulse propagation speed. As the distance between linear scatterers reduces, the time between the maxima of the train's pulses reduces until a critical distance is reached[15]. A critical distance from which the pulses arrive at the receiver are superposed and therefore, the system would not be able to discriminate or separate the echoes produced by each scatterer. This critical distance is related to the pulse width d_t and called axial resolution. In figure 2.10.b it is seen that the resolution can be improved by diminishing d_t, which is equivalent to increasing the frequency of the emitted pulse. In fact, the axial resolution of this technique depends on two factors: the ultrasound speed c and pulse duration d_t. The functional dependency between the spatial resolution, the frequency and the ultrasound speed propagation is given by (7):

$$d_r = cd_t = cT = \frac{c}{f} \tag{2.7}$$

Where d_r is the axial resolution, c is the ultrasound speed for biological tissues, d_t is the pulse width, T is the period of ultrasound wave and f is the ultrasound frequency. Different axial and lateral resolutions for different frequencies are displayed in table 2.2. The angular resolution is the capacity to discern two objects or two events located in the tangential direction that depends on the Beam width. The beam width depends on the transducer effective emission area (figure 2.11).

Slice thickness will affect the region perpendicular to the scan plane over which returned echoes are obtained. The slice thickness should be as thin as possible to maintain the image quality as much as possible. Thereby, focusing is often used in this plane as well as in the imaging plane.

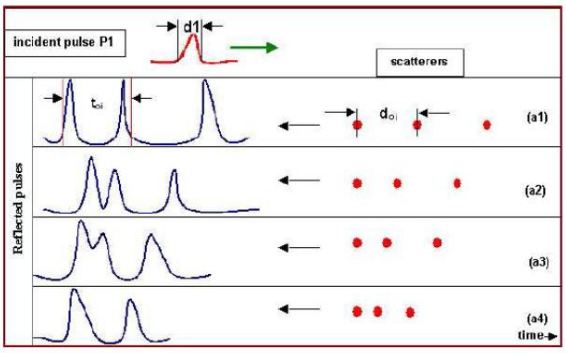

(a)

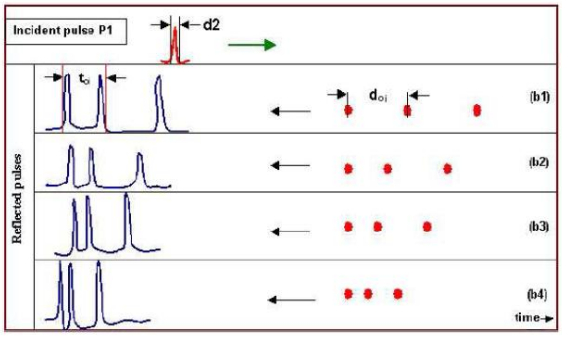

(b)

Figure 2.10.: We can see that the progressive distance reduction of the linear scatterers from $a_1 - a_4$ in (a) or $b_1 - b_4$ in (b) reduces the time difference between the maxima of the "train" pulses. The maxima can be separated by reducing the pulse width from d_1 in (a) to d_2 in (b), this is equivalent to an increase in the pulse frequency [74].

Table 2.2.: Axial and lateral resolution based on transducer frequency

MHz	Axial Resolution	Lateral Resolution
3.0	1.1 mm	2.8 mm
4.0	0.8 mm	1.5 mm
5.0	0.6 mm	1.2 mm
7.5	0.4 mm	1.0 mm
10.0	0.3 mm	1.0 mm

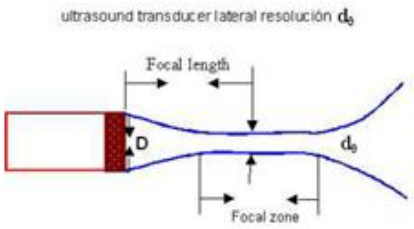

Figure 2.11.: The focal length and the focal zone of a ultrasound transducer are indicated. The transducer lateral resolution d_θ is a function of its diameter, D and the emission frequency, f [74].

2.3. Principles of IVUS

IVUS is a technique in which by using a catheter (figure 2.12) as a transducer, invaluable images of coronaries are provided (for its applications see Chapter 1).

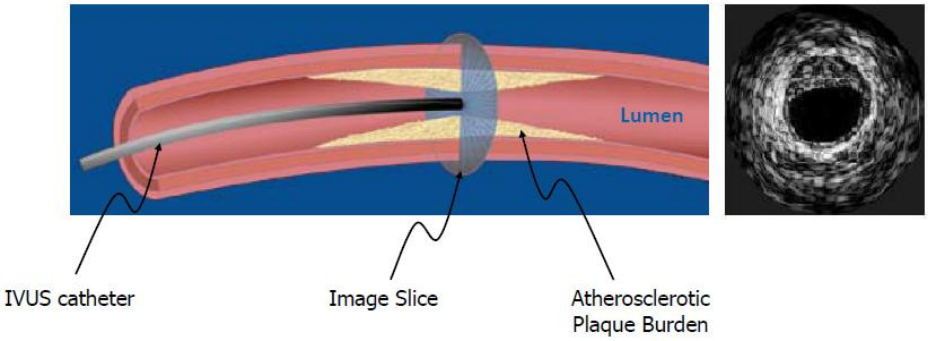

Figure 2.12.: Technology of IVUS Imaging [53]

2.3.1. Equipment for IVUS Examination

There are two different types of IVUS transducers: the mechanically rotating transducer and the electronically switched multi-element array system [53] (figure 2.13). The former is referred to as a ″mechanical IVUS system″ and the latter as a ″solid-state design IVUS system.″

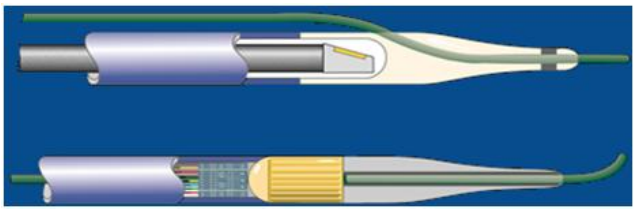

Figure 2.13.: Mechanical rotating probe (top) and phased array probe (bottom) [53].

Mechanical Systems

A single rotating transducer is driven by a flexible drive cable at 1,800*rpm* (30 revolutions per second) to sweep a beam almost perpendicular to the catheter. At approximately 1° increments, the transducer sends and receives ultrasound signals. The time delay and amplitude of these pulses provide 256 individual radial scans for each image. Because even small air bubbles can degrade image quality, mechanical transducer catheters require flushing with saline to provide a fluid pathway for the ultrasound beam. In most mechanical systems, the transducer spins within a protective sheath while the imaging transducer is moved proximally and distally. This facilitates smooth and uniform mechanical pullback.

Electronic Systems

Electronic systems use an annular array of small crystals rather than a single rotating transducer. The array can be programmed so that one set of elements transmits ultrasound pulses while a second set receives the echo pulses simultaneously. The coordinated beam generated by groups of elements is known as a synthetic aperture array. The image can be manipulated to focus optimally at a broad range of depths. The currently available electronic system provides simultaneous colorization of blood flow. A standard configuration of IVUS acquisition images consists of three components. Figure 2.14 shows a scheme of catheter with a piezoelectric transducer miniaturized the pull-back unit and the console to reconstruct the images. IVUS catheter has a rank of measures that oscillates between 2.9*F* to 3.5*F* (0.96 to 1.17*mm*) of diameter. The quality of the image depends on the operation frequency, which is in the order of 20 to 50*MHz*, so that the lateral resolution would be approximately of the order of 113μm and the axial resolution would be of the order of 80 μm [39]. The IVUS acquisition process is initiated when the catheter is manually (guided by the angiography) inserted within the artery (figure 2.14 (a)). The catheter pullback is made at linear constant velocity (usually 0.5*mm/s*) and its rotation has constant angular velocity of 1800*rev/min*. The pivoting transducer sends a radially focused beam of ultrasound and receives its corresponding echoes.

The obtained radial lines for different angular transducer positions are then processed, giving a 2D cross section artery image (figure 2.14 (b)). The sequence can be shown as a longitudinal sequence resulting in a longitudinal artery cut (figure 2.14(c)). The resolution of an ultrasound image is directly related to the ultrasound signal frequency and high frequencies allow for the obtaining of better resolution. Nevertheless, with the increase of frequency, the attenuation of ultrasound waves while penetrating the biological tissue is also increased. The typical frequencies of the IVUS technique are in the range of 20 MHz to 50*MHz* with inferior resolutions of 50μm.

2.3.2. Longitudinal Display (L-Mode)

An important limitation of IVUS is that only single cross sectional images of the coronary artery are displayed that limits the spatial orientation and precluding facile assessment of the length and distribution of plaque and lesions.

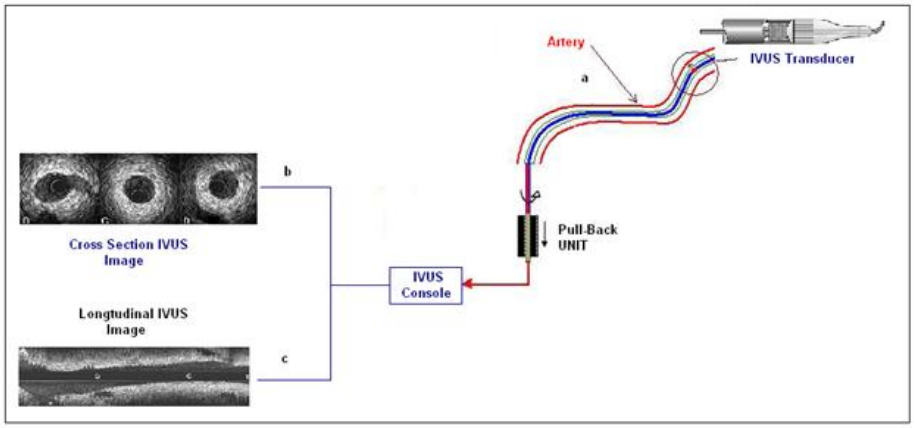

Figure 2.14.: Block diagram of IVUS Acquisition System [74].

Motorized transducer pullback and digital storage of cross-sectional images are necessary for longitudinal (L-mode) imaging. In an L-mode display, computerized image reconstruction techniques display sets of ”slices” taken from a single cut plane within each of a series of evenly spaced IVUS images to approximate the longitudinal appearance of the artery [29].

To be meaningful, the cut plane should be through the center of artery mass or of the lumen, not arbitrarily through the center of the catheter. Widely position variation of catheter within the vessel can arbitrarily affect the appearance of the artery. There are major limitations of L-mode display including the obligate straight reconstruction of the artery and the ability to display only a single arbitrary cut plane. Characteristic motion artifacts result in a ”saw-tooth” appearance because of relative movement of the transducer and vessel, although ECG-triggered image acquisition may eliminate some of these artifacts [8], [18]. Excessive artifacts may result in misinterpretations by inexperienced users. Therefore, the L-mode should not be used for quantitative purposes (figure 2.15).

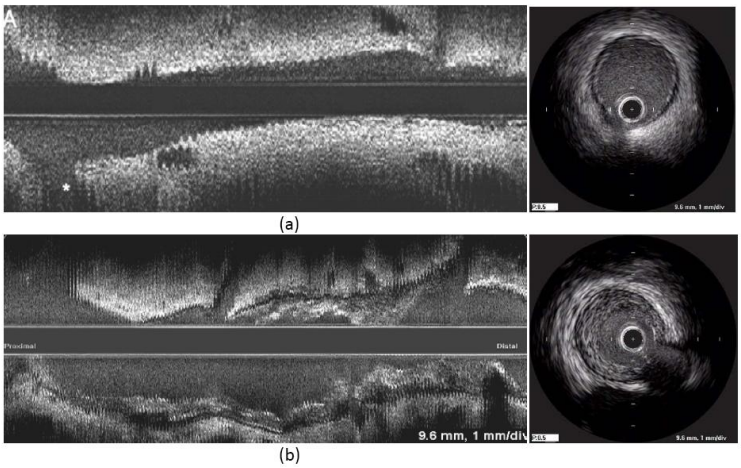

Figure 2.15.: (a) The longitudinal and cross sectional image for normal vessel (b) diseased vessel.

2.3.3. A Basic IVUS Image Model

Correct image processing requires understanding the image formation, gray-level meaning, artifact causes, the averaging and the motion of the dynamics structures. Thereby, generation of simulated IVUS images is important because of four reasons: a) generation, processing and visualization in the format that expert physicians use, b) the exploration of some of the artifacts generated by the averaging of the beams, c) the smoothing and treatment of the images to generate sufficient data to validate image processing algorithms, and, d) comparison of data generated by the image formation model to the real data [15]. IVUS images can be obtained in a simulated form using a simple physical model based on the transmission and reception of high frequency sound waves that radially penetrate a simulated arterial structure (figure 2.16). For this model, we assume that the waves are emitted by a transducer located in the center of the artery and that these waves propagate radially through the blood and the arterial structures (intima, media and adventitia) being reacted progressively by them. The reflected waves or echoes are received by the transducer that now behaves as a receiver. The time between the emission and the reception is directly related to the distance between the source and the reflector (figure 2.17).

The echo amplitude, which is a function of time, is transformed onto gray-scale and later to penetration depth and the radial coordinate is determined. If we place a rotator transducer that make a registry of the corresponding echoes for each angular position of the transducer and combine all the lines obtained from different positions we will obtain a simulated 2D image of the structure in study. The simulated 3D IVUS can be generated by concatenating the planes generated independently taking into account the arterial deformation caused by the blood pulsatile pressure.

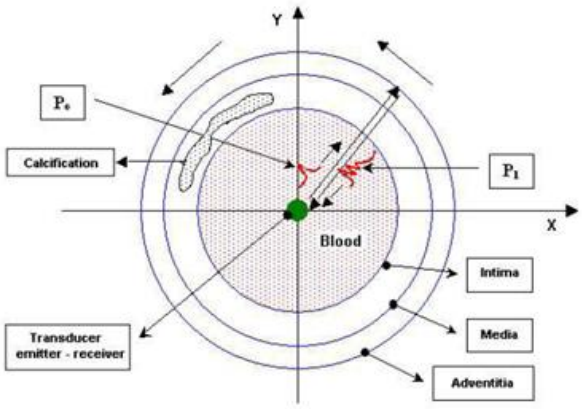

Figure 2.16.: The disposition of the simulated arterial structures (blood, intima, media and adventitia) and calcification are illustrated. The ultrasound rotator transducer which emits the pulse Po and receives pulse P1 has been placed at the coordinate center [74].

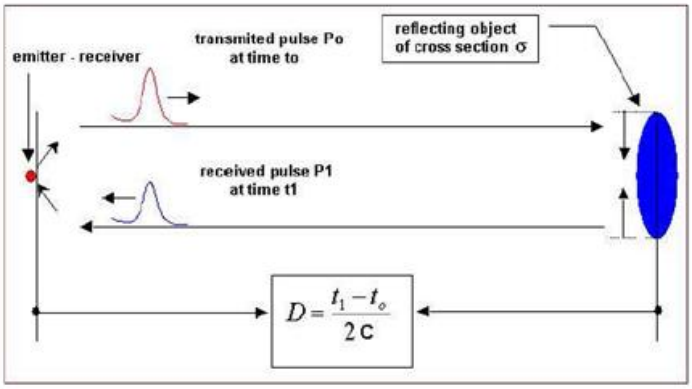

Figure 2.17.: The determination of the distance D between the emitter/receiver and the reflecting object is done from the difference of time between the transmitted pulse Po and the received pulse P1 assuming that the pulse speed c is constant [74].

2.3.4. IVUS Artifacts

Non-Uniform Rotational Distortion (NURD) and Motion Artifacts

Non-uniform rotational distortion is unique to mechanical catheter systems and results from mechanical binding of the drive cable that rotates the transducer [35]. This can occur for a number of reasons including the presence of acute bends in the artery, tortuous guide catheter shapes, variance in the hub or driveshaft manufacturing, excessive tightening of a haemostatic valve or kinking of the imaging sheath. In an extreme situation, fracture of the drive cable can occur (figure 2.18(c)). A distinct motion artifact can result from non stable catheter position. Occasionally, the vessel moves before a complete circumferential image can be created that result in the cycle deformation of the image. In addition, both mechanical and solid state transducers can move as much as *5mm* between diastole and systole. This can preclude accurate assessment of arterial phenomena that depends on the cardiac cycle (i.e., arterial pulsation and compliance).

Ring-Down, Blood Speckle, and Near Field Artifacts

Ring-down artifacts are usually observed as bright halos of variable thickness surrounding the catheter. They are produced by acoustic oscillations in the transducer, which result in high-amplitude ultrasound signals that obscure the area immediately adjacent to the catheter (figure 2.18(a)). Ring-down artifacts are present in all medical ultrasound devices and create a zone of uncertainty adjacent to the transducer surface. Although time gain compensation (TGC) can be used to decrease this artifact, excessive ring-down suppression can reduce signals from true targets. In the solid state systems, the transducers are surface mounted and ring-down is partially reduced by digital subtraction of a reference mask. In the case of incorrect performance, digital subtraction is potential to remove real information or introduce false targets. The intensity of the blood speckle increases (exponentially) as transducer frequency is increased and as blood flow velocity decreases. This phenomenon can limit the ability to differentiate lumen from tissue (especially soft plaque,

neointima, and thrombus). This problem is exacerbated by flow stagnation or rouleaux formation, often most evident when the catheter is across a tight stenosis or within certain dissections (e.g. intramural hematomas). As with ring down suppression, TGC manipulation to reduce blood speckle can reduce signals from real targets. Some operators flush contrast or saline through the guiding catheter to clear the lumen and to help identifying tissue borders. Computer-based imaging algorithms can also suppress or differentiate blood speckle from tissue.

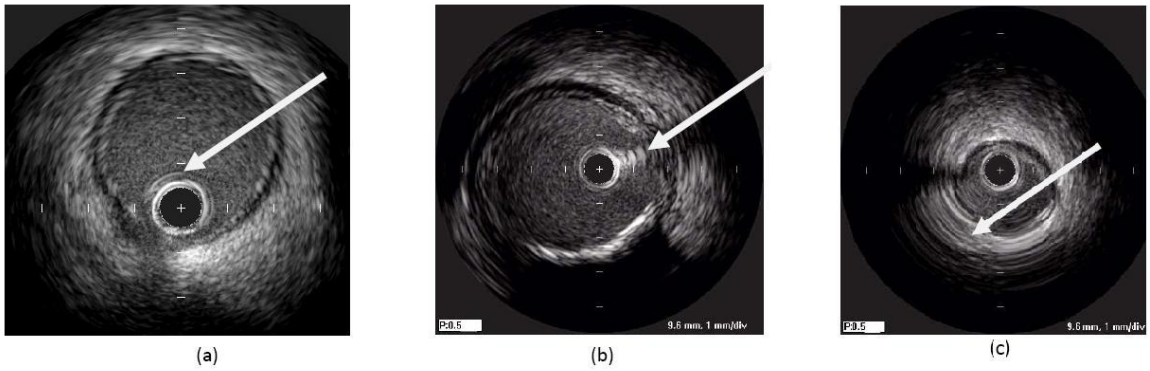

Figure 2.18.: (a) Ring Down Artifact in an IVUS image, (b) Guide wire artifact, (c) A sample of NURD in an IVUS image [14].

Obliquity, Eccentricity, and Problems of Vessel Curvature

Current imaging techniques assume that the vessel is circular, the catheter is located in the center of the artery, and the transducer is parallel to the long axis of the vessel. However, both transducer obliquity and vessel curvature can produce an image giving the false impression that the vessel is elliptical. Transducer obliquity is especially important in large vessels and can result in an overestimation of dimensions and a reduction in image quality [51]. Image quality reduces because the amplitude of the echo reflected from an interface depends on, in part, the angle at which the beam strikes the interface. When the catheter is coaxial within the vessel and/or the beam strikes the target at a 90° angle, the strongest signals are obtained. Therefore, lower image quality and errors in interpretation are more likely when the IVUS catheter is not parallel to the vessel wall. The guide wire artifact is the visualization of the wire shadow in the lumen area as shown in figure 2.18(b).

Problem of Spatial Orientation

There is no absolute anterior, posterior, left and right orientation possible in IVUS images. However, with some systems, images can be rotated electronically to produce a constant orientation. For example, images of a left anterior descending coronary can be electronically rotated so that the circumflex is positioned at 9 o'clock. With this orientation, the diagonal branches will arise from the left side of the image and the spatial branches will appear perpendicular to the diagonal branches. However, electronic rotation of the image is an electronic aid for interpretation and not a definitive standard. Side branches,

visualized with both angiography and ultrasound, are extremely useful as landmarks in facilitating interpretation and comparisons. Some authors also describe the use of perivascular landmarks as important references for both axial position and tomographic orientation within the vessel. These landmarks are including the pericardium, strands of muscle tissue, and the venous system.

3. Chapter Three: Plaque Area Detection

3.1. Previous Methods for IVUS Border Detection

3.1.1. Introduction

Intravascular Ultrasound (IVUS) imaging is a unique clinical imaging tool that provides cardiologists with a cross-sectional inside view of the vessel and, thus, allows a complete study of its morphology, such as arterial wall, lumen, or the plaque. The technique helps in diagnosis and treatment of cardiac diseases, as far as availability of a precise characterization and segmentation of arterial structures. A manual processing of images apart from being a tedious time-consuming task, might suffer from intra- and inter-observer variability. This fact motivates the development of image processing techniques addressing detection of the arterial structures. As stated in Chapter One, the accumulation of different plaques such as soft (lipid), fibrotic or calcified regions between the two layers of vessel wall (intima, the inner layer and media-adventitia, the outer layer) will lead to atherosclerotic lesions. The area of the plaque accumulation between these layers will determine whether the lesion is significant (borderline or intermediate) or not. So the first step in characterizing the plaque is to determine the borders of the vessel wall.

3.1.2. Previous IVUS Researches

Image segmentation is the process of separating or grouping an image into different parts. Because it is a difficult, subjective and time-consuming procedure to manually perform the segmentation, there is an increasing interest in the development of automatic border detection and tissue characterization methods for IVUS images. There is a wide range of segmentation approaches which have been studied over the years [4],[65],[10],[31],[33].

Withey and Koles in [97] classified the segmentation methods into three generations. First-generation methods like region growing [102], [77], [49] are low-level techniques while second-generation methods like active contours [36], [81] use optimization methods and uncertainty models. Both these generations are region-based segmentation methods. The active contour methods are suitable for finding the edges of a region gray-scale or some other features which are significantly different from the surrounding region [97]. Third-generation methods benefiting from higher-level knowledge such as a priori information and expert-defined rules. Shaped models constitute the third generation.

In the fist-generation, Paul et al. proposed a method for border detection using region-growing based on inter-pixel gray-scale differences. In this method, the center pixel of each image is used as the initial seed point to guarantee that the algorithm always starts in the lumen. Two automated border detection schemes, components-labeling (CL) with

dilation-erosion and watershed segmentation (WS) are used to correct the leaked regions due to signal drop-out and strut artifacts [5]. Watershed segmentation was chosen due to its ability to separate features to allow for counting, identification or measurements. Erosion and dilation were implemented to break the leaked region from the luminal region and components labeling was chosen to identify the luminal and leaked regions. The choice of threshold is important in both schemes, since a too small threshold will limit the growth of the luminal region and a too large threshold results in overgrowth into the arterial wall. An appropriate threshold that allows growth up to the luminal border, sometimes results in leaks extending beyond the luminal region. Paired *t-test* comparison of the areas showed that CL detected lumen areas were not significantly different from expert-traced contours but WS detected lumen areas were somehow differs from expert-traced contours.

The adventitia layer appears as a weak edge in IVUS images with a non-uniform gray-level that makes its detection difficult. However, although adventitia detection is crucial for reliable plaque quantification, the topic has hardly been approached.

A novel method for adventitia segmentation based on local orientation of image structures is proposed in [34]. There are two stages in adventitia detection: extraction of points laying on the adventitia and recovery of a closed model of such points.

Adventitia candidate points are selected by means of the negative edges of minimum radius extracted from IVUS images in polar coordinates. Edges are computed with a first derivative of a Gaussian over images filtered with a Restricted Anisotropic Diffusion (RAD) and longitudinal cuts serve to remove the intima layer. In order to interpolate curve segments, they use restricted anisotropic operators to extend a mask function of the unconnected set of points. By changing the boundary conditions of the diffusion process to Dirichlet, so that the evolving function is forced to take the values of the initial mask at the curve segments to be joined, the Anisotropic Contour Closing (ACC)is modeled. The statistics on the maximum and mean positioning error show that their segmentation is optimal in cases which the adventitia is thoroughly described as an edge.

The process yields an implicit level sets model of the adventitia that captures curvatures as it bases on the image local orientation (figure 3.1).

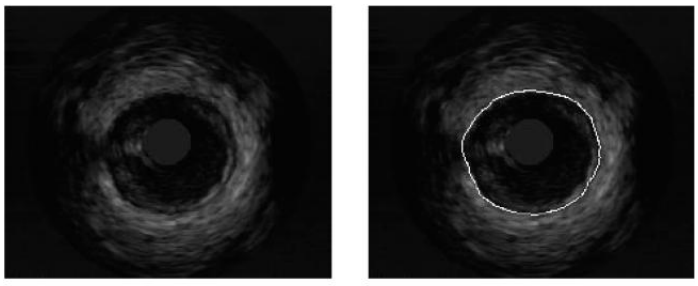

Figure 3.1.: Adventitia Models (b), of the original (a) [34].

A method for the automated detection of lumen and media-adventitia border in sequential intravascular ultrasound (IVUS) frames was proposed in [69]. The method basis was to use deformable models. The energy function is appropriately modified and minimized

with the use of a Hopfield neural network. Proper modifications in the definition of the bias of the neurons have been introduced to incorporate image characteristics. A simulated annealing scheme is included to ensure convergence at a global minimum. The method overcomes distortions in the expected image pattern, due to the presence of calcium, employing a specialized structure of the neural network and boundary correction schemas which are based on a priori knowledge about the vessel geometry. By exploiting the similarities of sequential frames, minimum user interaction is required only for the first frame of the sequence, where the user must provide an initial estimation for the lumen and the media-adventitia borders.

This second-generation segmentation method can be applied automatically on a sequence of IVUS frames to extract the regions borders of interest.

The introduction of a new expression for the image energy makes the method robust, resulting in accurate boundaries for all images, regardless of the presence of noise or weak edges, that are common in IVUS. In a sequence of frames obtained from the same arterial segment, each IVUS frame can be considered quite similar to the previous one.

In the minimization of a deformable model, energy function must be applied twice for each frame (once for each border) and the detected contours in the current frame are used as the initial estimation for the next frame (figure 3.2).

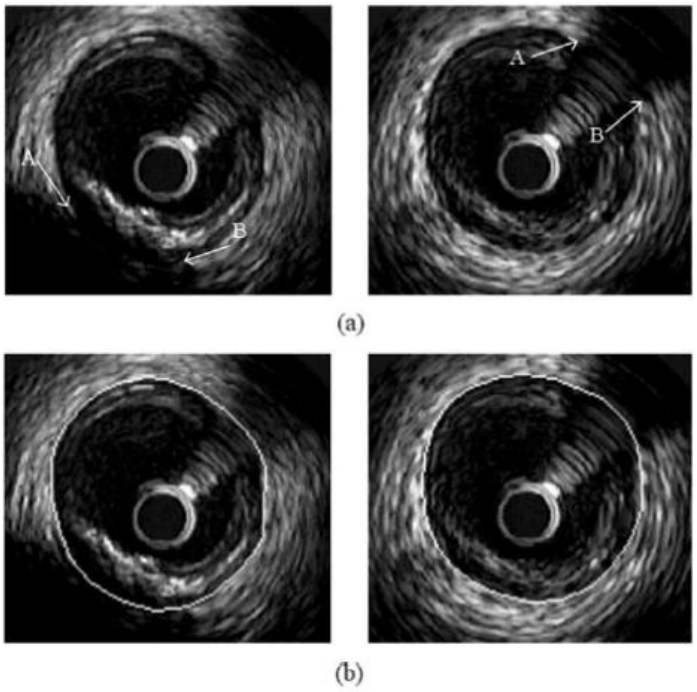

Figure 3.2.: Image with calcified lesion or artifacts. (a) The boundary between media-adventitia is ambiguous in the region between the arrows A and B due to acoustic shadowing or the presence of a guide wire in the image. (b) Detected borders [49].

In [46], a new method to segment the walls of coronary arteries in IVUS images was proposed based on a deformable model, which integrates both edge and region information. In this method, the whole image is supposed to have three regions - lumen, vessel wall,

and adventitia plus surroundings, which are separated by two closed contours, the inner and outer boundaries. This method consists of two steps: firstly, the outer vessel wall boundary is detected by minimizing an energy function of the contrast along it; secondly, by minimizing another energy function that considers the different gray-level distributions of the lumen and the vessel wall, and the contrast along the edge between these two regions, the inner vessel wall is located. Dynamic programming was adopted to implement this method (figure 3.3).

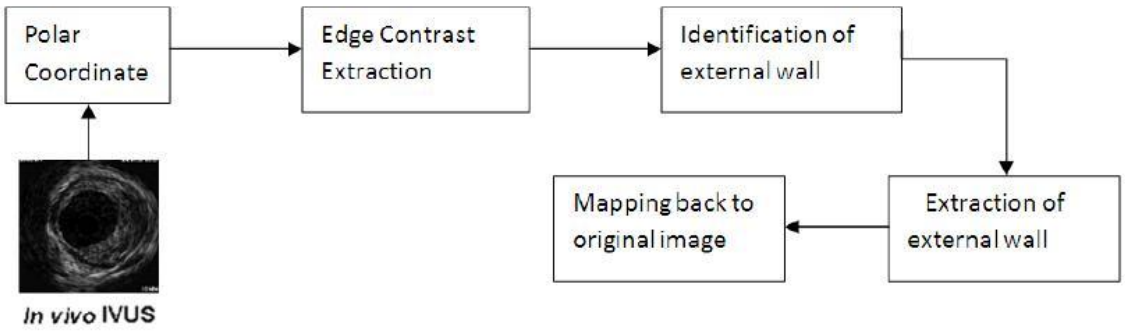

Figure 3.3.: Block diagram of edge contrast method [46].

Spatial continuity along the sequence was provided in some researches [67]. Some of the earlier works on IVUS images segmentation were based on the energy minimization of a contour either by means of guided snake or cost function. In these methods, various optimization algorithms are applied, such as solution of partial differential equations [44], dynamic programming [19], and genetic algorithms [23]. Segmentation methods based on the probabilistic approaches have been proposed in [28], [27]. A modified optimization-based contour detection method was presented in [49] to compute the lumen area of the coronary artery from intravascular ultrasound (IVUS) video images.

First, the search range for the artery inner wall was determined based on the continuity of IVUS video frames. Next, the internal and external energy were calculated to describe the smoothness of the arterial wall and the gray-scale variation of ultrasound images, respectively. Here, a novel form of the external energy which combines the gradient and variance of the intensity of image in the radial direction is used.

Finally, the minimal energy path based on the optimum contour of the artery wall was obtained using circular dynamic programming (DP).

In comparison to the typical DP procedure using the traditional external energy form based on only the image gradient, the reliability of this modified method is considerably improved in the measurement of coronary artery lumen area (figure 3.4). The steps of the modified DP procedure are as follows:

STEP I. Image Preprocessing:

1. Polar transformation of IVUS images-advanced techniques for medical imaging segmentation use a priori knowledge of the target structure shape. In the case of the adventitia border, its circular-like appearance is taken into account by transforming images to polar coordinates with the origin at the geometric center of the vessel border. In this coordinate system, the adventitia is nearly a horizontal curve, which

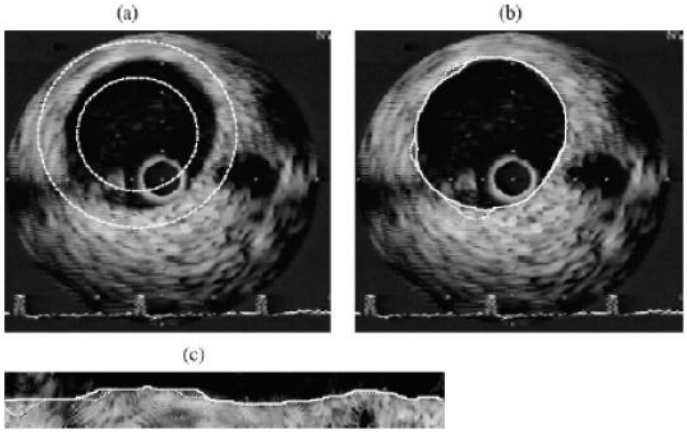

Figure 3.4.: Typical contour detection results respectively using the ordinary and the modified methods. (a) Frame of IVUS images with the delineated (dashed line) annular region for contour detection. (b) Transformed rectangular region and the obtained edge using the ordinary (dotted line) and the modified (solid line) methods. (c) Obtained contours displayed in the original IVUS image [69].

significantly simplifies border feature extraction and parameterization.

2. RAD- In order to enhance significant structures while removing noise and textured tissue, a Restricted Anisotropic Diffusion (RAD) was used. This filtering scheme modifies classic anisotropic diffusions by suppressing any diffusion across image level curves. The associated image operator homogenizes image structures gray values according to their geometric continuity and, thus results in a more uniform response to image local descriptors.

STEP II. Border Points Features Learning: The goal of the selected stage is to compute a mask of vessel border segments and calcium sectors. Extracting vessel borders and calcium points requires defining the functions that best characterize each set, as well as their most discriminating parameter values.

They learned both feature space and parametric threshold values by applying supervised classification techniques to a training set of manually segmented images.

1. Feature Space Design - their feature space is designed to discriminate among the set adventitia/intima, calcium, and fibrous tissue. Calcium sectors are discarded by their tissue shadow and adventitia. Fibrous tissue is discriminated by its similar appearance to vessel borders. By the chosen polar coordinates, horizontal edges are the main descriptors of the set adventitia/intima. Image simple statistics serve to formulate the functions characterizing calcium and fibrous plaque.

2. Parameters Determination - in their segmentation procedure, there are two kinds of parameters, those that best discriminate among different structures in the feature space and those controlling filtering of fake responses. Discriminating parameters are thresholding values on the feature space, while length filtering removes spurious detections from the extracted segments. Both parameters are tuned to yield an optimal segmentation for a training set of manually traced borders.

STEP III. Segmentation Stage: The selection stage produces two binary images: adventitia/intima points and calcium sectors.

Vessel border segments are modeled by computing an implicit closed representation and then an explicit snake representation using B-Splines.

1. Implicit ACC - for the implicit closing, using an ACC based on functional extension principles to complete curve segments in the image mask domain was suggested. The use of restricted diffusion operators enables to take into account image geometry, restore curved shapes, and discard calcium and side branch sectors. Three-dimensional (3D) continuity was endowed to such implicit reconstruction by topological area considerations.

2. Explicit B - Snakes Representation- the vessel contours at uncompleted segments (e.g. branches or calcification) by approaching ACC with a B-spline snake encoded with control points was defined.

A new three-dimensional (3D) IVUS segmentation model which was based on the fast-marching method and uses gray-level probability density functions (pdf) of the vessel wall structures was developed by Cardinal et al. [12]. Fast-marching is a particular case of the level-set model and consists of evaluating an interface propagating under a unidirectional speed function. In this method, the gray-level distribution of the whole IVUS pullback was modeled with a mixture of Rayleigh pdf. With multiple interface fast-marching segmentation, the lumen, intima plus plaque structure, and media layers of the vessel wall were computed simultaneously. figure 3.5 is the Schematic implementation of the image-formation model.

An *in vivo* IVUS pullback (1) was used to create the vessel geometry (2) $z(x, y)$ is a function representing the acoustic impedance variations; $z(r, \varphi)$ is the acoustic impedance function mapped in polar coordinates; $h(r, \varphi)$ is the polar PSF, with a beam width that is increasing with depth; $\otimes$ is the 2-D-convolution operator; $I(r, \varphi)$ is the simulated polar radio-frequency image; $I_B(r, \varphi)$ is the polar B-mode image, that was computed using the Hilbert transform (HT) of $I(r, \varphi)$; $I_B(x, y)$ is the Cartesian B-mode image or simulated IVUS image. This simulation strategy was repeated for the whole image series of a pullback within a diseased superficial femoral artery.

A shape-driven approach to segmentation of the arterial wall from IVUS images in the rectangular domain was proposed by Gozde et al.[88]. Their first contribution was a shape driven approach to IVUS segmentation. They modeled both the lumen and media-adventitia(*MA*) contour variations within a shape space in the "re-sampled" rectangular domain. Hence, they constrained the lumen and media-adventitia contours to a smooth, closed geometry, which increases the segmentation quality without any tradeoff with a regularizer term, yet with adequate flexibility.

Their second contribution was for the lumen segmentation in which they utilize a non-parametric intensity model based on probability density. Furthermore, they incorporated global image measurements into the intensity model rather than point-wise measurements used in previous methods. The media-adventitia was segmented by employing edge information. They defined an oriented smooth gradient that overcomes noise present in IVUS images. In addition, they developed a method to detect calcifications and branch

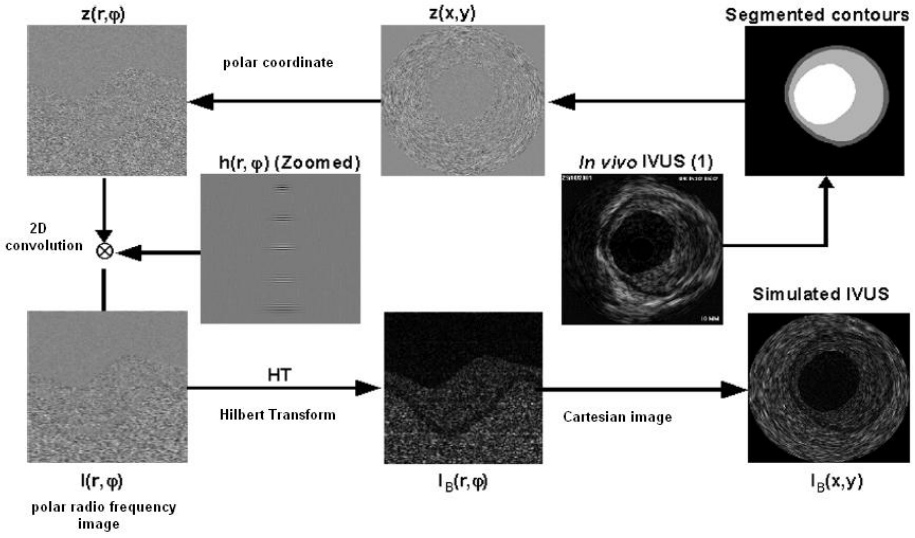

Figure 3.5.: Block diagram of the proposed method of [12].

openings, taking advantage of anatomical characteristics. Incorporating the feature information into the media-adventitia contour extraction greatly enhances their segmentation method.

In this paper the side branches are identified as the openings formed when the vessel was being imaged as bifurcates. This is visualized as an area of dark intensity extending from the lumen in the near field towards the lumen in the far field. The intensity pattern is detectable in the rectangular image domain as a dark intensity segment extending in the vertical direction (figure 3.6).

To detect side branches, the image is divided into n columns, similar to the *MA* initialization, and columns of dark intensity are sought (figure 3.7). The maximum smoothed intensity for every column is noted. From these intensities, the maximum smoothed intensity over the whole image is obtained. A column is classified as a branch opening, if its maximum smoothed intensity is smaller than 20% of the overall maximum intensity.

At the positions of branch opening, the initial *MA* contour is interpolated linearly. Once the initial *MA* contour is interpolated correctly, it is median filtered and the initial shape pose is found. The evolution method of the *MA* shape is not affected by the side branch feature, because in the region of the dark branch opening, there is no high gradient by which the contour can be distracted.

figure 3.8 shows the flowchart of their overall method depending on the side branch feature. In the cases of branch opening, the evolution of the luminal contour is delimited by the *MA* contour as shown in figure 3.8. Otherwise, the evolution of the *MA* contour will be constrained by the lumen contour. Table 3.1 shows a survey on different segmentation algorithms for border detection in IVUS images.

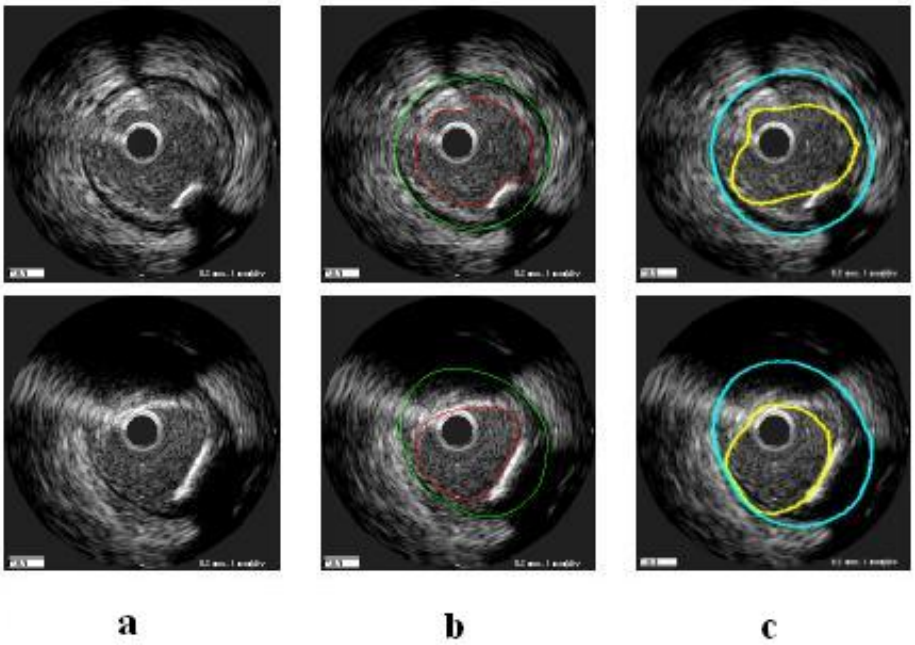

Figure 3.6.: Lumen and *MA* segmentation on a pullback from the Boston Scientific Galaxy probe at 40MHz. (a) Original image (b) Image with doctor-drawn contours (c) Segmentation result. High frequency probe pullbacks pose more challenges to the algorithm, as can be seen in these images [88].

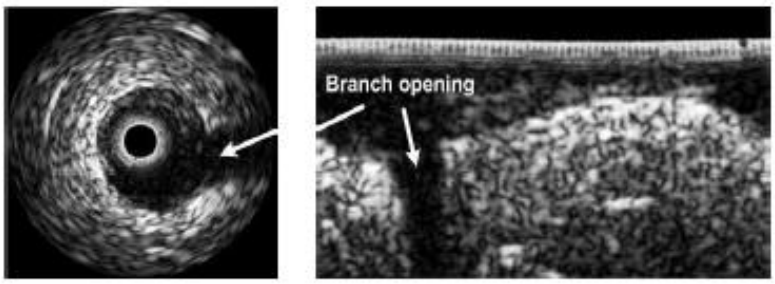

Figure 3.7.: Branch opening in display and rectangular domain[88].

Table 3.1.: A survey on segmentation algorithms

Generation	Main Method	Title	Authors	Year
1st	Region growing	Lumen Detection in Human IVUS Images Using Region-Growing. Computers in Cardiology.	P.A. Brathwaite, B. Chandran, D.D. McPherson, E.L. Dove.	1996
		A Novel Region Growing Method for Segmenting Ultrasound Images. IEEE Ultrasonics Symposium.	X. Hao, C. Bruce, C. Pislaru, J.F. Greenleaf.	2000
2nd	Edge following/ Multiscale edge following	Automated Segmentation of Coronary Wall and Plaque from Intravascular Ultrasound Image Sequences. Computers in Cardiology.	M. Sonka, M.X.Z. Siebes, S. Dejong, C.R. McKa, S.M. Collins.	1994
		A Multiscale Dynamic Programming Procedure for Boundary Detection in Ultrasonic Artery Images. IEEE Transactions on Medical Imaging.	Q. Liang, I.Wendelhag, J. Wikstrand, , T. Gustavsson.	2000
	Statistical/ C-means Clustering	Bayesian Contour Detection in a Time Series of Ultrasound Images Through Dynamic Deformable Template Models. IEEE Transactions on Image Processing.	M.B. Hansen, J. Moller, F.A. Togersen.	2002
		Fully Automatic Luminal Contour Segmentation in Intracoronary Ultrasound Imaging: a Statistical Approach. IEEE Transactions on Medical Imaging.	E. Brusseau, C.L. de Korte, F. Mastik, J. Schaar, A.F.W. van der Steen	2004
		Detection of Luminal Contour Using Fuzzy Clustering and Mathematical Morphology in Intravascular Ultrasound Images. Annual International Conference of the IEEE Engineering in Medicine and Biology.	E. Dos Santos, M. Yoshizawa, A. Tanaka, Y. Saijo, T. Iwamoto.	2005
		On the Usefulness of Supervised Learning for Vessel Border Detection in Intravascular Imaging. Frontiers in Artificial Intelligence and Applications	A. Hernandez, D. Gil, P. Radeva.	2005
	Region based	Estimating Coronary Artery Lumen Area With Optimization based Contour Detection. IEEE Transactions on Medical Imaging.	Z. Luo, Y. Wang, W. Wang. .	2003
		Anisotropic Processing of Image Structures for Adventitia Detection in Intravascular Ultrasound Images. Computers in Cardiology.	A.H. Hernandez, D.G. Gil1, P.R. Radeva1, E.N. Nofrerias.	2004
		Multi Agent Segmentation of IVUS Images. The Journal of the Pattern Recognition Society.	E.G.P. Bovenkamp, J. Dijkstra, J.G. Bosch, J.H.C. Reiber.	2004
3th	High level knowledg e driven	Segmentation of Intravascular Ultrasound Images, a Machine Learning Approach Mimicking Human. International Congress Series.	M.E. Olszewski, A. Wahle, S.C. Vision, Mitchell, M. Sonka	2004
		Shape Driven Segmentation of the Arterial Wall In Intravascular Ultrasound Images, IEEE Transactions on Information Technology in Biomedicine.	G. Unal, S. Bucher, S. Carlier, G. Slabaugh, T. Fang, K. Tanaka	2008

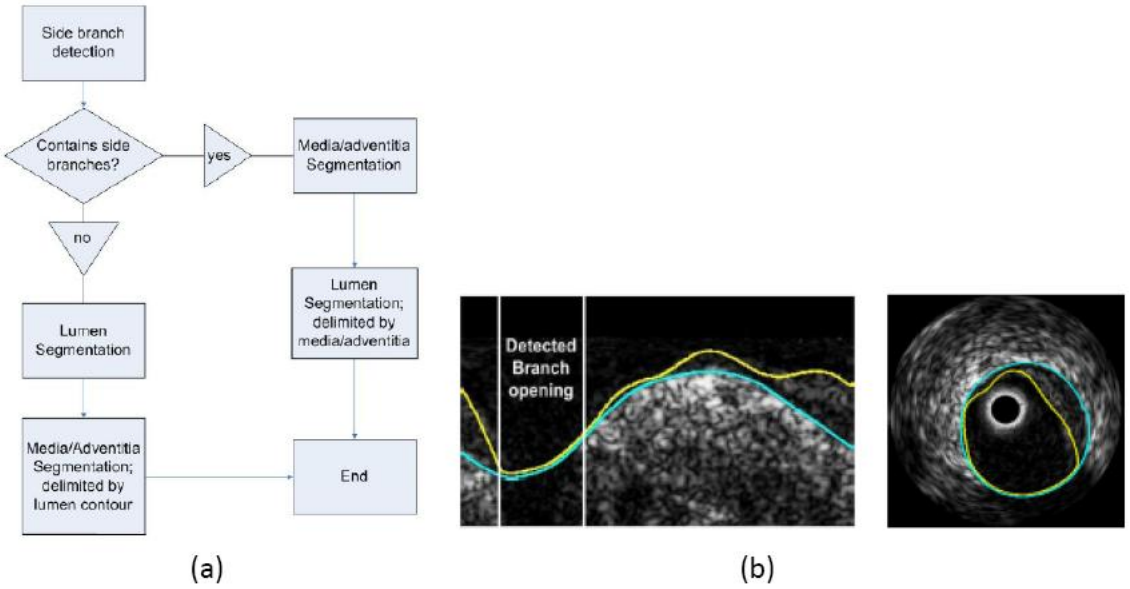

Figure 3.8.: (a)The order in which the segmentation algorithms are executed depends on whether branch openings have been detected or not.(b) Interpolated branch opening in the rectangular and display domain; lumen is delimited by the *MA* [88].

3.2. Proposed Method for IVUS Border Detection

3.2.1. Introduction

Medical images are often corrupted by noise and sampling artifacts, which can cause considerable difficulties when applying classical segmentation techniques such as edge detection and thresholding. As a result, these techniques either fail completely or require some kind of post-processing steps to remove invalid object boundaries in the segmentation results. To address these difficulties, deformable models have been extensively studied and widely used in medical image segmentation with promising results.

Deformable models are curves or surfaces defined within an image domain that can move under the influence of internal forces, which are defined within the curve or surface itself, and external forces, which are computed from the image data.

The internal forces are designed to keep the model smooth during deformation. The external forces are defined to move the model toward an object boundary or other desired features within an image. By constraining extracted boundaries to be smooth and incorporating other prior information about the object shape, deformable models offer robustness to both image noise and boundary gaps and allow integrating of boundary elements into a coherent and consistent mathematical description. Such a boundary description can then be readily used by subsequent applications. Moreover, since deformable models are implemented on the continuum, the resulting boundary representation can achieve subpixel accuracy, a highly desirable property for medical imaging applications. The term deformable models first appeared in the work by Terzopoulos and his collaborators in the late eighties [84]. The popularity of deformable models are largely due to the sem-

inar paper "Snakes: Active Contours" by Kass, Witkin, and Terzopoulos [36]. Since its publication, deformable models have grown to be one of the most active and successful research areas in the image segmentation. Various names, such as snakes, active contours or surfaces, balloons, and deformable contours or surfaces have been used in the literature to refer to the deformable models. However, there are basically two types of deformable models: parametric deformable models and geometric deformable models.

Parametric deformable models represent curves and surfaces explicitly in their parametric forms during deformation. This representation allows direct interaction with the model and can lead to a compact representation for fast real-time implementation.

However, adaptation of the topology model, such as splitting or merging parts during the deformation, can be difficult using parametric models.

Geometric deformable models, on the other hand, can handle topological changes naturally. These models, based on the theory of curve evolution [78] and the level-set method represent curves and surfaces implicitly as a level-set of a higher-dimensional scalar function.

Their parameterizations are computed only after complete deformation, thereby to low topological adaptively to be accommodated easily. Despite this fundamental difference, the underlying principles of both methods are similar.

3.2.2. Preprocessing

The anisotropic diffusion filter is used to de-speckle the medical ultrasound images; this method preserves the features and enhances the edges [52], [25]. There are some parts of the image in the IVUS frames that are not important from the image processing point of view, for example, the calibration and the scale marks. These regions along with the bright catheter ring artifact are replaced by the neighboring gray values. Furthermore, because of more or less circular structures of the vessels, the planar image in the Cartesian coordinates is converted into the Polar coordinates in order to facilitate the detection steps such as the contour initialization. The initial contours used in the deformable models have to be as near as possible to the real borders. For detecting an initial contour for intima, the intensity information is used for thresholding. This is done by sweeping the pixels starting from the center of the catheter toward the image borders on a constant angle on a radius *(r)* while the angle is constant. $I(r, \theta)$ denote the intensity of a pixel located in a radius of r and an angle of θ in polar coordinate. If $I(r, \theta) > T$, where T is the threshold value for intensity, then this pixel will be assumed as a point on the initial border. The value of T is empirically set to 42. figure 3.9(b) illustrates the intima's initial contour. For the media-adventitia initial contour, the image is first filtered using a 3×3 low pass filter with a sigma value equal to unity. Then a canny edge detection operator with $\alpha = 8$ is applied to each frame in Polar coordinate. An example result is shown in figure 3.9(a). After the initial border detection step, the images are converted back to the Cartesian coordinates for further processing.

3.2.3. Parametric Deformable Models

The basic premise of the energy minimizing formulation of deformable contours is to find a parameterized curve that minimizes the weighted sum of internal and potential energy.

Figure 3.9.: (a) Initial contour for media-adventitia border, (b) initial contour for Intima border.

The internal energy specifies the tension or the smoothness of the contour. The potential energy is defined over the image domain and typically possesses local minima at the image intensity edges occurring at object boundaries (figure 3.10). Minimizing the total energy yields internal and potential forces. Internal forces hold the curve together (elasticity forces) and keep it from bending too much(bending forces). External forces attract the curve toward the desired object boundaries. To find the object boundary, parametric curves are initialized within the image domain, and are forced to move toward the potential energy minima under the influence of both these forces.

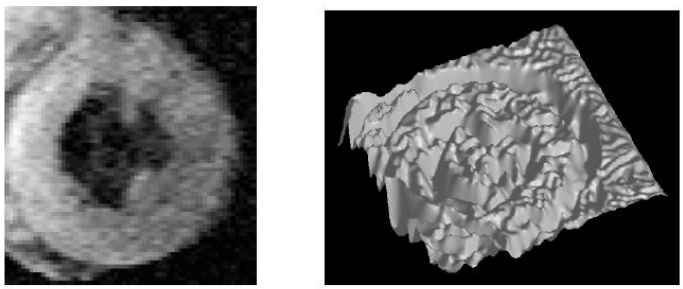

Figure 3.10.: (a) A 2D MR image of the heart left ventricle, (b) A potential energy function derived [101].

Mathematically, a deformable contour $R(s)$ is a curve:

$$R(s) = (X(s), Y(s)), s \in [0, 1] \tag{3.1}$$

that moves through the spatial domain s of an image I to minimize the following energy function:

$$E(R) = E_{internal}(R) + E_{potential}(R) \tag{3.2}$$

The first term is the internal energy function and is defined to be:

$$E_{internal}(R) = \frac{1}{2}\int_0^1 (\alpha(s)|\frac{\partial R}{\partial s}|^2 + \beta(s)|\frac{\partial^2 R}{\partial s^2}|^2)\, ds \tag{3.3}$$

The first-order derivative discourages stretching and makes the model behave like an elastic string. The second-order derivative discourages bending and makes the model behave like a rigid rod. The weighting parameters $\alpha(s)$, $\beta(s)$ can be used to control the strength of the model's tension and rigidity respectively. In practice, $\alpha(s)$, $\beta(s)$ are often

chosen to be constants. The second term is the potential energy function and is computed by integrating a potential energy function $P(x, y)$ along the contour $R(s)$:

$$E_{potential}(R) = \int_0^1 P(R(s))\, ds \tag{3.4}$$

The potential energy function $P(x, y)$ derived from the image data and takes smaller values at object boundaries as well as other features of interest. Given a gray-level image $I(x, y)$ viewed as a function of continuous position variables (x, y), a typical potential energy function designed to lead a deformable contour toward step edges is:

$$P(x, y) = -W_e|\nabla[G_\sigma(x, y) * I(x, y)]|^2 \tag{3.5}$$

Where W_e is a positive weighting parameter, $G_\sigma(x, y)$ is a two-dimensional Gaussian function with standard deviation σ, ∇ is the gradient operator, and $*$ is the 2D image convolution operator. If the desired image features are lines, then the appropriate potential energy function can be defined as follows:

$$P(x, y) = -W_l[G_\sigma(x, y) * I(x, y)] \tag{3.6}$$

Where W_l is a weighting parameter. Positive W_l is used to find black lines on a white background, while negative W_l is used to find white lines on a black background. For both edge and line potential energies, increasing σ can broaden its attraction range. Regardless of the selection of the exact potential energy function, the procedure for minimizing the energy function is the same. The problem of finding a curve $R(s)$ that minimizes the energy functional E is known as a variation problem. It has been shown that the curve that minimizing E must satisfy the following Euler-Lagrange equation [101]

$$\frac{\partial}{\partial s}(\alpha\frac{\partial R}{\partial s}) - \frac{\partial^2}{\partial s^2}(\beta\frac{\partial^2 R}{\partial s^2}) - \nabla P(R) = 0 \tag{3.7}$$

To gain some insight about the physical behavior of deformable contours, we can view equation 3.7 as a force-balanced equation

$$F_{internal}(R) + F_{potential}(R) = 0 \tag{3.8}$$

where the internal force is given by

$$F_{internal}(R) = \frac{\partial}{\partial s}(\alpha\frac{\partial R}{\partial s}) - \frac{\partial^2}{(\partial^2 s)(\beta\frac{\partial^2 R}{\partial s^2})} \tag{3.9}$$

and the potential force is given by

$$F_{potential}(R) = -\nabla P(R) \tag{3.10}$$

The internal force $F_{internal}(R)$ discourages stretching and bending while the potential force $F_{potential}(R)$ pulls the contour toward the desired object boundaries. The forces are defined and derived from the potential energy function $P(x, y)$ given in either equation 3.5 or equation 3.6, as Gaussian potential forces. To find a solution to equation 3.7, the deformable contour is made dynamic by treating $R(s)$ as a function of time t as well as s-

i.e. $R(s,t)$. The partial derivative of R with respect to t is then set equal to the left-hand side of equation 3.7 as follows:

$$\gamma \frac{\partial R}{\partial s} = \frac{\partial}{\partial s}(\alpha \frac{\partial R}{\partial s}) - \frac{\partial^2}{\partial s^2}(\beta \frac{\partial^2 R}{\partial s^2}) - \nabla P(R) \tag{3.11}$$

The coefficient γ is introduced to make the units on the left side consistent with the right side. When the solution $R(s,t)$ stabilizes, the left side vanishes and we achieve a solution of equation 3.7. We note that this approach of making the time derivative term vanished is equivalent to applying a gradient descent algorithm to find the local minimum of equation 3.2. Thus, the minimization is solved by placing an initial contour on the image domain and allowing it to be deformed according to equation 3.11. Figure 3.11 shows an example of recovering the left ventricle wall using Gaussian potential forces.

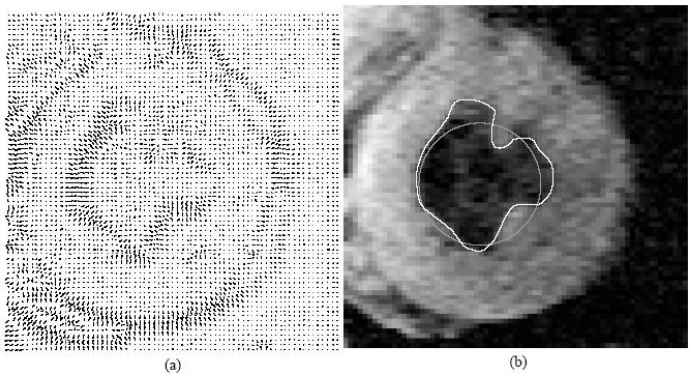

Figure 3.11.: An example of recovering the left ventricle wall using Gaussian potential forces. (a) Gaussian potential forces and (b) the result of applying Gaussian potential forces to a deformable contour, with the circular initial contour shown in gray and the final deformed contour in white [101].

So the algorithm involves firstly initializing a set of snake points defined in the preprocessing step from which the iterative process then begins. The parameters of this algorithm were set to the following weights: $\alpha = 0.5, \beta = 0.5, \gamma = 4.2$. These values are defined through an optimization procedure using the results of the border detection method applied to 30 different images (used as the training set) and comparing them to the manually defined borders by experts. The snake algorithm ends when the zero snake points are moved to new positions for five consecutive iterations (figure 3.12).

3.2.4. Geometric deformable models

Let us consider a dynamic curve as $R(s,t) = [X(s,t), Y(s,t)]$ where t is the time and s is the curve parameter also to denote the curve's inward normal unit as N and its curvature as k. The evolution of the curve along its normal direction can be characterized by the following partial differential equation:

$$\frac{\partial R}{\partial t} = V(k).N \tag{3.12}$$

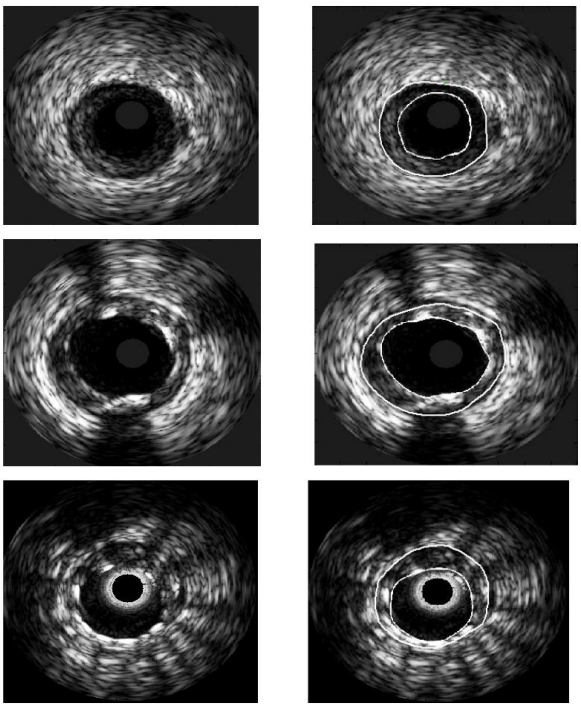

Figure 3.12.: First row a fibro-lipid plaque image and its result, second row calcified image, third row an image with struts of stent and its results with parametric deformable models.

Where $V(k)$ is the speed function as it determines the speed of the curve evolution. The basic idea of the geometric deformable model is to couple the speed of deformation (using curvature and/or constant deformation) with the image data, so that the evolution of the curve stops at object boundaries. The evolution is implemented using the level-set method. Thus, the majority of the researches in geometric deformable models has been focused in the design of speed functions. We now review the level-set method for implementing curve evolution.

The level-set method is used to account automatic topology adaptation, and it also provides the basis for a numerical scheme using by geometric deformable models. In the level-set method, the curve is represented implicitly as a level-set of a 2D scalar function which is usually defined on the same domain as the image itself. The level-set is defined as the set of points having the same function value. Figure 3.13 shows an example of embedding a curve as a zero level-set.

It is worth noting that the level-set function is different from the level-sets of images, which are sometimes used for image enhancement. The sole purpose of the level-set function is providing an implicit representation of the evolving curve. Instead of tracking a curve through time, the level-set method evolves a curve by updating the level-set function at fixed coordinates through time. This perspective is similar to that of an Eulerian motion formulation as opposed to a Lagrangian formulation, which is analogous to the parametric deformable model. A useful property of this approach is remaining the level-set as valid function while the embedded curve can change its topology. This situation is depicted in figure 3.14.

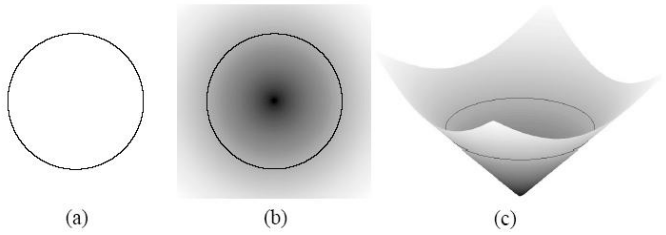

Figure 3.13.: An example of embedding a curve as a level-set. (a) A single curve. (b) The level-set function where the curve is embedded as the zero level-set (in black). (c) The height map of the level-set function with its zero level-set depicted in black [80].

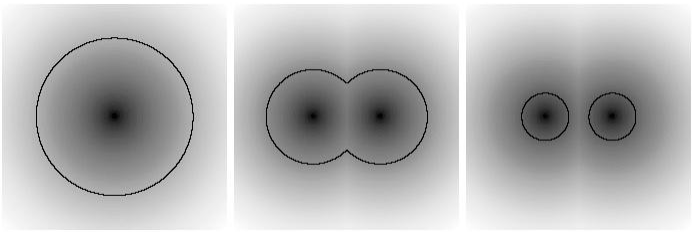

Figure 3.14.: From left to right, the zero level-set splits into two curves while the level-set function still remains a valid function.

We now derive the level-set embedding of the curve evolution. Given a level-set function $\phi(x, y, t)$ with the contour $R(s, t)$ as its zero level-set, we have $\phi[R(s, t), t] = 0$. By differentiating this term with respect to *t* and using the chain rule, we obtain:

$$\frac{\partial \phi}{\partial t} + \nabla \phi . \frac{\partial R}{\partial t} \tag{3.13}$$

where $\nabla \phi$ denotes the gradient of ϕ, assuming that ϕ is negative inside of the zero level-set and positive outside of it. Equation 3.13 can be rewritten to 3.14 according to inward normal unit to the level-set curve:

$$\frac{\partial \phi}{\partial t} = V(k)|\nabla \phi| \tag{3.14}$$

where *k* the curvature at the zero level-set is given by:

$$K = \nabla . \frac{\nabla \phi}{|\nabla \phi|} = \frac{\phi_{xx}\phi_y^2 - 2\phi_x \phi_{xy} + \phi_{yy}\phi_x^2}{(\phi_x^2 + \phi_y^2)^{\frac{3}{2}}} \tag{3.15}$$

Since the evolution (equation 3.14) is derived for the zero level-set only, the speed function $V(k)$, in general, is not defined on the other level-sets. Hence, we need a method to extend the speed function V(k) to all of the level sets. A speed function that is used by geometric deformable contours, takes the following form:

$$\frac{\partial \phi}{\partial t} = c(k + V_0)|\nabla \phi| \tag{3.16}$$

where [40]

$$c = \frac{1}{1 + |\nabla(G_\sigma * I)|} \tag{3.17}$$

A positive value of V_0 shrinks the curve while a negative V_0 expands it. The curve evolution is coupled with the image data through a multiplicative stopping term. This scheme can work well for objects that have good contrast. However, when the object boundary is indistinct or has gaps like the IVUS image in our case, the geometric deformable contour may leak out because the multiplicative term only slows down the curve near the boundary rather than completely stopping the curve. Once the curve passes the boundary, it will not be pulled back to recover the correct boundary. To overcome this deficiency a new term is added to (equation 3.16) as shown in (equation 3.18)

$$\frac{\partial \phi}{\partial t} = c(k + V_0)|\nabla \phi| + \nabla c \nabla \phi \tag{3.18}$$

The resulting speed function has an extra stopping term $\nabla c \nabla \phi$ that can pull back the contour if it passes the boundary [28], [50].

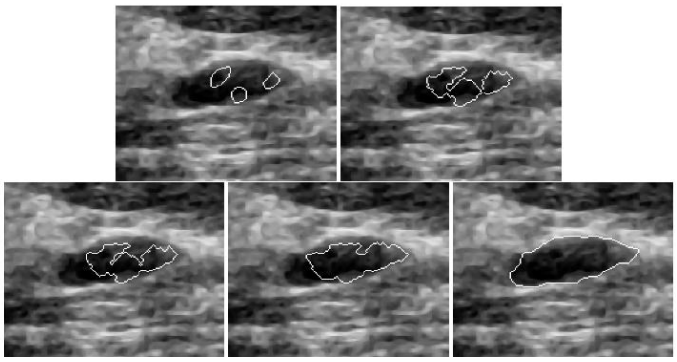

Figure 3.15.: Extraction of cyst form ultrasound breast image via merging multiple initial level sets [101].

This term behaves in similar style to the Gaussian potential force in the parametric formulation. An example of using this type of geometrical deformable contours is shown in figure 3.15. The latter formulation can still generate curves that pass through boundary gaps. Siddiqi et al. [81] partially address this problem by altering the constant speed term through energy minimization, leading to the following geometric deformable contour:

$$\frac{\partial \phi}{\partial t} = \lambda(ck|\nabla \phi| + \nabla c.\nabla \phi) + (c + \frac{1}{2}X.\nabla c)|\nabla \phi| \tag{3.19}$$

In this case, the constant speed term V_0 in equation3.18 is replaced by the second term, and the term $\frac{1}{2}X.\nabla c$ provides additional stopping power that can prevent the geometrical contour from leaking through small boundary gaps.

The second term can be used alone as the speed function for shape recovery as well. Although this model is robust to small gaps, large boundary gaps can still cause problems. At this time, there is no geometric deformable contour model possessing the property of

Table 3.2.: AD is the average distance, HD is the Hausdorff distance (maximum distance), and Area diff is the absolute difference between the automatically detected and manually traced contour for the Intima border. (Automatic1 is the parametric deformable model method and Automatic2 is the geometric deformable model method)

Method	**Area diff(mm^2)**	**HD(mm)**	**AD(mm)**
Automatic1(snake)	7.5367±4.6274	0.8817±0.3115	0.3011±0.2512
Automatic2(level set)	6.2653±4.6274	0.7081±0.2491	0.2031±0.1502
Interobserver variability	5.9312±1.2573	0.6812±0.2107	0.1949±0.0862

convergence to both perceptual boundaries (large boundary gaps) and boundary concavities as there are in parametric deformable contours. The narrow band and fast marching methods are two computationally fast and widely used algorithms for the numerical implementation of the geometric deformable models [94]. Instead of computing the evolution of all level sets, which means all the grid points, the narrow band method consists of just updating a small set of points in the neighborhood of the zero level-set for each iteration. However, the result of this method depends on the position of the initialized curve/surface.

In this work, a new methodology is proposed to solve this problem with choosing right interface positions, so that the complete boundaries of the intima and the media-adventitia are automatically detected.

3.2.5. Result and discussion

The performance of the proposed methods was evaluated using 60 different IVUS images obtained from 7 patients. After applying the nonlinear anisotropic diffusion filter to the IVUS images, intima and media-adventitia of each image was manually traced by two experts. For the performance analysis of the proposed algorithms the Absolute Distance (Area diff.), Average Distance (AD) and the Hausdorff Distance (HD) (i.e. the maximum distance) [27] between the automatically identified boundaries and the expert defined ones are determined and also between the two experts (inter-observer variability).

The results are shown in tables 3.2 and 3.3 for intima and media-adventitia, respectively. The results demonstrate that the variability of the two experts is higher for the intima borders. Detection of the intima is more problematic because of the speckle artifacts and the irregular shape of the intima layer.

It is also obvious that geometric method outperforms the parametric method. The linear regression analysis for the geometric deformable model (figure 3.16) indicates that this method is reliable (*r =0.97*, *y =0.9623 x +1.53* for the media-adventitia and *r =0.96*, *y =0.9137 x +1.3214* for the intima border detection). The slopes are close to unity, the y-interception confidence interval is close to zero and the correlation coefficient is higher than 0.95.

Another parameter for performance analysis used in this work is the William Index (WI) [96], which is the ratio of the average computer-to-observer agreement and the average interobserver agreement [18] as calculated in equation3.20:

Table 3.3.: AD is the average distance, HD is the Hausdorff distance (maximum distance), and Area diff is the absolute difference between the automatically detected and manually traced contour for the Media-adventitia border. (Automatic1 is the parametric deformable model method and Automatic2 is the geometric deformable model method)

Method	**Area diff(mm^2)**	**HD(mm)**	**AD(mm)**
Automatic1(snake)	6.53671232±1.8332	0.5982±0.2510	0.3015±0.0125
Automatic2(level set)	5.0179±3.7915	0.4531±0.3120	0.2132±0.0510
Interobserver variability	4.1253±1.0381	0.5011±0.1287	0.1158±0.1013

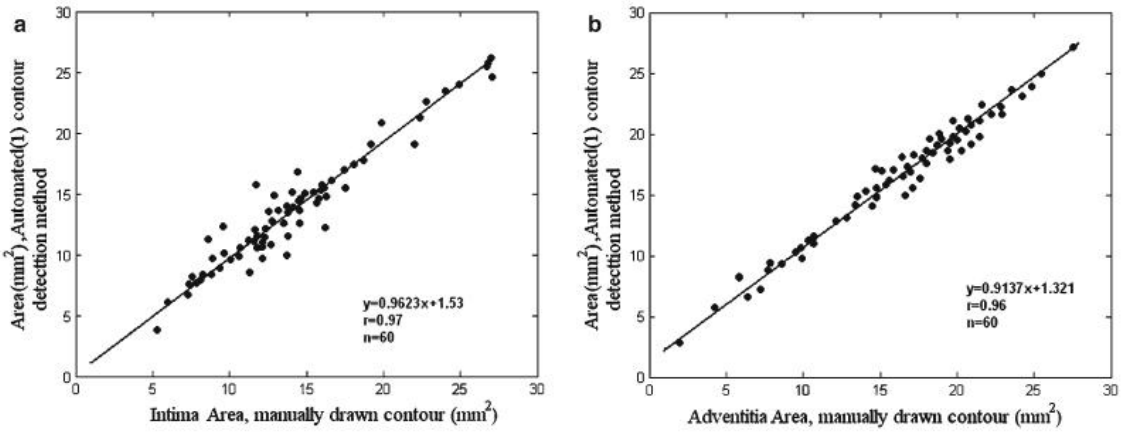

Figure 3.16.: Comparison of (left) media-adventitia and (right) intima cross section areas, segmented with geometric deformable models (n = 60)

$$WI = \frac{\frac{1}{n}\sum_{j=1}^{n}\frac{1}{D_{0,j}}}{\frac{2}{n-1}\sum_{j}\sum_{\acute{j}\neq j}\frac{1}{D_{j,\acute{j}}}} \tag{3.20}$$

where n is the number of observers, $D_{j,\acute{j}}$ is the average inter-observer errors and D_0, j is the average error of the proposed method compared to each of the borders defined by expert. The WI values that are close to unity indicate that the difference between our methods and manually detected ones are not significant, so the proposed methods can be considered as accurate as the experts. The William index for non overlapping areas for the intima in both automated methods were 0.89 and 0.91, and for media-adventitia 0.90 and 0.93, respectively. This discrepancy is caused by the lower inter-observer variability for the media-adventitia which decreases the value of the William index. As expected, these values also illustrate that the second method (geometric deformable model) is more accurate than the first method (parametric deformable model).

4. Chapter Four: State Of The Art In Plaque Characterization

4.1. State of the Art

4.1.1. Introduction

In previous chapters, it it has been mentioned that understanding of plaque composition is a vital step in the evaluation of coronary arteries. The analysis of IVUS data is generally approached in two ways in literature: on one hand, several authors propose the analysis of IVUS images themselves by means of normalization procedures and texture analysis [103], [90], [37]. On the other hand, several researchers prefer the use of the original radiofrequency signal when available [38], [55], [54]. The main advantage of image-based methods is the availability of the images since they are the standard data source of the equipment. In addition, there is a high variety of descriptors which capture the spatial information of gray-level values of a pixel together with its neighborhood in the image.

However, this source suffers from a loss of information and the introduction of artifacts due to the reconstruction process. One of the main problems in image-based techniques is that they do not take into account the plaque size variation (that is meant that all parts of the image are processed with a fixed sweeping window and multi-resolution image processing is missing) [21], [73] and they suffer from high variability among non-normalized DICOM sequences. RF signal represents the ultrasound data better avoiding the introduction of artifacts from the pixel interpolation in the process of image formation. Due to the higher resolution of the unprocessed data, small regions of plaque could be distinguished. However, this kind of data is not easily available and its processing is usually restricted to local spots (i.e. no information about the neighbors is available while processing a spot). In addition, the spatial information is lost when spectral measurements are calculated [21]. Table 4.1 lists some advantages and disadvantages of each approach. However, some researchers mixed image-based and signal-based features for plaque characterization to benefit from the advantages of both approaches while reducing the disadvantages [11], [21].

The main purpose of this chapter is to investigate the basic and newly proposed IVUS image-based and IVUS RF signal-based methods in coronary plaque characterization.

4.1.2. IVUS RF Signal-Based Plaque Characterization Methods

Almost all researchers working on IVUS RF signals for plaque characterization believe that spectral analysis of the radiofrequency (RF) ultrasound signals allows detailed assessment of plaque composition and previous studies have demonstrated the potential of spectral features for discerning plaque components in real time [48], [47]. Thereby, most of IVUS RF signal-based methods are based on spectral features.

Table 4.1.: Advantages and disadvantages of each image-based and RF-based approach for IVUS plaque characterization

	Advantages	**Disadvantages**
Image-based methods	1- Availability 2- Powerful background	1-Loss of information while producing images from ultrasound signals 2- Problems with plaque size variation 3- Problems with high variability among non-normalized DICOM sequences 4- Problems with artifacts resulted from the pixel interpolation in the process of image formation
RF-based methods	1- Higher resolution of the unprocessed data 2- Capability of recognizing small regions of plaques	1- Not easily available 2- Processing is restricted to local spots 3- Loss of spatial information when spectral measurements are applied

Since 2001 [56], Nair et al. have tried to take advantage of conventional spectral features and have added some newly proposed features to do a thorough spectral analysis of IVUS RF for plaque characterization. They accurately classified plaque region into four classes: fibrous, fibro-fatty, necrotic core and calcification. As their method showed high accuracy when validated with histopathology *ex-vivo* and *in-vivo*, it led to Virtual Histology as a surrogate of pathology. Many researches compare the results of their method with this reliable method.

In their method [57], IVUS data were acquired with a Hewlett-Packard SONOS clinical IVUS console (Hewlett-Packard Co.) and 30-MHz, 2.9F, mechanically rotating IVUS catheters (Boston Scientific Corp). Then, IVUS B-mode images were reconstructed from the RF data by custom software (IVUSLab) written by Klingensmith et al. [41]. Software was also developed to maintain the 1:1 correspondence between the reconstructed IVUS and digitized histology images (considered as gold standard in their research), which is essential for the accurate selection of the regions of interest (ROI). The histology images were first registered, scaled, and wrapped by mathematical techniques to fit the corresponding IVUS reconstructed image. The Movat images were used to identify homogeneous ROIs representing the four plaque components, and the corresponding regions were highlighted on the IVUS images in software. Each ROI was 64 backscattered RF data samples in length ($\approx$ 480 μm), and 12$\pm$4 scan lines in width (figure 4.1).

Representative frequency spectrum of each ROI was then calculated by averaging the mathematical autoregressive (AR) model (AR models are qualified for analysis of stochastic, short-time data, such as IVUS backscatter [57]) for each line in the ROI over its width. Then, a normalized spectrum was calculated by subtraction of plexiglas spectrum from averaged ROI spectrum and a least squares regression line was fitted to it. A set of eight spectral parameters that had been identified and validated for IVUS plaque characterization were used to further classify this calibrated spectrum. These are the maximum power and its corresponding frequency, minimum power and its corresponding frequency, slope

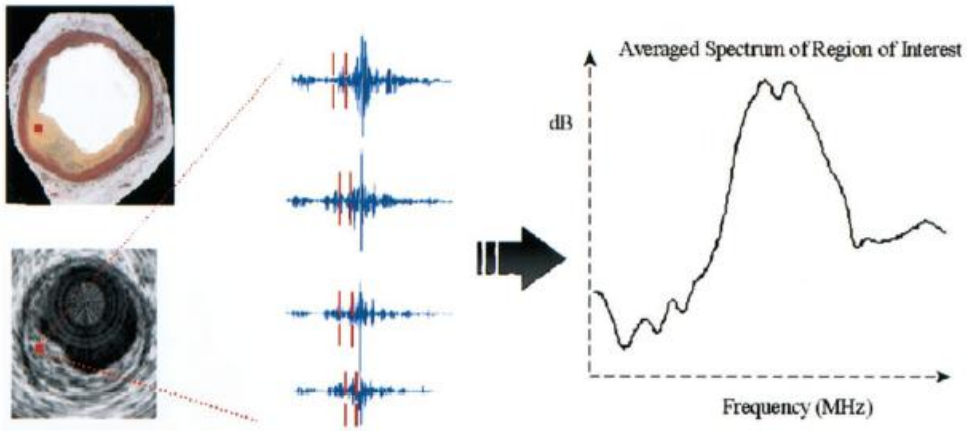

Figure 4.1.: Schematic description of IVUS-histology correlation: ROI of homogeneous plaque component is selected on a histology image; the same region is highlighted on the corresponding reconstructed IVUS image. Signal data representing the region is identified and a power spectrum is calculated after averaging across all 12 scan lines in the region [57].

Table 4.2.: Accuracy of the classified tissues by Nair et al. method (early method)

Tissue Type	Fibrous	Fibro-Lipidic	Calcified	Calcified Necrotic
Accuracy for Training Data	90.4%	92.8%	90.9%	89.5%
Accuracy for Test Data	79.7%	81.2%	92.8%	85.5%

and y-intercept of the linear regression fit to the calibrated spectra, mid-band fit, and the integrated backscatter, all within the bandwidth of 17-42MHz (figure 4.2). Mid-band fit is the power of the regression line at the central frequency of the ultrasound and has been evaluated as a parameter for ultrasonic tissue characterization. Integrated backscatter is defined as:

$$Integrated \;\; Backscatter = \frac{1}{f_{max} - f_{min}} \int_{f_{min}}^{f_{max}} PSD(f)\, df. \tag{4.1}$$

ROIs were then classified using classification trees. Nair et al. believed that classification trees permit use of as many parameters as possible, and this characteristic can be exploited to increase accuracy of the predictions. In addition, classification trees provide a simple means for real-time analysis by lending models that can be programmed in image analysis software. The AR tree (tree classifier based on AR) classified fibrous, fibrolipidic, calcified, and calcified necrotic regions with high predictive accuracies of 90.4%, 92.8%, 90.9%, and 89.5%, respectively, for the training data and 79.7%, 81.2%, 92.8%, and 85.5%, respectively, for the test data. Nair et al. believed that although overlap between fibrous and fibrolipidic regions still occurred, their technique provided an accurate differentiation of focal areas of micro-calcification and necrosis that has an important implication for *in-vivo* assessment of atherosclerotic coronary plaques. They believed that, in contrast to the

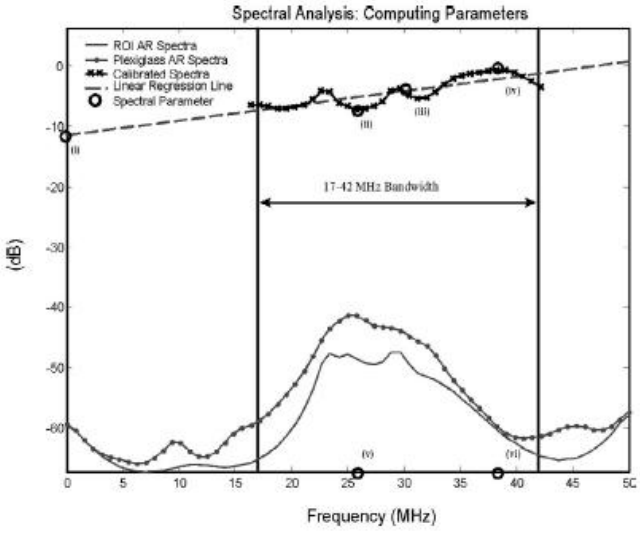

Figure 4.2.: Computing spectral parameters from calibrated spectrum: The averaged spectrum from a region of interest is calibrated, and parameters are computed within the bandwidth of 17-42MHz. The database of parameters then is used to compute the classification tree for plaque characterization (i: y-intercept; ii: minimum power; iii: mid-band fit; iv: maximum power; v and vi: frequencies at minimum and maximum powers, respectively; vii (not shown): slope of regression line; and viii (not shown): integrated backscatter) [55].

standard IVUS display, tissue maps which resulted from their method could differentiate areas of micro-calcifications, heavy calcification, mixed fibrolipidic, and areas of necrosis adjacent to calcification. They also believed that the gray-scale images indicate the overall composition of large homogeneous regions, such as a predominantly calcified area, and they are unreliable in differentiating adjacent smaller areas with heterogeneous composition. It is worth mentioning that coronary atherosclerotic plaques are most frequently heterogeneous. In particular, plaques with a necrotic core, which is an accepted histological finding of unstable plaques, have adjacent areas of micro-calcification and lipid [57].

The shortcoming of their method was that the size of analysis window limited the spatial accuracy of the tissue maps to 480 μm in the axial direction. One of the predominant identifying characteristics of coronary plaques that is vulnerable to rupture is a thin fibrous cap. Although the thickness of this cap is under much debate, a fibrous region $<100\mu$m surrounding an area of necrosis and lipid is a widely accepted marker for vulnerability and the 480 μm analysis window restricts the detection of vulnerable atheromas. Similarly, in artery wall sections with minimal atherosclerotic disease, plaque classification is dependent on analysis of RF data spanning less than 480μm. Therefore, the aim of their new method [55] was to improve the spatial accuracy of the predicted plaque composition to match the axial resolution of 30MHz unfocused IVUS (80-150μm) beyond the 480 μm limit. Although, the use of AR methods could improve the analysis of short-time, stochastic data records such as IVUS backscatter but reduction in the aforementioned window size for analysis of IVUS RF data would make the system prone to perturbations by reducing the signal-to-noise ratio (SNR) in that small window. Nair et al. overcame this shortcom-

ing by regularization, defined as the selection of an appropriate order for the presumed AR process. In the previous studies, AR order was performed using Akaike's final prediction error method, with data records of 480μm (64-sample window) in the spatial domain along each IVUS A-scan. In the new study, the appropriate order for the AR process was estimated by three conventional methods in addition to monitoring the reduction of the mean square error (MSE) of the AR model with the Levinson-Durbin algorithm so that the effect of perturbations may be minimized in the estimated AR coefficients. Data were analyzed in windows of two lengths (240μm and 120μm), which increased the axial spatial accuracy along the IVUS A-scans beyond the original 480μm but within reasonable bounds of available resolution. The best AR order determination technique and the most suitable window size were evaluated using statistical classification trees and their performance in accurately detecting plaque component.

In their method, four order determination techniques were compared to each other:

- The Levinson-Durbin Algorithm
- Final Prediction Error (FPE)
- Akaike's Information Criterion (AIC)
- Minimum Description Length (MDL)

The ROIs were shortened to 32 and 16 samples (0.32μs and 0.16μs round-trip travel time or 240μm and 120μm, respectively) by selecting the middle 32 samples and the middle 16 samples of those 64 sample ROIs. The AR model orders were determined by FPE, AIC, and MDL methods and by monitoring the reduction in MSE with the Levinson-Durbin algorithm. The range of appropriate orders was between 3 and 20 with these four techniques. Hence, spectra for each ROI (analyzed twice in varying lengths of 32 and 16 samples) were calculated with AR coefficients assuming model orders of 3, 5, 10, 15, and 20 using the Burg algorithm in MATLAB and five AR spectra were calculated for both the 32- and 16-sample databases of IVUS backscattered signals.

The average spectrum representing a homogeneous ROI was calibrated then approximated by statistical least squares regression fit and the previous sets of eight spectral parameters were used to further classify this calibrated spectrum. The eight spectral parameters were calculated for each of the five AR spectra calculated from ROI lengths of both 32 and 16 samples. For the two sample lengths, 75% of the data representing each plaque component was randomly selected for computing statistical classification trees using S-Plus (version 3.4, Statistical Sciences, Inc., Seattle,WA). The classification trees then were programmed in MATLAB and cross validated by resolving the type of plaque in the remaining 25% of the test data. The outcomes of these predictions were compared to the known pathologies for each ROI to obtain the corresponding sensitivity, specificity and Youden's Index of the classification trees (for both the training and the cross-validation data sets):

$$Youden's \;\; Index = (Sensitivity + Specifity) - 1 \tag{4.2}$$

Nair et al. believe that the previous validation methods are not efficient since they are only representative of the accuracy of the classification scheme based on the homogeneity of ROI while plaques are very heterogeneous by nature and dividing a plaque into four

tissue components is very difficult due to the amorphous overlap of the tissue components (figure 4.3) [58].

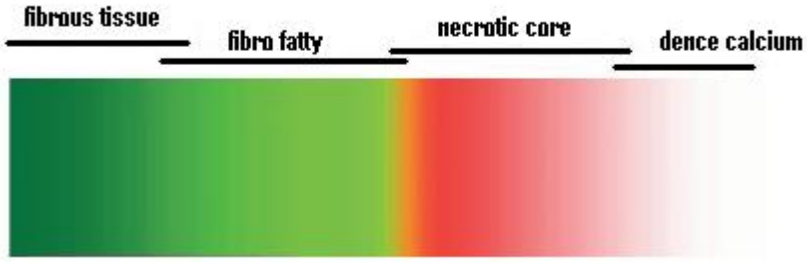

Figure 4.3.: Virtual Histology spectrum illustrates the possible overlap zones between the four plaque component types; fibrous tissue, fibro-fatty, necrotic core and, dense calcium [58].

Hence, in order to better validate their method, they employed a new validation procedure which is more suitable to the heterogeneous nature of the atherosclerotic disease process. The color-coded VH tissue maps derived from spectral analysis and classification scheme were paired with the corresponding matched histology sections and three experts were engaged in the task of systematically and quantitatively dividing each image pair into numerous regions that were individually assessed for accuracy. The process is outlined as follows (figure 4.4):

- The first expert was provided with printouts of the histology images and transparent papers with a grid printed on them with $1/3 \times 1/3$ *mm* squares. Transparent paper was overlaid on each histology printout and the plaque outline was sketched on it. Then, alternating grid boxes that fit the plaque outline were selected as the ROI for accuracy assessment. The plaques that were not thick enough to include at least one complete grid box were excluded from the study. This expert was blinded to the pathology and the VH results.
- The second expert was asked to compare the transparent papers, with the histology outlines and square ROI drawn on the grid, to corresponding VH images. A matching region was identified on the VH images for each ROI on the histology image outlines. ROI that could not be matched were excluded from the study. The expert was then asked to determine the tissue type in the ROI on the VH image based on the rule that the tissue type with the maximum pixels within that ROI be selected as the VH result. This expert was blinded to the true pathology of each ROI.
- The last expert was asked to determine the pathology of each ROI from the histology outlines by examining the original histology studies. This expert was blinded to the VH results including the assessment of the second expert. Finally, a truth-table was constructed with the outcomes of the assessment of the second and the third expert (table 4.3).

Statistical analysis of the truth-table with sensitivity, specificity and predictive accuracy showed that VH characterized atherosclerotic plaque with a combined predictive accuracy

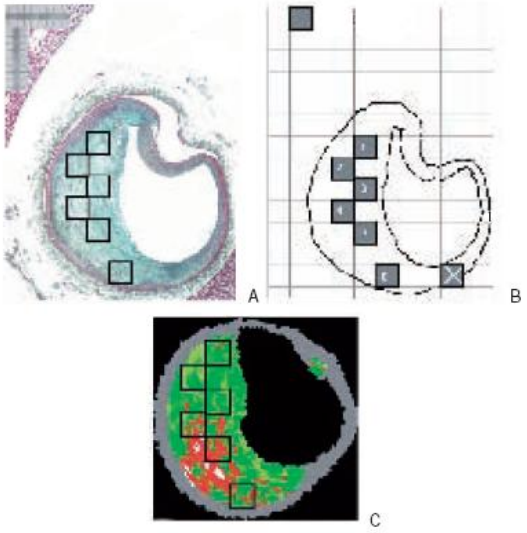

Figure 4.4.: ROI selection for *ex-vivo* accuracy assessment: Three experts were engaged in the separate tasks of (A) interpreting the pathology outcome in all ROI(The experts were blinded to each others' result); (B) drawing histology image outlines on transparent paper with a grid of $1/3\ mm \times 1/3\ mm$ regions and highlighting alternating regions; and finally (C) finding matching regions on corresponding VH images and interpreting the VH outcome in each ROI.

$>$ 93% for all four VH plaque components and at very high sensitivities (72-96%) and specificities (91-99%) (table 4.3).

Nair et al. believe that the VH technique has a tremendous potential to gain clinical importance in the assessment of plaque vulnerability that requires certain level of training and further understanding of VH in relation to clinical end-points. The major limitation of their work is that the window size applied for selection of ROI and eventual tissue map or VH reconstructions is approximately 246 μm in the radial direction that limits the detection of thin fibrous cap $<$ 65 μm in thickness. Also in vessel wall sections with a low extent of disease, plaque classification requires analysis of RF data spanning $<$ 245 μm.

In 2008, Katouzian et al. [38] studied the challenges in atherosclerotic plaque characterization with IVUS backscatters (from data collection to classification). Noting that most pattern recognition approaches for plaque characterization with IVUS backscatters are spectral-based, Katouzian et al. tried to find out how factors such as intrinsic variability among the transducers' spectral parameters and tissue signals may affect the results of the selected pattern recognition method. In their paper, Katouzian et al. categorized the intrinsic challenges into three categories:

1. *In Vitro* setup and specimen preparation: Producing histology images as a gold standard for plaque characterization with IVUS images is a cumbersome task. In the research of Katouzian et al., twenty-five human hearts were studied. They were obtained from two sources: autopsy and transplant surgery, within 24 hour postmortem and explanation, respectively. The artery to be imaged is dissected from the heart and oriented in a tissue cage fixture (figure 4.5).

Table 4.3.: VH Accuracy

VH plaque component	Predictive accuracy	Sensitivity %	Sensitivity CI	Specificity %	Specificity CI
FT (n=471)	93.5%	95.7%	94 - 98	90.9%	88 - 94
FF (n=130)	94.1%	72.3%	65 - 80	97.9%	97 - 99
NC (n=132)	95.8%	91.7%	87 - 96	96.6%	95 - 98
DC (n=156)	96.7%	86.5%	81 - 92	98.9%	98 - 100

FT = fibrous tissue; FF = fibro-fatty; NC = necrotic core; DC = dense calcium; CI = 95% confidence interval

Figure 4.5.: Tissue cage fixture: The artery is fixed in the cage and an automatic pullback is performed in saline and human blood. The histology sections are taken at every 2 mm using side rods after the artery was fixed by formaldehyde[38].

However, with all these difficulties, tissue fixation might alter the acoustic and structural properties of the tissues which may cause problems in interpreting *in-vivo* IVUS images. Imaging of the plaque through blood (*in-vivo* IVUS imaging), which is difficult to simulate *in vitro*, can be expected to introduce signal changes, e.g., attenuation. Thereby, a tissue characterization algorithm developed using *in vitro* data will work on *in-vivo* data to the extent that the tissue signatures remain similar. As long as the differences found in the tissue signatures between the *in vitro* and *in-vivo* imaging situations are consistent, it may still be possible to empirically retune an *in vitro*-trained algorithm and have it perform well *in-vivo*. However, not much is known about the nature of these differences, so they need to be further studied and validated.

2.) Variability of Tissue Signatures: It is a statistically observable fact that on averaging a large number of spectra obtained from homogenous areas of tissue in carefully controlled *in vitro* experiments, different types of tissue give rise to recognizably different spectra. In most recent methods of tissue characterization, the spectrum is summarized using a few numbers of features to capture its basic shape, the so-called spectral signature. For example, Nair et al. used eight spectral signatures (integrated backscatter coefficient, slope, mid-band fit (MBF), intercept, and maximum and minimum powers and their relative frequencies) to characterize different plaques. However, the principal challenge in building a tissue characterization system is to develop a proper definition for tissue signatures that maintain their similarity within each tissue type and distinction between tissue types. This is indeed a challenge since the tissue signatures corresponding to a single tissue type can, in general, be shown to vary across different cross-sectional slices even within the same vessel. The source of such variations can be related to: 1) image formation, such as small changes in the angle of incidence of the ultrasound beam or variations in the geometric configuration of scatterers; 2) genuine changes in physical characteristics within the particular tissue type; and 3) variation in transducer properties that confound the recovery of tissue type from tissue signatures. Figure 4.6 presents the variability in the normalized spectrum across four frames of RF signals acquired from two randomly selected cadaver hearts. The overlapping spectra visually confirm the difficulty that is involved in characterizing these two tissue types on the basis of their spectral signatures. For example, at $20MHz$, for the third frame analyzed, lipidic tissue seems to be well separated from fibrotic tissue. However, if a classifier were built taking into account the $20MHz$ component of the spectra derived from this frame alone, it would be impossible to discriminate between lipidic and fibrotic tissue in another frame.

   Furthermore, transducer's spectral parameters deviated from line to line in the same frame and among distinct frames that cause inter- and intra-frame variations in spectral signatures. Table 4.4 shows the statistical variations of the center frequency and the bandwidth of 12 averaged spectra measured in 12 distinct frames during pullback. The inter- and intra-frames variations of the spectra of transducers are inevitable and can be the source of (large) perturbations in the tissue spectra.

3. Ground Truth: Since the overall justification of *in-vivo* real-time plaque characterization is made by interventional cardiologists through the use of classified tissues, it is indispensable to train the classifier with the most reliable features. Although the his-

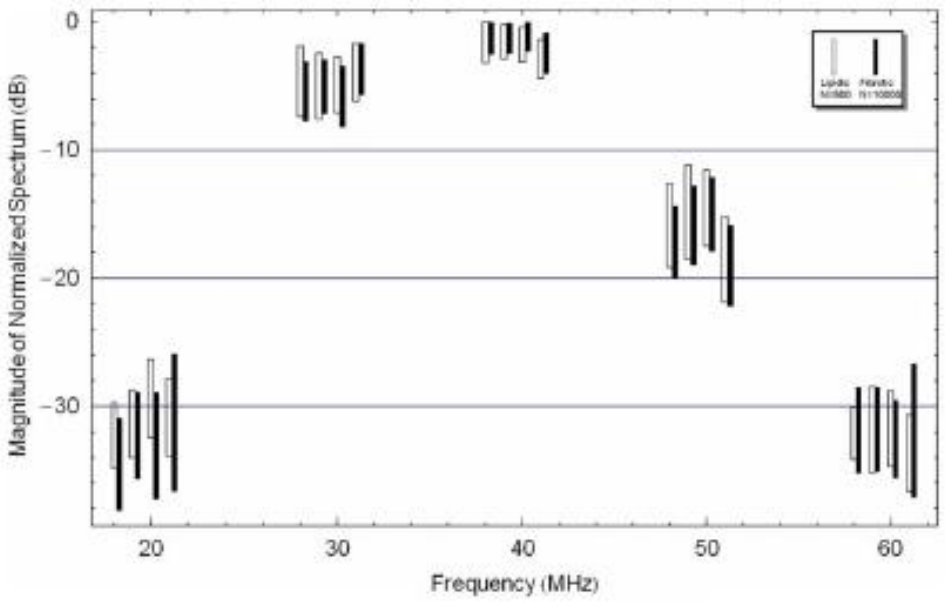

Figure 4.6.: Normalized spectra of two distinct types of plaque tissue found in four cross sections of data from two cadaver hearts. As before, the bars represent the inter-quartile range of variation. The unfilled bars represent lipidic tissue and the filled bars, fibrotic tissue [38].

Table 4.4.: Statistical Variations of transducers' spectral parameters [38].

	Transducer1	**Transducer2**	**Transducer3**
Center frequency (MHz)	34.48 ± 0.14	41.93 ± 0.31	36.46 ± 0.69
Bandwidth at -6 dB (% of center frequency)	29.31 ± 1.64	37.34 ± 2.28	32.32 ± 2.65
Bandwidth at -12 dB (% of center frequency)	59.22 ± 2.82	63.68 ± 3.39	66.79 ± 5.36

tology image is the gold standard, its interpretation can be subjective. Consequently, experts may categorize tissues differently, and as a result, different training data sets may lead to different classification. For example, one can simply categorize tissues as fibrotic, lipid pool, necrotic core and calcium, or one may differentiate between the levels of presence of fatty materials and add fibro-lipid to compromise between fibrotic and lipid. Basically, in order to collect a training dataset, the regions of interest (ROIs) in the arteries are marked and relative cross-sectional histology images obtained. The IVUS-histology frame alignment plays a crucial role in this study because the IVUS frames are labeled through the interpretation of the corresponding histology images. Subsequently, the signals are assigned to labeled tissues and relative features are extracted. The IVUS histology matching problem becomes more challenging due to the: 1) curvature of arteries; 2) registration between an IVUS image and its relative histology since the IVUS imaging plane and the slicing plane of the microtome are somewhat different; and 3) shrinkage of the arteries after formalin fixation. The more the number of ROIs, the more comprehensive signature database is assembled. It is frequently observed that when tissue characterization algorithms are applied to new data (data that is not part of the training set), unsatisfactory results are obtained. This is explained, at least in part, by the fact that the training database is not comprehensive enough, the pattern recognition algorithm has not seen enough examples to learn to recognize new data with sufficient generality.

In spite of the above mentioned shortcomings, Katouzian et al. believed that the atherosclerotic plaque classification could be achievable if: 1) proper features were extracted, with some of them having potential physical grounds and 2) the apposite classification algorithm is deployed. In their method, they used full-spectrum analysis and extract features in the functional range of the bandwidth of the transducers (for a single-element rotating transducer with nominal 40-*MHz* center frequency and 100% bandwidth, this range is measured to be 20-60 *MHz*). The dissimilarities of tissue spectra in this range motivated them to use full-spectrum analysis instead of defining a few numbers of signatures. As the most recognizable difference in the backscattered signals spectra is energy, the energy norm (E_{norm}) was extracted as one of the features that could be a measure for the softness or hardness of the tissue structures. For this reason, signals in the regions behind calcified and necrotic core are attenuated sharply and shadows are often visible behind arcs of calcified plaques. For a given tissue signal of length l ,$X = [x_1, ..., x_l]$, the energy norm is calculated as follows:

$$E_{norm} = ||X|| = \sqrt{X.X^T} \tag{4.3}$$

As a second feature, they extract the radial position (r) of the tissue from the center of the transducer. This feature will help the classifier to incorporate the tissue signals with different attenuations. Then, k-NN and linear Fisher classifiers were applied to the feature space. A sample result is shown in figure 4.7. Confidence was related to distance between feature vector and the decision surface. Both methods show a good correlation between the corresponding histological regions and the classification color outputs.

A useful way to evaluate the accuracy of a classifier is by drawing the receiver-operating-characteristic curve (ROC) that portrays the trade-off between sensitivity and specificity when the threshold is varied. The area under the ROC curve (AUC) is a metric that can be used to rate different classifiers. As suggested by the ROC curves shown in figure 4.8,

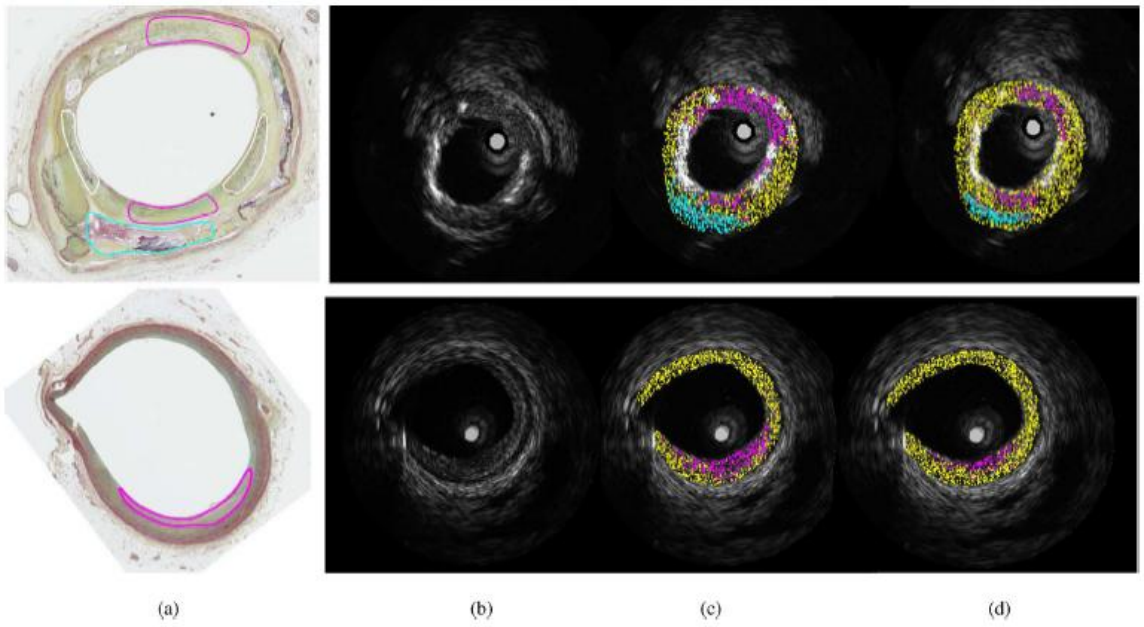

Figure 4.7.: Pictorial illustration of two full-spectrum-based classification methods: (a) Movat Pentachrome histology image. (b) IVUS image. (c) IVUS tissue map generated by Fisher. (d) IVUS tissue map generated by k-NN, k = 5 [38].

it is empirically evident that the process of summarizing the spectrum by specifying the eight spectral signatures previously described reduces discrimination in comparison to a full-spectrum analysis proposed by Katouzian et al.

Although full spectrum analysis holds great potential for accomplishing robust tissue classification, it is solely evaluated for *ex-vivo* data and needs to be further evaluated and quantified for *in-vivo* data. Katouzian et al. hope to quantify the classification results with other methods of characterization (e.g., using the OCT). They believe that evaluation of different classifier performances, reliability of the spectral features, and the complexity of the classification algorithm along with the insufficiency of data are open problems in atherosclerotic plaque characterization that require further studies.

Another IVUS RF signal-based method is the method of Murashige et al.[54] that detects lipid-laden atherosclerotic plaque by wavelet analysis of Radiofrequency Intravascular Ultrasound (RF IVUS) signals. Murashige et al. believed that IVUS imaging provides a detailed arterial cross section with accurate morphometric representation of atherosclerotic plaque dimensions. However, they also believed that there are some limitations in tissue characterization by IVUS intensity patterns alone, especially in discriminating fibrous and fatty tissues and recently, many authors have proposed quantitative tissue characterization methods to overcome these limitations. The tissue characterization method is a wavelet-based method. Wavelet analysis is a new mathematical model for assessing local changes in the geometrical profile of time-series signals. Hence, Murashige et al. tried to study the feasibility of using wavelet analysis of radiofrequency IVUS signals to detect lipid-laden plaque.

In their method, RF IVUS signals were adopted and analyzed by wavelet analysis us-

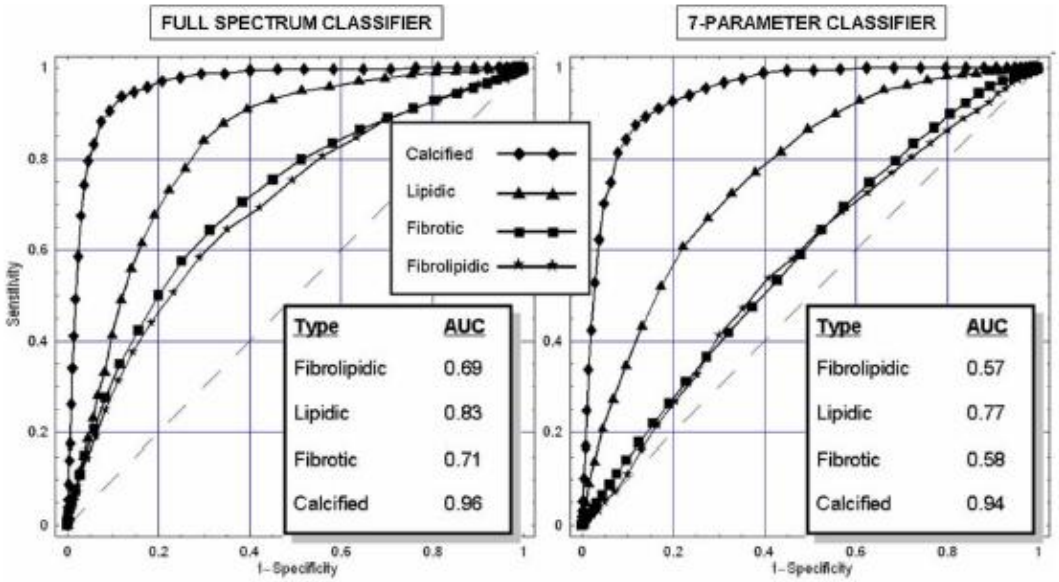

Figure 4.8.: ROC curves comparing the linear separability of full spectral features (left) with that of a reduced set of eight spectral signatures (right); 1451, 475, 10 668, and 382 volumes of 128 samples of fibro-lipidic, lipidic, fibrotic, and calcified tissue signals were used, respectively [38].

ing MATLAB data processing software. Consequently a scale-space pattern of each signal was acquired (figure 4.9). It was noticed that scale-space pattern of signals from different plaque areas are different from each other. Especially wavelet coefficients of lipid-laden patterns between scales 20 and 30 were significantly greater than those of fibrous plaque. The ROC analysis revealed that the optimal value of this wavelet coefficient was 0.6 to discriminate a lipid-laden plaque. Using this criterion, the lipid-laden plaque was detected with a sensitivity of 81% (13 of 16; histological examination from the directional coronary atherectomies revealed that 16 of 29 coronary segments were fat-dominant (lipid-laden) while no apparent fatty area was observed in the remaining 13 segments) and a specificity of 85% (11of 13). Many other wavelet approaches (approximately 50 types) were analyzed, and it was found out that Daubechies-2 wavelet provides the best sensitivity and specificity. Murashige et al. believed that currently, there is no reliable, commercially available device that is capable of discriminating fibrous and fatty areas within atherosclerotic plaque and their new method may be useful in assessing plaque vulnerability in patients with coronary artery disease. They hoped that further evaluation of wavelet analysis in comparison with clinical data and inflammatory markers would be necessary to assess the usefulness of their method in clinical practice to predict future cardiac events in patients with coronary artery disease.

Recently, Kawasaki et al.[63] proposed another RF signal-based method for tissue characterization of coronary plaques. They believed that a parameter called Integrated Backscatter (IB) extracted from backscattered RF signals is noticeably different between different plaque types. Based on IB, Kawasaki et al. classified the plaques into 4 major components:

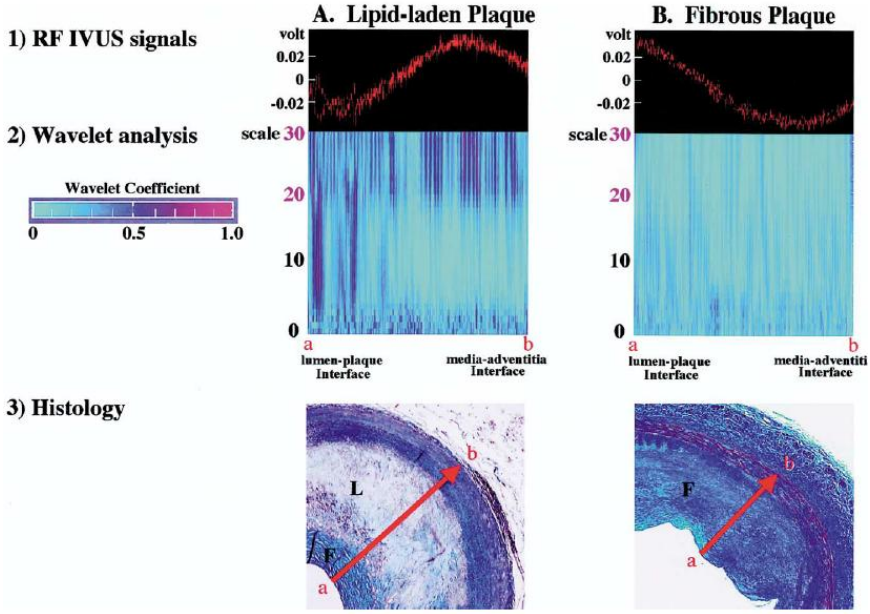

Figure 4.9.: Representative examples of *in vitro* wavelet analysis of RF IVUS signals from a lipid-laden plaque (A) and from a fibrous plaque without a lipid core (B). The upper panels show RF signals, the middle panels show the results of wavelet analysis, and the lower panels show the histological specimen of the corresponding arterial cross section with Masson's trichrome. In the time-scale domain color-coded mapping of wavelet analysis, an apparently different pattern of pink area from an RF signal vector of a lipid-laden plaque is observed between scale 20 and scale 30, compared with the fibrous plaque. F is fibrous area and L is lipid core [54].

fibrous, dense fibrosis, lipid pool, and calcification. After acquiring 256 vector lines per image RF signals (1.4*grades/line*) using a 40*MHz* mechanically rotating IVUS catheter (Atlantis, Boston Scientific, Natick, MA, USA) and digitizing them at 100*MHz* with eight-bit resolution, IB values for each tissue component were calculated as the average power using a fast Fourier transform, measured in decibels (dB), of the frequency component of the backscattered signal from a small volume of tissue. IB value of a stainless steel needle (standard: 0 dB) placed at a distance of $1.5mm$ from the catheter was then subtracted from the tissue IB values for calibration. As the average attenuation using a 40*MHz* frequency catheter was 3 to 6*dB/mm* [7], each IB value was finally corrected adding $0.3dB/0.1mm$ when the ROI was located 1.5 *mm* further from the catheter and subtracting $0.3dB/0.1mm$ when the ROI was located $1.5mm$ nearer to the catheter. In their training study, a total of 724 ROIs $(0.3mm \times 0.3mm)$ with typical histology were examined in the 50 arterial segments to compare the IB values and the typical tissue components, calcification ($n = 144$), fibrosis ($n = 335$) and lipid pool ($n = 205$) were selected. Statistical analysis of IB values showed a significant difference between different components (figure 4.10). According to the statistical analysis, an IB value of ≤ 49 dB (area under curve = 0.98) was the most reliable cut-off point for discriminating lipid pool (90% sensitivity, 92% specificity) and fibrosis (94% sensitivity, 93% specificity) and an IB value of $>$ 29 dB (area under curve = 0.99) was the most reliable cut-off point for discriminating calcification (95% sensitivity, 99% specificity) and fibrosis. Upper values of fibrous region is considered as dense fibrosis (exact cut-off was not reported by the group).

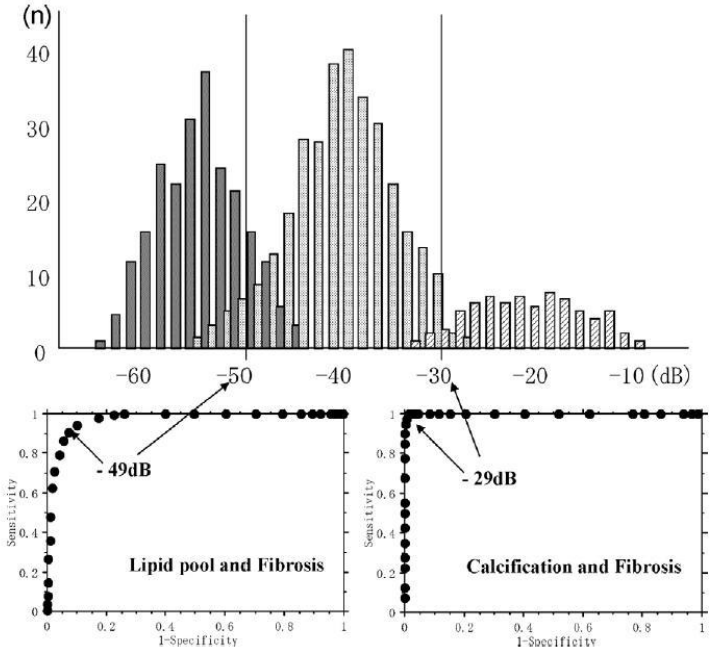

Figure 4.10.: Histogram of integrated backscatter values of each tissue component. According to the receiver operating characteristic curves, the most reliable cut-off points for discriminating each tissue component were determined [63].

Based on these cut-offs a color-coded map of plaque types is extracted from RF signals

in which green indicates fibrous, yellow indicates dense fibrosis, blue indicates lipid pool and red indicates calcification(figure 4.11).

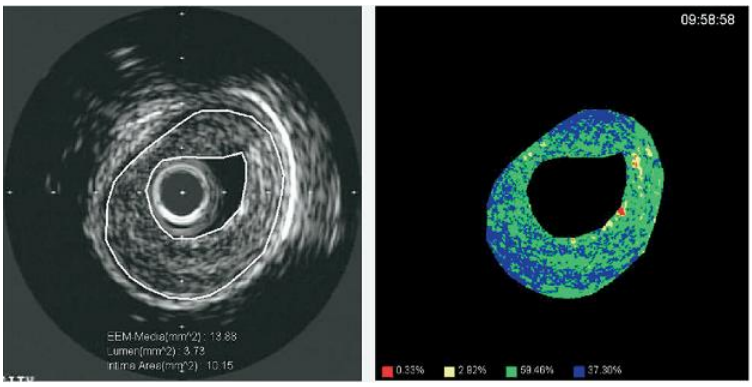

Figure 4.11.: Conventional IVUS images and IB-IVUS color-coded maps [63].

Kawasaki et al. believe that their method outperforms the Nair et al. method in characterising plaque types. In order to prove their claims, Kawasaki et al. performed "qualitative", "direct qualitative", "quantitative" and "direct quantitative" comparisons between IB-IVUS and IVUS-VH images [64]. In the "qualitative" comparison, 150 IB-IVUS and IVUS-VH images were classified into Stray's type III, IV, Va, Vb or Vc by the consensus of 2 IVUS readers who were unaware of the histological diagnoses. They performed a "direct qualitative" comparison by setting small ($0.3 \times 0.3mm$) regions-of-interest (ROIs) on the same sites in both the histological and IVUS images. Histological classification in the direct qualitative comparison was performed as per the previous reports [63]. They then performed the "quantitative" comparison using the following definition. The 150 cross-sections were diagnosed as fibrocalcific, fibrous or lipid-rich by 2 IVUS readers who were unaware of the histological diagnoses. In the IB-IVUS images, the lesions that included calcification (red) and occupied $>$ 1% of the entire cross-section were diagnosed as fibrocalcific, regardless of the %lipid pool area, because a calcified mass can be recognized in the corresponding histological images when the red area was $>$1%. The lesions that included lipid pool (blue) and occupied $>$30%, and calcification (red) that occupied $\leq$1% of the entire cross-section and include a mass of lipid core were diagnosed as lipid rich by IB-IVUS. Otherwise, the lesions were diagnosed as fibrous by IB-IVUS. In the IVUS-VH images, the lesions that included dense calcification (white) that occupied $>$5% of the entire cross-section were diagnosed as fibrocalcific, regardless of the %necrotic core area, because a calcified mass can be recognized in the corresponding histological images when the white area was $>$5%. The lesions that included a necrotic core (red) that occupied $>$10%, and dense calcification (white) that occupied $\leq$5% of the entire cross-section and included a mass of lipid core were diagnosed as lipid-rich, because the percentage of necrotic core (y) indicated by IVUS-VH was approximately one-third of the lipid pool (x) indicated by IB-IVUS ($y = 0.34x$, $r = 0.91$, $p < 0.001$) at the same cross-section. Otherwise, the lesions were diagnosed as fibrous by IVUS-VH. This definition was determined using the remaining 240 of the 392 cross-sections. Furthermore, they performed a "direct quantitative" comparison. Of the 150 histology/IVUS image pairs, were randomly selected 49 pairs in which the histological specimens were clearly stained with Masson's

trichrome with sufficient resolution for quantification. These images were digitized and the areas that were stained blue were automatically selected by a multipurpose image processor (LUZEX F, Nireco Co, Tokyo, Japan). The relative fibrous area (fibrous area/plaque area) was then automatically calculated by the LUZEX F system. They were not able to quantitatively compare the lipid area and necrotic core area because the lipid area and/or necrotic core were partly corrupted and/or melted by the formalin fixation and microtome cuts necessary to the procedure. Of a total of 49 pairs, they selected 45 histology/IVUS image pairs for use in the "direct qualitative" comparison. In these 45 pairs, the shape of the cross-sections was not deformed by the process of formalin fixation, paraffin embedding and microtome cutting. When there were 2 diagnoses in the ROI, the diagnosis that occupied more than half of the area was selected. When there were more than 3 diagnoses in the ROI, the ROI was excluded from the comparison. A total of 141 ROIs were compared. When there was a small gap between the location of the ROIs placed on the IVUS images and histological images, referring to the vascular lumen and outside border, the location of the ROIs (figure 4.12) was adjusted. The results of their comparisons are shown in tables 4.5 and 4.6.

	Histological diagnosis								
	III	*IV*	*Va*	*Vb*	*Vc*	*LR*	*FI*	*FC*	*Total*
Qualitative comparison									
IB-IVUS diagnosis									
III (Preatheroma)	*20*	*0*	*0*	*0*	*0*				*20*
IV (Atheroma)	*7*	*14*	*0*	*0*	*0*				*21*
Va (Fibroatheroma)	*0*	*0*	*21*	*8*	*4*				*33*
Vb (Calcific lesion)	*0*	*0*	*0*	*49*	*0*				*49*
Vc (Fibrotic lesion)	*0*	*0*	*0*	*0*	*15*				*15*
Total	*27*	*14*	*21*	*57*	*19*				*138*
Cohen's κ=0.81 (95%CI: 0.74–0.89)									
IVUS-VH diagnosis									
III (Preatheroma)	*14*	*0*	*0*	*0*	*0*				*14*
IV (Atheroma)	*11*	*12*	*0*	*0*	*0*				*23*
Va (Fibroatheroma)	*0*	*0*	*14*	*6*	*7*				*27*
Vb (Calcific lesion)	*0*	*1*	*1*	*50*	*3*				*55*
Vc (Fibrotic lesion)	*0*	*0*	*4*	*1*	*9*				*14*
Total	*25*	*13*	*19*	*57*	*19*				*133*
Cohen's κ=0.66 (95%CI: 0.56–0.75)									
Quantitative comparison									
IB-IVUS diagnosis									
LR						*60*	*8*	*4*	*72*
FI						*1*	*15*	*0*	*16*
FC						*1*	*0*	*49*	*50*
Total						*62*	*23*	*53*	*138*
Cohen's κ=0.83 (95%CI: 0.75–0.91)									
IVUS-VH diagnosis									
LR						*52*	*7*	*5*	*64*
FI						*4*	*12*	*1*	*17*
FC						*2*	*3*	*47*	*52*
Total						*58*	*22*	*53*	*133*
Cohen's κ=0.73 (95%CI: 0.63–0.83)									

IVUS, intravascular ultrasound; LR, lipid-rich; FI, fibrous; FC, fibrocalcific; IB, integrated backscatter; CI, confidence interval; VH, virtual histology.

Table 4.5.: Qualitative and Quantitative Comparison of the IVUS and Histological Diagnoses.

However, their method has the common disadvantages of signal-based methods and the validity of their comparison was not analyzed.

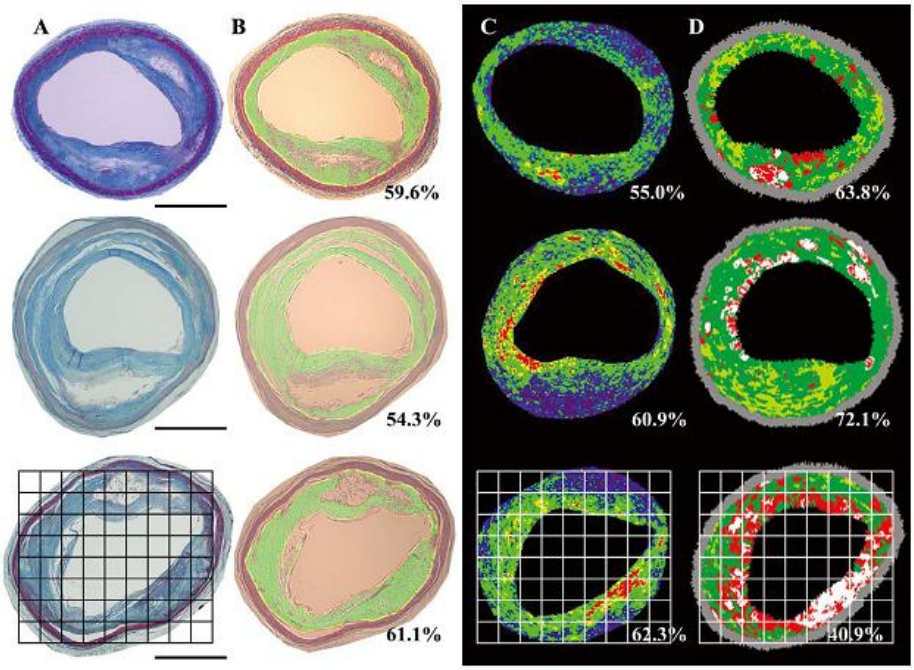

Figure 4.12.: Representative lesion used in the direct comparison study. (A) Histological images stained with Masson's trichrome. Bar=$1mm$. (B) Images after quantification by the image processor. Areas stained blue by Masson's trichrome staining were automatically selected (green area) by the multipurpose image processor (LUZEX F) and the relative fibrous area (fibrous area/plaque area) was automatically calculated by the system. (C) Integrated backscatter-intravascular ultrasound (IVUS) images corresponding to sections analyzed by histology. (D) IVUS-Virtual Histology images corresponding to sections analyzed by histology. Percentages indicate the relative fibrous areas determined by each method. A "direct qualitative" comparison was performed by setting small ($0.3 \times 0.3mm$) regions-of-interest on the same sites in both the histological and IVUS images (Lower) [64].

	Histological diagnosis								
	CL	*DF*	*FI*	*LP*	*DC*	*FI*	*FF*	*NC*	*Total*
IB-IVUS diagnosis									
CL	*14*	*0*	*0*	*0*					*14*
DF	*2*	*3*	*0*	*0*					*5*
FI	*3*	*0*	*53*	*2*					*58*
LP	*2*	*0*	*8*	*54*					*64*
Total	*21*	*3*	*61*	*56*					*141*
Cohen's κ=0.81 (95%CI: 0.72–0.89)									
IVUS-VH diagnosis									
DC					*20*	*4*	*0*	*2*	*26*
FI					*1*	*25*	*11*	*16*	*53*
FF					*0*	*3*	*13*	*5*	*21*
NC					*0*	*28*	*1*	*12*	*41*
Total					*21*	*60*	*25*	*35*	*141*
Cohen's κ=0.30 (95%CI: 0.14–0.41)									

CL, calcification; DF, dense FI; LP, lipid pool; DC, dense CL; FF, fibro-fatty; NC, necrotic core. Other abbreviations see in Table 1.

Table 4.6.: Direct Qualitative Comparison of the IVUS and Histological Diagnoses.

4.1.3. IVUS Image-Based Plaque Characterization Methods

Image processing methods hold the potential to provide objective and quantitative measures of plaque composition. Previous studies have identified texture analysis as being useful in the analysis of ultrasound images. Hence, almost all image-based plaque characterization methods are based on texture analysis. In 1998, Zhang et al.[103] proposed a method to classify plaque regions into three classes: soft plaque, hard plaque and hard plaque shadow. In their proposed method, detected plaque regions were straightened along the plaque border to form a rectangle B for convenient further processing (figure 4.13). The height of the resulted rectangle is determined as:

$$H = t_{max} + h \tag{4.4}$$

where t_{max} is the maximum thickness of the plaque region and is h the height of a analysis box called elementary region (figure 4.13). Then for each column of B a pixel of interest (POI) is adopted for texture analysis:

$$y_{POI} = arg_{max_{0<j<t(x)}} M(x,j) \tag{4.5}$$

$$M(x,y) = \frac{1}{w} \sum_{i=-w/2}^{w/2} I(x+i,y) \tag{4.6}$$

where I is the intensity of the pixel and $t(x)$ is the thickness of the plaque at column. Based on these pixels,the following texture measures were computed. Zhang et al. adopted texture descriptors since they believed these features have proved useful in a variety of medical and non-medical applications in the past.

Selected texture descriptors are as follows:

1. **Gray-Level-Based Texture Descriptors:** These included standard features of histogram contrast, skewness, kurtosis, dispersion, and variance. In addition, a property describing the radial profile was designed to reflect the different gray-level profile characteristics of the hard and soft plaque. For an elementary region with the POI, the radial profile is determined as:

$$radial - profile = \frac{maxM(x,j)_{0<j<x(t)}}{maxM(x,y+j)_{j=10,20,\ldots,h}} \tag{4.7}$$

2. **Co-Occurrence Matrices:** These matrices describe repeated occurrences of some gray-level configurations in the plaque texture classes. An occurrence of some gray-level configuration may be described by a matrix of relative frequencies $F_{\phi,d}(a,b)$, describing how frequently two pixels with the gray-levels a, b appear in the texture separated by a distance d in direction ϕ. The features energy, entropy, maximum probability, contrast, and inverse difference moment were computed from the resulted co-occurrence matrix (later in section 5.1.1, we talk about these features in detail).

3. **Run-Length Measures:** These measures describe the maximum contiguous set of constant gray-level pixels located at a specified direction. A large number of neighboring pixels of the same gray-level represent a coarse texture while a small number

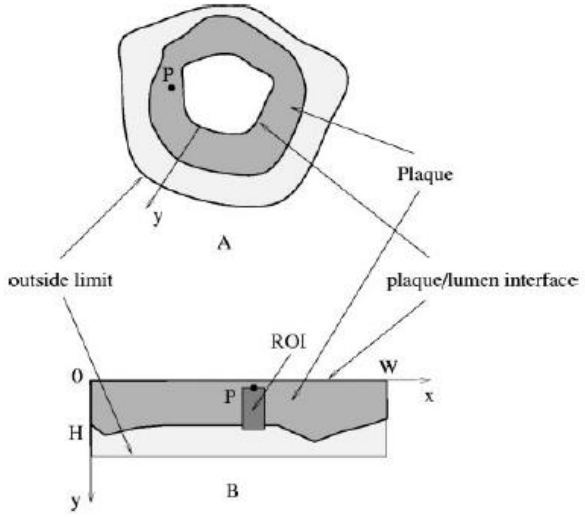

Figure 4.13.: Plaque region straightened along the plaque border. Original plaque region A, straightened plaque region B, point of interest P and its elementary region (bottom, enlarged).

of these pixels represent a fine texture. Hence, the lengths of texture primitives at different directions can serve as texture descriptors. Short primitives' emphasis and long primitives' emphasis were computed as run-length descriptors (later in section 5.1.1, we talk about these features in detail).

4. **Fractal-Based Measures:** These measures (e.g. Brownian fractal dimension) were calculated through the transformation of image space to fractal dimension. From the large number of calculated features, correlated ones were removed. Then, features with the highest discrimination power were identified using the inter-class distance search criterion and the Euclidean metric. Finally, the following three descriptors were identified as providing the best features for soft/hard plaque classification in IVUS images: radial profile, long run emphasis, and the Brownian fractal dimension.

This group obtained IVUS images from coronary arteries *in-vivo* and *in vitro*, using 2.9 French intra-coronary ultrasound imaging catheters (Boston Scientific, San Jose, CA). IVUS images were recorded on S-VHS video tapes and digitized using a high-end commercially available digitizer (Parallax Xvideo 700) at image resolution of 640×480 pixels, 0.03*mm/pixel* and digitization rate of 30*frames/s*. Then, single-frame images were stored as JFIF format and later converted to 8-bit gray-level raw data format. Zhang et al. compared the plaque regions classified by their method to those defined by experts (figure 4.14). Plaque composition in the 12 images was determined with classification correctness of 89.9% overall. Hard plaque was correctly classified in 89.2% of elementary regions (653/732) and soft plaque classification correctness was 90.2% (1805/2001).

They also evaluated their method with the metric percent circumference of hard plaque:

Figure 4.14.: Automated plaque characterization. (a) Original image. (b) Computer-detected soft (black), hard (gray) plaque, and shadow (white) regions, plaque borders were determined automatically. (c) Observer-identified soft, hard, and shadow plaque regions.

$$percent\ \ of\ \ circumference\ \ of\ \ hard\ \ plaque = \frac{circumference\ \ of\ \ hard\ \ plaque}{circumference\ \ of\ \ plaque} \quad (4.8)$$

where circumference was expressed in degrees. A good correlation was found between the computer-detected and observer-defined percent circumference of hard plaque (figure 4.15).

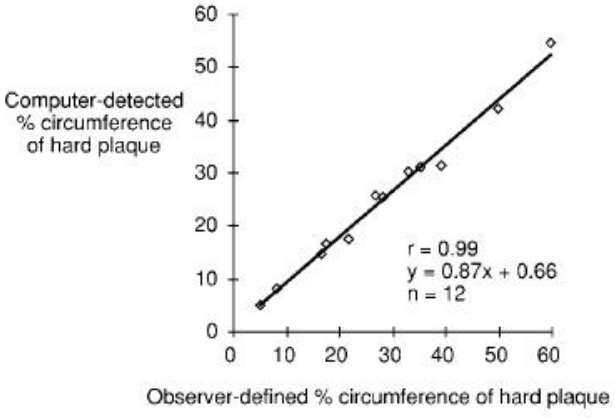

Figure 4.15.: Comparison of computer-detected and observer-defined percent circumference of hard plaque.

Zhang et al. noted the limitations of their work as follows:

1. With the currently available IVUS images detection of the total amount of vessel calcification or hard plaque volume has its limitations. Total calcium burden often cannot be estimated, because deeper structures that may or may not be calcified

are hidden in the shadow of more superficially calcified regions. At the same time, brightness of the initial bright echo does not indicate the total depth or amount of calcification. Therefore, quantification of calcification by intravascular ultrasound can be expressed only as the arc length.

2. Gain setting of the IVUS device is another difficulty associated with ultrasound tissue imaging. Also, image brightness may vary in fibrotic plaques due to angle dependency of echo responses with respect to ultrasound beam. These may affect texture features.

3. This method for plaque characterization is limited to classification of soft and hard plaques. Developing ultrasonic methods for more detailed plaque characterization are vital for better understanding plaque composition.

In 2000, Vince et al. [90] attempted to classify plaque regions into finer classes: calcified, fibrous and necrotic core. They used texture features in their method with the aim of assessing of the efficacy of texture analysis methods in identifying plaque components. To this end, the following statistical texture techniques were evaluated:

1. **First-order statistics method:** The first step in texture analysis was to examine the first-order or low-level statistics describing the image gray-level distribution (histogram). By direct use of the image pixel gray-level values, four first-order statistics were evaluated: mean, variance, skew, and kurtosis.

2. **Haralick's method:** Haralick's method is a second-order statistical approach in which textural features are derived from angular nearest-neighbor spatial-dependence matrices, also known as co-occurrence matrices. Vince et al. computed 14 statistical features from the co-occurrence matrix (also utilized by Zhang et al.). They believed that each feature measured a particular characteristic of the spatial distribution relationship between neighboring pixels in the region of interest. For example, angular second moment measures the homogeneity of the region, whereas contrast measures the amount of local variation present in the region.

3. **Laws' texture energy method:** Laws' method for rapid texture identification was implemented using three main steps. (1) Five coefficient vectors representing levels ($L = [14641]$), edge ($e = [-1-2021]$), shape ($S = [-1020-1]$), wave ($W = [-10201]$), and ripple ($R = [1 - 46 - 41]$) were multiplied to form a set of 5×5 kernels used as filters. Input images were convolved with these kernels, forming a set of filtered images. By combining particular kernels it was possible to extract specific information about the image. (2) Each filtered image was processed with an averaging filter to determine the total textural energy in each pixel's neighborhood. A 3×3 window was used because the selected regions of interest were small. The images generated from this step were termed "energy images." Each set of images formed from orthogonal matrices (for example, EL and LE) were then averaged to provide rotational invariance. (3) The final step was to calculate the mean, variance, and range of values from the regions of interest in the energy images.

4. **Neighborhood gray-tone difference matrix method:** The NGTDM method is an approach that utilizes textural features that correspond to the visual properties of an

image. An NGTDM is a column matrix formed by summing the absolute value of the pixel being observed minus the average of the pixels in its neighborhood. The neighborhood was predefined as a distance of d = 1 pixel because of the small regions of interest.

5. **Texture spectrum method:** In the texture spectrum approach, an image is considered as a set of texture units (TUs) that characterizes the local texture information of a given pixel and its neighborhood. The global texture of the image was characterized by the texture spectrum, which was the frequency distribution of all the TUs in the image. A given 3×3 neighborhood was described by a set of nine elements, V, where the first vector element was the center pixel and the following elements were the succeeding pixels' eight neighbors in a pre-specified order. The corresponding TU was a set of eight elements derived through the formulas in figure 4.16. Each element of the TU had three possible values (0, 1, and 2). When considering all eight elements, this step resulted in 38 or 6561 possible TUs. The TU number, defined as a number between 0 and 6561, was then calculated for each 3×3 region in the image. Finally, the texture spectrum was derived by examining the frequency distribution of all the TUs. The texture spectrum abscissa represents the TU number, and the ordinate represents its occurrence frequency. For this study, three texture features were derived from the texture spectrum and used for classification: black-white symmetry (BWS), geometric symmetry (GS), and degree of direction (DD).

$$
\begin{aligned}
V &= \{V_0, V_1, ..., V_8\} \\
E_i = 0 \quad & if \quad V_i < V_0 \\
E_i = 1 \quad & if \quad V_i = V_0 \\
E_i = 2 \quad & if \quad V_i > V_0 \\
TU &= \{E_1, E_2, ..., E_8\}
\end{aligned}
$$

Figure 4.16.: The nine elements describing a 3×3 neighborhood of pixels (V), the elements of the texture unit (E_i), and the quantitative definition of a texture unit (TU) [90].

IVUS images for this study were acquired by a Boston Scientific catheter (30MHz, 3.5F) and results were evaluated with histology images. Table 4.7 shows the results of classification using each of the five methods explained above. It is seen that the most accurate results are achievable with the Haralick's method. Vince et al. also took into account the computational expense of each method. They believed that First-order statistics, NGTDM, and the texture spectrum approach were very efficient due to the simplicity of the underlying algorithms. The computational expense in Haralick's method was minimized by quantizing the images to 64 gray-levels and optimizing the discrimination by using only two of the 14 features. They believed that Laws' texture energy approach was very inefficient, due to the number of stages necessary in processing the images.

Although, Vince et al. achieved good results with their image-based method, they believed that analysis of IVUS RF has three major advantages over the approach taken in this work which involves digitizing video tape: (1) It is fast, as data can be streamed from

Table 4.7.: Self-validation error rates of texture analysis techniques [90].

Technique	Resubstitution error (%)	Croos-Validation error (%)
First order statistics	29.05	40.48
Haralick's method	0.00	14.76
Law's texture energies	8.10	37.14
NGTDM	18.10	30.95
Texture spectrum	34.76	34.76

the RF port directly to a PC; (2) it does not reduce the resolution of the image; and (3) it cannot be altered by the console display controls. However, they also believed that the capture, rendering, and analysis of IVUS RF data is technically demand fast, sophisticated, and requires expensive hardware while their method can be implemented using standard computer workstations.

Recently, Katouzian et al. [37] developed a texture-based algorithm for plaque characterization using discrete wavelet packet frame (DWPF) and a 2-D envelope detection method. They believed that the extracted textural features by their method are perfectly suited for classification and capture characteristics of the plaque with the highest correlation to histology and their method would also resolve one of the main current limitations of IVUS, which is the discrimination between fibrotic and lipidic tissues. Katouzian et al. also believed that the traditional extracted spectral features from IVUS RF signals are affected by transducer's spectral parameters (bandwidth, center frequency) and their variability make the classification challenging.

IVUS images for their research were acquired by a $40MHz$ Atlantis Boston Scientific (Fremont, CA) IVUS catheter. Primary images contain 256 radial lines that span 360 degree with 2048 samples per line and in order to have an optimized frame size in respect to the computational complexity and the textural resolution, they were interpolated (spline) and decimated in the lateral and axial directions by factor of 2 and 4, respectively.

In their method, images were transferred to a polar plane to form 512×512 frames. Then horizontal and vertical lines of each frame are decomposed with DWPF separately. In DWPF decomposition, a high-pass filter and a low-pass filter are applied to the signal and decomposition continues on the signals resulted form filtering (figure 4.18). The decompositions are translation invariant in DWPF and no decimation occurs between levels. The high-pass and low-pass filters at level can be written as follows:

$$G_l(w) = G_0(2^l w), H_l(w) = H_0(2^l w) \tag{4.9}$$

In their method, the filters were Lemarie-Battle and number of levels were adopted 2. For each component at the last level (level 2), horizontally processed images were multiplied by vertically processed images and the envelope of each pixel was calculated by a 2-D envelope detection method. These envelopes constructed the feature matrix as follows:

$$e^{\rightarrow}_{k,i,j} = \{e^l_{k,i,j} | 0 \leq k \leq (2^{l-1}), i, j = 1, ..., 512\} \tag{4.10}$$

where $e^{\rightarrow}_{k,i,j}$ represents the envelope value of pixel for the components at level. Based on these features, pixels were clustered into four clusters: calcified, fibrotic, lipidic and

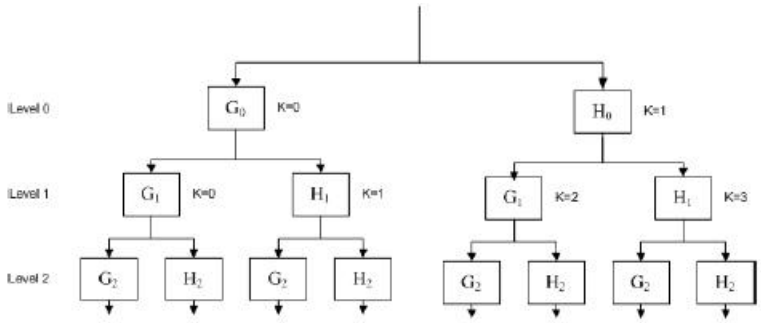

Figure 4.17.: Tree structure for discrete wavelet packet frames (DWPF) and associate indexes [37].

background using k-mean clustering algorithm and then mapped onto a Cartesian plane to generate prognosis histology (PH) images (figure 4.18). PH images were compared to Histology images and the accuracy of classified tissues was found to be 81.71%, 82.76% and 85.51% for fibrotic, lipidic and calcified components, respectively (table 4.8).

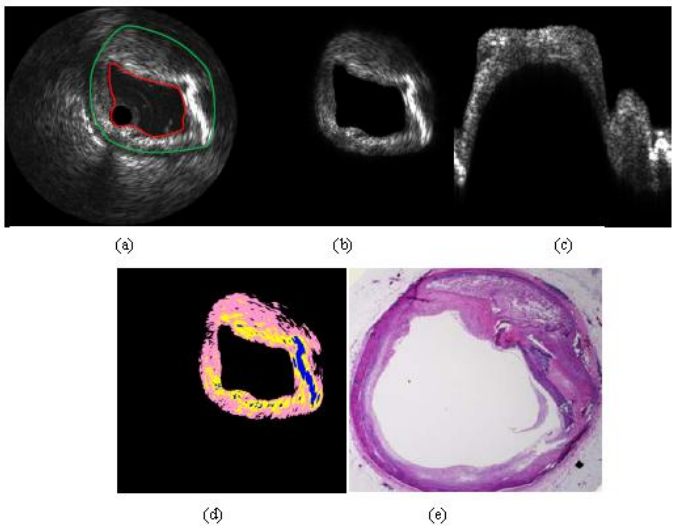

Figure 4.18.: (a): IVUS image with a manually traced vessel wall (green) and lumen (red) borders, (b): segmented plaque in Cartesian coordinates, (c): segmented plaque in r-θ coordinates, (d): generated PH image (pink, yellow and blue represent lipidic, fibrotic and calcified components, respectively) and (e) Movat Pentachrome histology image [37].

The main advantage of the proposed algorithm is that it can reliably classify tissues regardless of the transducer center frequency or spectrum. However, it is not able to detect the necrotic core components directly. Both necrotic core tissues and lipid-rich pools have been recognized as markers for detection of vulnerable plaques and it is an advantage to have a classification algorithm that is able to detect the necrotic core in addition to fibrotic, lipidic and calcified tissues. Furthermore, the effects of blood on generated PH images and classification performance were not investigated in their method. In their future work, Katouzian et al. hope to test the feasibility of tissue classification within the regions of

Table 4.8.: Accuracy of the classified tissues by Katouzian et al. method

Tissue Type	Fibrotic	Lipidic	Calcified
Accuracy	81.71%	82.76%	85.51%

acoustic shadowing behind calcification.

4.1.4. Mixture of IVUS Image Features and IVUS RF Features

As each image-based and RF signal-based approaches have their own advantages and disadvantages, some researchers tried to mix the features extracted from IVUS image and RF signals to better characterize different types of tissues.

In 2008, Escalera et al. [21] proposed a method to characterize different tissues in IVUS images into calcified tissue (characterized by a very high echo-reflectivity and absorption of the ultrasound signal), fibrous plaque (medium echo-reflectivity and good transmission coefficient), and lipidic or soft plaque (characterized with very low reflectance of the ultrasound signal) based on radial frequency, texture-based, and combined features. In order to deal with the classification of overlapping multiple tissues, error-correcting output codes (ECOC) were applied to the feature vectors under the supervision of their proposed strategy.

The parameters of the ARMA model applied to RF signals are the signal-based features in their method and the co-occurrence matrix (defined as the estimation of the joint probability density function of gray-level pairs in an image), local binary patterns (LBP) (used to detect uniform texture patterns in circular neighborhoods with any quantization of angular space and spatial resolution) and Gabor coefficients (resulted from Gabor decomposition of IVUS images) are the image-based features. At the classification stage, three different base classifiers are applied over ECOC configuration: nearest mean classifier (NMC) with the classification decision using the Euclidean distance between the mean of the classes, discrete AdaBoost with 40 iterations of decision stumps, and linear discriminant analysis.

The data set was the RF signals and their reconstructed images from a set of 10 different patients with left descent artery pullbacks acquired in hospital "German Trias i Pujol" from Barcelona, Spain. All these pullbacks contain the three classes of plaque. For each one, 10 to 15 different vessel sections were selected to be analyzed. Two physicians independently segmented 50 areas of interest per pullback. From these segmentations 15 regions of interest (ROI) of tissue per study was selected randomly to make a total of 5,000 evaluation data. In order to reduce the variability among different observers, the regions where both cardiologists agreed have been taken under consideration. Some samples from the data set are shown on the left of figure 4.19. Their results (figure 4.20) showed that combined signal and image-based features with AdaBoost classifier resulted in the best performance ($> 90\%$).

Table 4.9 shows a comparison of different image-based and RF-based methods based on accuracy of detecting different plaques.

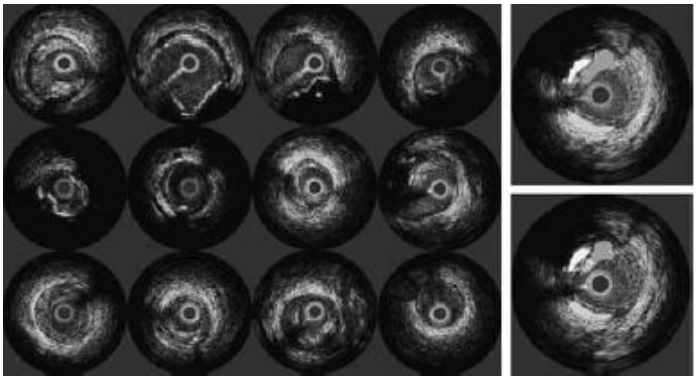

Figure 4.19.: Left: IVUS data set samples. Right: (top) segmentation by a physician and (down) Automatic classification with texture-based features. The white area corresponds to calcium, the light gray area to fibrosis, and the dark gray area to soft plaque [21].

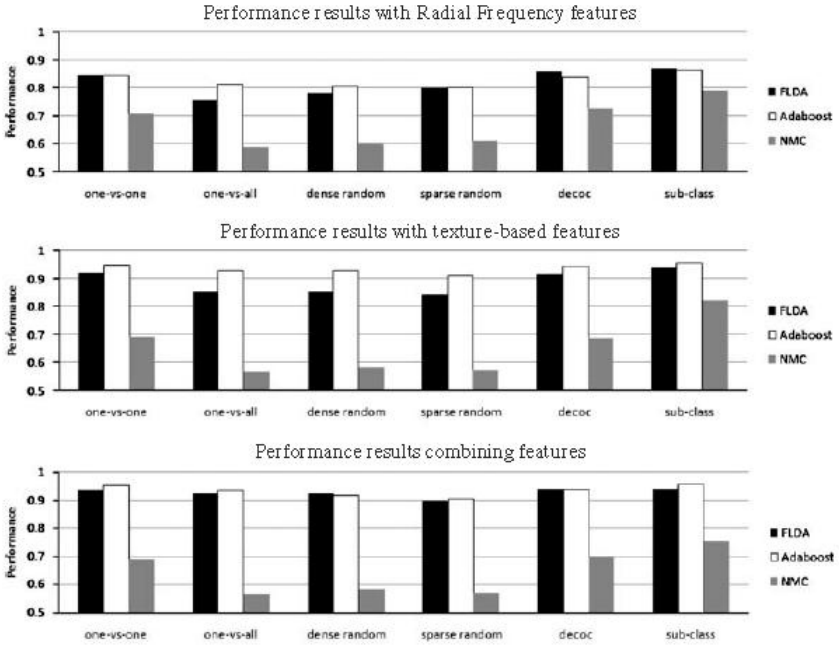

Figure 4.20.: Performance results for different sets of features, ECOC designs and base classifiers on the IVUS data set [21].

Table 4.9.: Comparison of different image-based and RF-based methods.

Group Name	Methodology	Kinds of Plaque Detected and Corresponding Accuracy			
Zhang et al. [103]	Image-based	Hard Palque	Soft Plaque		
		89.2%	90.2%		
Vince et al. [90]	Image-based	Calcified	Fibrous	Necrotic Core	
		Total Accuracy : 82.24%			
Katouzian et al. [37]	Image-based	Calcified	Fibrotic	Lipidic	
		85.51%	81.71%	82.76%	
Nair et al. [58]	RF-based	Calcified	Fibrous	Fibrolipidic	Calcified Necrotic
		92.8%	79.7%	81.2%	85.5%
Murashige et al. [54]	RF-based	Lipid-Laden			
		82.76%			
Kawasaki et al. [63]	RF-based	Calcification	Fibrosis	Lipid Pool	
		97%	94%	91%	

5. Chapter Five: New Approaches For Plaque Component Analysis

The aim of this part of the project is to classify pixels from plaque area of IVUS images into three tissue classes: dense calcium (DC), fibro-fatty(FF) and necrotic core (NC). These plaque components appear with different texture patterns in IVUS images (figure 5.1).

Figure 5.1.: Different tissue types in plaque area of IVUS images: (a) Dense Calcium, (b) Necrotic Core and (c) Fibro-Lipid.

Thereby, texture analysis methods are best suited to characterize coronary plaque compositions. In most texture analysis methods, for each pixel (i, j) of the image $I_{D\times D}$(or I), a$(M+1)\times(N+1)$ neighborhood $I\{i+m, j+n\}$ with $m \in \{-\frac{M}{2}, \frac{M}{2}\}$ and $n \in \{-\frac{N}{2}, \frac{N}{2}\}$ calling sweeping window is being processed. Then, textural features are extracted from this sweeping window and assigned to the central pixel. Finally, according to the extracted features, pixels are classified into predetermined classes by the means of a classifier. It is worth mentioning that since IVUS images are circular cross section of the blood vessel, input images are converted into polar coordinates before applying texture analysis methods so that rectangular sweeping windows used for feature extraction are utilizable (figure 5.2).

Figure 5.3 shows the outline of the project and the steps of Tissue Characterization stage. However, each of the proposed algorithms later explained in this chapter may follow some or all of these steps. It is worth defining the materials of these steps before stating the proposed algorithms.

Note: In this chapter, the plaque area taken directly from the VH examples, in order for us to be able to validate the classifcation algorithms proposed here.

5.1. Materials and General Background

5.1.1. Feature Extraction Methods

Co-occurrence Matrix and Statistical Properties: A co-occurrence matrix C, is used to describe the patterns of neighboring pixels in an image at a given distance d, and a given direction $\theta \in \{0^o, 45^o, 90^o, 135^o\}$ corresponding to horizontal, diagonal, vertical and anti-diagonal directions (figure 5.4). This matrix is somehow a second order histogram of the

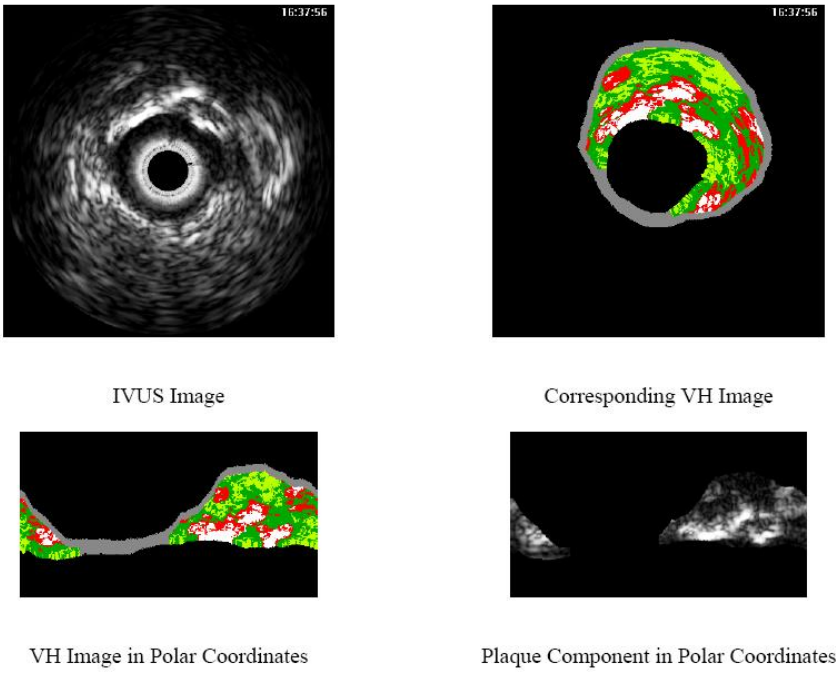

Figure 5.2.: Cartesian-Polar conversion of IVUS images for feature extraction.

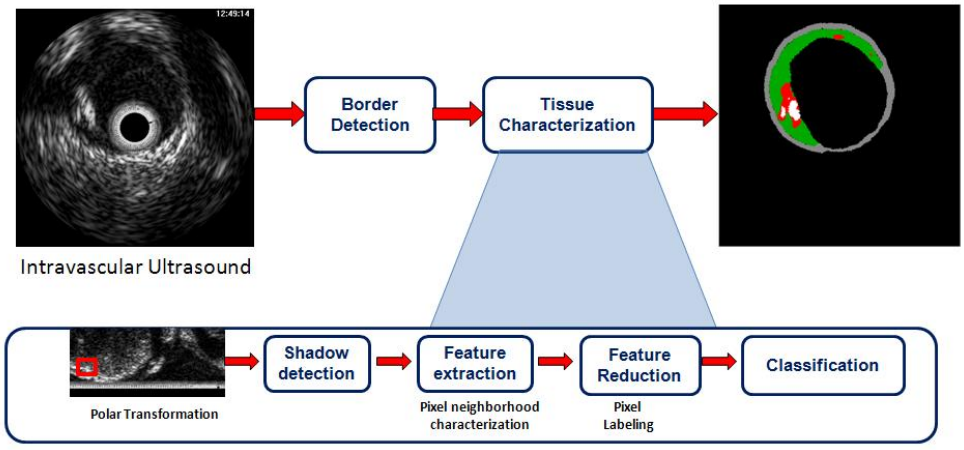

Figure 5.3.: Outline of the project and steps of Tissue Characterization stage.

image and gives information about the relative positions of the various gray-levels within the image [85].

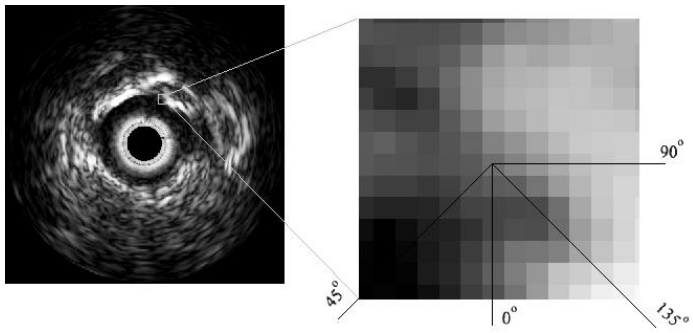

Figure 5.4.: The four directions used to form the co-occurrence matrix.

Let us consider the neighborhood centered on the pixel (i, j) from image I. Its co-occurrence matrix is defined in a certain direction as $C_{d,\theta}(a, b)$, where $a, b \in [1, .., P]$. Heret P refers to maximum gray-level in image I and d ise the gray-levels distance in the direction θ. Figure 5.5 gives a graphical description of this process for $C_{1,0^o}$.

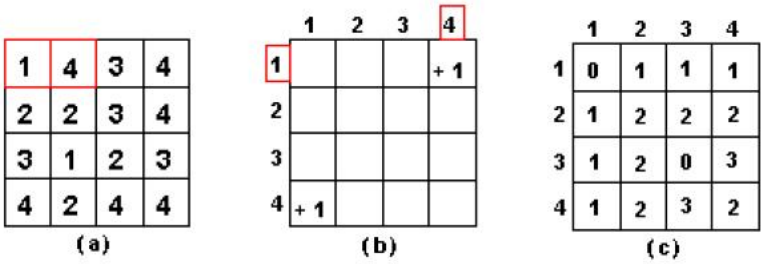

Figure 5.5.: Construction of the co-occurrence matrix in horizontal direction: (a) The original image (b) Horizontal neighboring of gray-levels 1 and 4 with distance 1 occurred once in the image (c) The final result of the horizontal co-occurrence matrix.

Various textural features can then be derived from co-occurrence matrix. For defining these textural features it is necessary to calculate the following statistical parameters in the first step:

$$p^{d,\theta}(a, b) = \frac{C_{d,\theta}(a, b)}{\sum_{a=1}^{P} \sum_{b=1}^{P} C_{d,\theta}(a, b)} \tag{5.1}$$

$$p_x^{d,\theta}(a) = \sum_{b=1}^{P} p^{d,\theta}(a, b) \tag{5.2}$$

$$p_y^{d,\theta}(b) = \sum_{a=1}^{P} p^{d,\theta}(a, b) \tag{5.3}$$

$$p_{x+y}^{d,\theta}(k) = \sum_{a=1}^{P} \sum_{b=1}^{P} p^{d,\theta}(a, b), a + b = k, k = 2, ..., 2P \tag{5.4}$$

$$p_{x-y}^{d,\theta}(k) = \sum_{a=1}^{P}\sum_{b=1}^{P} p^{d,\theta}(a,b), |a-b| = k, k = 1, ..., P-1 \tag{5.5}$$

$$HX^{d,\theta} = -\sum_{a=1}^{P} p_x^{d,\theta}(a) log(p_x^{d,\theta}(a)) \tag{5.6}$$

$$HY^{d,\theta} = -\sum_{b=1}^{P} p_y^{d,\theta}(b) log(p_y^{d,\theta}(b)) \tag{5.7}$$

$$HXY_1^{d,\theta} = -\sum_{a=1}^{P}\sum_{b=1}^{P} p^{d,\theta}(a,b) log(p_x^{d,\theta}(a) p_y^{d,\theta}(b)) \tag{5.8}$$

$$HXY_2^{d,\theta} = -\sum_{a=1}^{P}\sum_{b=1}^{P} p_x^{d,\theta}(a) p_y^{d,\theta}(b) log(p_x^{d,\theta}(a) p_y^{d,\theta}(b)) \tag{5.9}$$

$$Q^{d,\theta}(a,b) = \sum_{k=1}^{P} \frac{p^{d,\theta}(a,k) p^{d,\theta}(b,k)}{p_x^{d,\theta}(a) p_y^{d,\theta}(b)} \tag{5.10}$$

Based on these statistical parameters, the 14 Haralick texture features are defined as follows:

1. Angular Second Moment (ASM): This feature is a measure of smoothness of the image. The less smooth the image is the lower is the ASM.

$$f_1^{d,\theta} = \sum_{a=1}^{P}\sum_{b=1}^{P} p^{d,\theta}(a,b) \tag{5.11}$$

2. Contrast: This feature is a measure of local gray-level variations.

$$f_2^{d,\theta} = \sum_{k=0}^{P-1} k^2 p_{x-y}^{d,\theta}(k) \tag{5.12}$$

3. Correlation:

$$f_3^{d,\theta} = \frac{\sum_{a=1}^{P}\sum_{b=1}^{P} ab p^{d,\theta}(a,b) - \mu_x \mu_y}{\sigma_x \sigma_y} \tag{5.13}$$

4. Variance:

$$f_4^{d,\theta} = \sum_{a=1}^{P}\sum_{b=1}^{P} (a-\mu)^2 p^{d,\theta}(a,b) \tag{5.14}$$

5. Inverse Difference Moment:

$$f_5^{d,\theta} = \sum_{a=1}^{P}\sum_{b=1}^{P} \frac{1}{1+(a-b)^2} p^{d,\theta}(a,b) \tag{5.15}$$

6. Sum Average:

$$f_6^{d,\theta} = \sum_{k=2}^{2P} k p_{x+y}^{d,\theta}(k) \tag{5.16}$$

7. Sum Variance:

$$f_7^{d,\theta} = \sum_{k=2}^{2P} (k - f_6^{d,\theta}) p_{x+y}^{d,\theta}(k) \tag{5.17}$$

8. Sum Entropy:

$$f_8^{d,\theta} = -\sum_{k=2}^{2P} p_{x+y}^{d,\theta}(k) log(p_{x+y}^{d,\theta}(k)) \tag{5.18}$$

9. Difference Variance:

$$f_9^{d,\theta} = variance \;\; of \;\; p_{x-y} \tag{5.19}$$

10. Difference Variance:

$$f_{10}^{d,\theta} = -\sum_{k=1}^{P-1} p_{x-y}^{d,\theta}(k) log(p_{x-y}^{d,\theta}(k)) \tag{5.20}$$

11. Entropy: This feature is a measure of randomness of the image and takes low values for smooth images.

$$f_{11}^{d,\theta} = -\sum_{a=1}^{P}\sum_{b=1}^{P} p^{d,\theta}(a,b) log(p^{d,\theta}(a,b)) \tag{5.21}$$

12. Information Measure:

$$f_{12}^{d,\theta} = \frac{f_{11} - HXY_1^{d,\theta}}{max(HX^{d,\theta}, HY^{d,\theta})} \tag{5.22}$$

$$f_{13}^{d,\theta} = \sqrt{1 - exp^{-2(HXY_2^{d,\theta} - f_{11}^{d,\theta})}} \tag{5.23}$$

13. Maximal Correlation Coefficient:

$$f_{14}^{d,\theta} = \sqrt{second \;\; largest \;\; eigenvalue \;\; of \;\; Q^{d,\theta}} \tag{5.24}$$

Local Binary Pattern: Local Binary Pattern (LBP) is a structure related measure in which a binary number is allocated to the circularly symmetric neighborhoods of the center pixel of the window being processed and the histogram of the resulting binary patterns can be used as a discriminative feature for texture analysis [62], [79]. Actually, in this method N neighbors of the center pixel (i, j) on a circle of radius R with coordinates $(-Rsin\frac{\pi n}{N}, Rcos\frac{\pi n}{N})(n \in \{0, ..., N-1\})$ are processed. Typical neighbor sets (N, R) are (8, 1), (16, 2) and (24, 3), as shown in figure 5.6. As these coordinates do not match the coordinates of the processing window, their corresponding gray-levels are estimated by interpolation. Let g_c corresponds to the gray value of the center pixel and g_n correspond to the gray values of the N neighbor pixels. A binary digit is then allocated to each neighbor based on the following function:

$$s(g_n - g_c) = \begin{cases} 1, & g_n - g_c \geq 0 \\ 0, & g_n - g_c < 0 \end{cases} \tag{5.25}$$

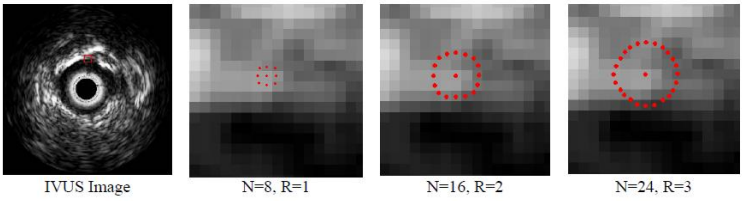

Figure 5.6.: Typical LBP Binary Patterns [20].

Then, by rotating the neighbor set clockwise the least significant resulting binary string is assigned to the processing as its binary pattern $L_{R,N} = \{L^0_{R,N}, ..., L^{N-1}_{R,N}\}$. This way the local binary pattern is rotation-invariant. The basic steps for calculating $L_{R,N}$ and some microstructures that binary patterns can detect in images are illustrated in figure 5.7.

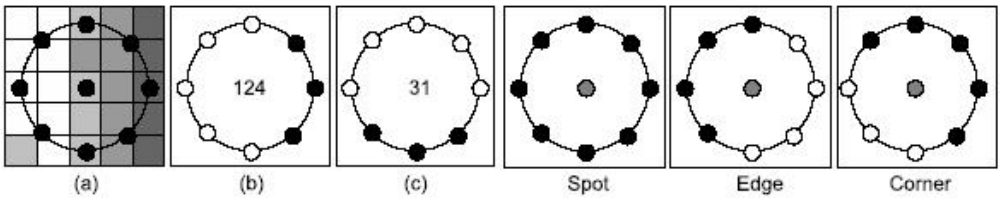

Figure 5.7.: Illustration of LBP, Left: The basic steps in computing the LBP code for a given pixel position: (a) the operator is centered on the given pixel and equidistant samples are taken on the circle of radius around the center; (b) the obtained samples are turned into 0's and 1's by applying a sign function with the center pixel value as threshold; (c) rotation invariance is achieved by bitwise shifting the binary pattern clock-wise until the lowest binary number is found. Right: Some of the microstructures that LBP are measuring [82].

Based on the binary pattern $L_{R,N}$ and the gray values of neighbor pixels g_n, three texture features are defined as follows:

$$f^1_{R,N} = \sum_{n=0}^{N-1} L^n_{R,N} 2^n \tag{5.26}$$

Figure 5.8.: Illustration of $f^1_{R,N}$ feature for $P = 8, R = 1$:Plaque Area in Polar Coordinates (left) and $f^1_{R,N}$ (right)

$$f^2_{R,N} = var\{g_n\} \tag{5.27}$$

Figure 5.9.: Illustration of $f^2_{R,N}$ feature for $P = 8, R = 1$:Plaque Area in Polar Coordinates (left) and $f^2_{R,N}$ (right)

$$f^3_{R,N} = \begin{cases} \sum_{n=0}^{N-1} L^n_{R,N}, & U(L_{R,N}) \leq 0 \\ N+1, & otherwise \end{cases} \tag{5.28}$$

Function U is a transition counter that counts the transition between 0 and 1 and vice versa in the binary pattern.

Figure 5.10.: Illustration of $f^3_{R,N}$ feature for $P = 8, R = 1$:Plaque Area in Polar Coordinates (left) and $f^3_{R,N}$ (right)

Run-length Matrix: One of the methods that has been extensively used in segmentation and texture analysis is Run-length transform [85]. A gray-level run is a set of consecutive pixels having the same gray-level value. The length of the run is the number of pixels in the run. Run-length features encode textural information related to the number of times each gray-level appears in the image by itself, the number of times it appears in pairs,

and so on. Let us consider the neighborhood centered on the pixel (i, j) from image I. Its Run-length matrix is defined in a certain direction as $R_k(a, b)$, where $a \in [1, ..., P]$ where P is maximum gray-level and b is the Run-length, i.e. the number of consecutive pixels along a direction having the same gray-level value. In this approach each neighborhood is characterized with two Run-length matrices:$R_v(a, b)$ and $R_h(a, b)$ corresponding to vertical and horizontal directions, respectively. Figure 5.11 shows the formation of Run-length matrix.

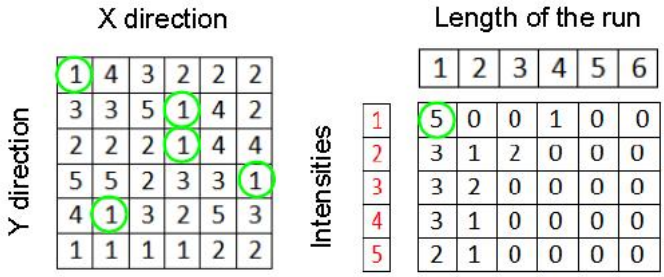

Figure 5.11.: Run-length matrix (in horizontal direction) formation: (a) original intensity matrix and (b) Run-length matrix

Let R be the maximum Run-length , N_r be the total number of runs and N_p be the number of pixels in the processing window. Run-length features are then defined as follows:

- Galloway (Traditional) Run-length Features: The five original features of Run-length statistics derived by Galloway [26] are as follows:
  1. Short Run Emphasis (SRE):

$$f_1^k = \frac{1}{N_r} \sum_{a=1}^{P} \sum_{b=1}^{R} \frac{R_k(a, b)}{b^2} \tag{5.29}$$

Figure 5.12.: Illustration of feature SRE: Plaque Area in Polar Coordinates (left) and SRE (right).

  2. Long Run Emphasis (LRE):

$$f_2^k = \frac{1}{N_r} \sum_{a=1}^{P} \sum_{b=1}^{R} R_k(a, b).b^2 \tag{5.30}$$

Figure 5.13.: Illustration of feature LRE: Plaque Area in Polar Coordinates (left) and LRE (right).

3. Gray-Level Non-uniformity (GLN):

$$f_3^k = \frac{1}{N_r} \sum_{a=1}^{P} (\sum_{b=1}^{R} R_k(a,b))^2 \tag{5.31}$$

Figure 5.14.: Illustration of feature GLN: Plaque Area in Polar Coordinates (left) and GLN (right).

4. Run-length Non-uniformity (RLN):

$$f_4^k = \frac{1}{N_r} \sum_{b=1}^{R} (\sum_{a=1}^{P} R_k(a,b))^2 \tag{5.32}$$

Figure 5.15.: Illustration of feature RLN: Plaque Area in Polar Coordinates (left) and RLN (right).

5. Run Percentage:

$$f_5^k = \frac{N_r}{N_p} \tag{5.33}$$

- Chu Run-length Features: The following features proposed by Chu et al. extract gray-level information in Run-length matrix:
  1. Low Gray-Level Run Emphasis (LGRE):

Figure 5.16.: Illustration of feature Run Percentage: Plaque Area in Polar Coordinates (left) and Run Percentage (right).

$$f_6^k = \frac{1}{N_r} \sum_{a=1}^{P} \sum_{b=1}^{R} \frac{R_k(a,b)}{a^2} \tag{5.34}$$

Figure 5.17.: Illustration of feature LGRE: Plaque Area in Polar Coordinates (left) and LGRE (right).

2. High Gray-Level Run Emphasis (HGRE):

$$f_7^k = \frac{1}{N_r} \sum_{a=1}^{P} \sum_{b=1}^{R} R_k(a,b).a^2 \tag{5.35}$$

Figure 5.18.: Illustration of feature HGRE: Plaque Area in Polar Coordinates (left) and HGRE (right).

- Dasarathy and Holder Features: These features follow the idea of joint statistical measure of gray-level and run length:

1. Short Run Low Gray-Level Emphasis (SRLGE):

$$f_8^k = \frac{1}{N_r} \sum_{a=1}^{P} \sum_{b=1}^{R} \frac{R_k(a,b)}{a^2.b^2} \tag{5.36}$$

Figure 5.19.: Illustration of feature SRLGE: Plaque Area in Polar Coordinates (left) and SRLGE (right).

2. Short Run High Gray-Level Emphasis (SRHGE):

$$f_9^k = \frac{1}{N_r} \sum_{a=1}^{P} \sum_{b=1}^{R} \frac{R_k(a,b).a^2}{b^2} \tag{5.37}$$

Figure 5.20.: Illustration of feature SRHGE: Plaque Area in Polar Coordinates (left) and SRHGE (right).

3. Long Run Low Gray-Level Emphasis (LRLGE):

$$f_{10}^k = \frac{1}{N_r} \sum_{a=1}^{P} \sum_{b=1}^{R} \frac{R_k(a,b).b^2}{a^2} \tag{5.38}$$

Figure 5.21.: Illustration of feature LRLGE: Plaque Area in Polar Coordinates (left) and LRLGE (right).

4. Long Run High Gray-Level Emphasis (LRHGE):

$$f_{11}^k = \frac{1}{N_r} \sum_{a=1}^{P} \sum_{b=1}^{R} R_k(a,b).a^2.b^2 \tag{5.39}$$

Above mentioned methods have been previously used by several groups for IVUS plaque characterization. In next sections the proposed methods are introduced and discussed.

Figure 5.22.: Illustration of feature LRLGE: Plaque Area in Polar Coordinates (left) and LRHGE (right).

5.1.2. Feature Reduction

Linear Discriminant Analysis (LDA): Linear Discriminant Analysis(LDA) are methods which are used in statistics and machine learning to find the linear combination of features which best separate two or more classes of objects or events. The resulting combination may be used as a linear classifier or more commonly, for dimensionality reduction before later classification.

Suppose that the feature vectors come from C different classes (each class with mean μ_i and covariance Cov_i), then the between class and within class scatter matrices are defined as follows:

$$S_b = \frac{1}{C}\sum_{i=1}^{C}(\mu_i - \mu)(\mu_i - \mu)^T \quad , \quad \mu = \frac{1}{C}\sum_{i=1}^{C}\mu_i \tag{5.40}$$

$$S_w = \sum_{i=1}^{C} Cov_i \tag{5.41}$$

It is proved that eigenvectors of $S_w^{-1}S_b$ are the directions that best separate these classes from each other [95]. Projecting feature vectors to the L (L $<$ # of features) largest eigenvectors results in a new reduced feature vector that better suited to classification methods. Figure 5.23 shows a Fisher direction for a three class problem.

5.1.3. Classification

SVM Classifier

Support Vector Machines (SVM) are the classifiers based on the concept of decision planes that define decision boundaries. A decision plane is one that separates between a set of objects having different class memberships. A schematic example is shown in the illustration below. In this example, the objects belong either to class Black or White. The separating line defines a boundary on the right side of which all objects are Black and to the left of which all objects are White.

The above is a classic example of a linear classifier, i.e., a classifier that separates a set of objects into their respective groups (Black and White in this case) with a line. Most classification tasks, however, are not that simple, and often more complex structures are needed in order to make an optimal separation, i.e., correctly classify new objects (test cases) on the basis of the examples that are available (train cases). Classification tasks based on drawing separating lines to distinguish between objects of different class memberships are known

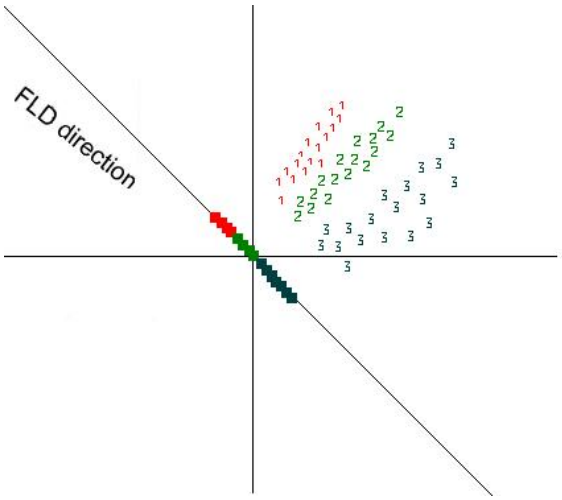

Figure 5.23.: Distribution of three classes and the Fisher direction that best separates these classes from each other.

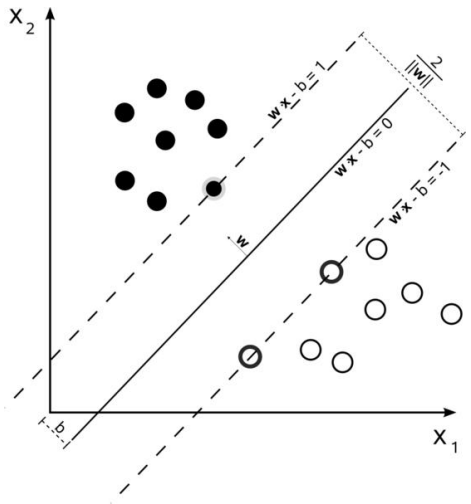

Figure 5.24.: Maximum-margin hyper-plane and margins for a SVM trained with samples from two classes. Samples on the margin are called the support Distribution.

as hyperplane classifiers. Support Vector Machines are particularly suited to handle such tasks.

Support Vector Machine (SVM) is primarily a classifier method that performs classification tasks by constructing hyperplanes in a multidimensional space that separates cases of different class labels. To construct an optimal hyperplane, SVM employs an iterative training algorithm which is used to minimize an error function. According to the form of the error function, SVM models can be classified into different distinct groups. The C-SVM type is used in all proposed algorithms. In a two-class case, if the training dataset consists of feature vectors $\{f_1, ..., f_n\}$ with class labels $y_i \in \{-1, 1\}$, then the SVM training problem is equivalent to finding W and b such that training involves the minimization of the error function [3] and [13]:

$$\frac{W^T W}{2} + C \sum_{i=1}^{N} \zeta_i \tag{5.42}$$

subject to the constraints:

$$y_i(W^T \varphi(x_i) + b) \geq 1 - \zeta_i \;\; and \;\; \zeta_i \geq 0, \quad i = 1, ..., N \tag{5.43}$$

where $\zeta_i \geq 0$ are the so-called slack variables that allow for misclassification of noisy data points, and parameter $C > 0$ controls the trade-off between the slack variable penalty and the margin [3]. In fact, W and b are chosen in a way that maximize the margin, or distance between the parallel hyper-planes that are as far apart as possible while still separating the data (figure 5.24).

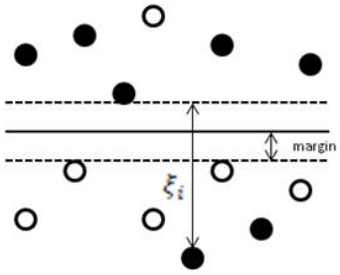

Figure 5.25.: Example of misclassification that shows slack variables.

The function $\varphi(x)$ maps the data to a higher dimensional space. This new space is defined by its kernel function:

$$K(f_i, f_j) = \varphi(f_i)^T \varphi(f_j) \tag{5.44}$$

The above problem can be formulated as a quadratic optimization process. The details of the solution and its implementation can be found in [24]. The Gaussian Radial Basis Function (RBF) kernel was used:

$$K(f_i, f_j) = e^{-\gamma ||f_i - f_j||^2} \tag{5.45}$$

This was firstly due to the fact that RBF kernel has only one parameter (γ) to adjust. Also, SVM classifiers based on RBF kernel was found more accurate than linear, sigmoid, and polynomial kernels in case of our problem.

The publicly available C++ implementation of the SVM algorithms known as LIBSVM [24] was used. The entire dataset was normalized prior to training by setting the maximum value of each feature to 1 and the minimum to 0. For each set of parameters, 5-fold cross-validation was performed: the SVM was trained using 80% of the data samples, classified the remaining 20%, and repeated the procedure for all 5 portions of the data.

5.1.4. Post-Processing

Studying intensity variety of each plaque component in VH images of the dataset through histogram analysis reveals that useful information can be extracted via this simple analysis. Figure 5.26 illustrates the histogram of pixels for three different plaque components. As this gray-scale derived information might be ignored among many textural features in the classification steps, another step is added to the algorithm after the classification by SVM. In this step the given label of a pixel by SVM is confirmed or altered based on some prior information derived from the histogram of the IVUS image.

Some useful information is pointed out below that can be inferred from the histograms displayed in figure 5.26:

- The majority of samples belong to FF class; however, there are few FF pixels whose their intensities exceed the gray-level 150 (ThFF = 150).
- Most of the pixels with intensities above the gray-level 200 (ThDC (low) = 200) belong to the DC class, whereby few pixels with value under 50 (ThDC (high) =50) belong to this class.
- Pixels belonging to the NC are concentrated more between 30 to 200 gray-levels (ThNC (low) =30) and (ThNC (high) = 200).

So, based on these additional thresholds, the system will decide on whether to change the decision of SVM classifier or not.

5.1.5. Dataset

The data was acquired from 10 patients, which included about 2263 gray-scale IVUS images and their corresponding VH images. These IVUS images of size 400×400 pixels were acquired using an electronic probe (In-Vision Gold, Volcano Therapeutics, Inc.) with a synthetic aperture 2.9 F and a frequency of 20 MHz. A motorized pullback was performed along the entire vessel with a speed of 1.0 mm/s using a dedicated pullback device. A total number of 500 frames from 12 vessels (6 left anterior descending (LAD), 3 right coronary artery (RCA), 3 left circumflex (LCX)) of 10 patients were available for VH analysis and comparison with IBH. In the VH analysis the total average amount of fibrous/fibrofatty, dense calcium and necrotic core were (1,505,907 pixels) $37647mm^2$, (388,073 pixels) $9701mm^2$, and (516,711 pixels) $12917mm^2$, respectively. The relative average amounts per cross-section were 63%, 16%, and 21%.

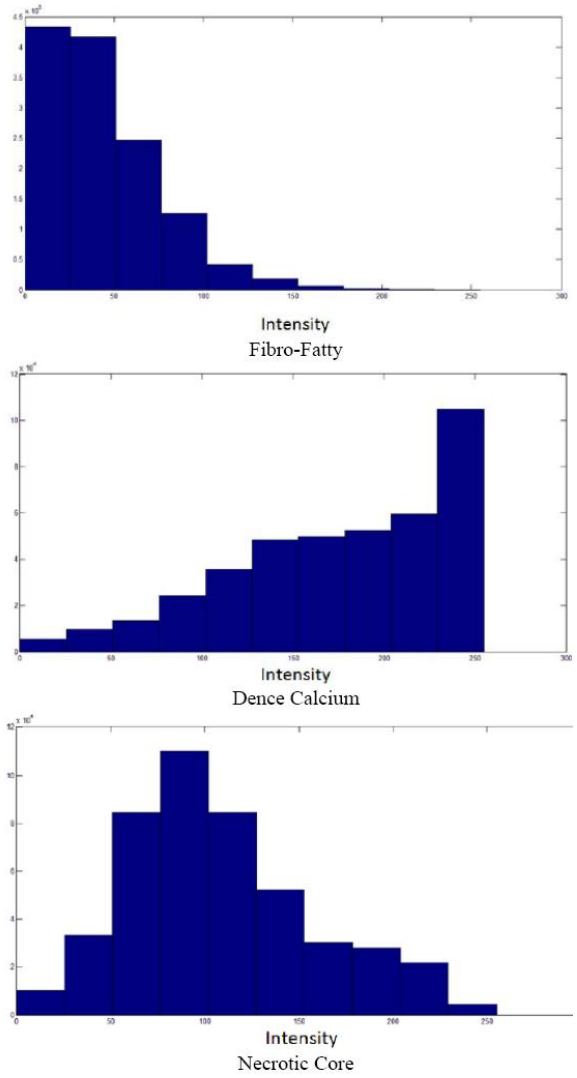

Figure 5.26.: The histogram of pixels belonging to FF, DC, and NC classes for 400 out of 500 IVUS images.

5.1.6. Statistical Analysis

The measures of sensitivity, specificity and predictive accuracy for the three plaque components were calculated and reported as statistical analysis in this thesis. The standard formulae for these measures were the same commonly accepted in medical literature [58].

$$Sensitivity = \frac{True\ Positive\ Decisions}{Decisions\ Actually\ Positive} \tag{5.46}$$

$$Specificity = \frac{True\ Negative\ Decisions}{Decisions\ Actually\ Negative} \tag{5.47}$$

$$Accuracy = \frac{All\ Correct\ Decisions}{Total\ Cases} \tag{5.48}$$

$$CI_{0.95\%} = X \pm 1.96 \times \frac{X \times (1 - X)}{N} \tag{5.49}$$

Where X is either the sensitivity or specificity and N is the number of decisions used in denominator for calculating the sensitivity or specificity.

In addition to the above mentioned measures, Cohen's Kappa index is calculated to quantify the degree of agreement between the Algorithm IV and VH classification for *in-vivo* validation, and Algorithm IV and manual painted images for *ex-vivo* validations. A kappa value of $0.41 - 0.60$ indicates moderate (fair) agreement, $0.61 - 0.80$ indicates good agreement, and $0.81 - 1.0$ indicates excellent agreement. This metric was originally introduced by Cohen to determine the level of agreement between two observers [58]. The kappa is calculated as :

$$k = \frac{\rho_0 - \rho_c}{1 - \rho_c} \tag{5.50}$$

where ρ_0 is the observed proportion of agreement and ρ_c is the expected proportion of agreement resulting from chance.

5.2. Algorithm I

5.2.1. Textural Feature Extraction

As it was mentioned in the previous section, various textural features can be derived from Run-length matrix such as the short run emphasis, the long run emphasis, the Gray-level non-uniformity, the Run-length non-uniformity, and the run percentage. These features have been previously used on IVUS images however the results were not fulfilling [90]. Hence, two new features are proposed characterizing each gray-level a (i.e. every row) of the Run-length matrix. The first feature $f_1^k(a), k \in \{h, v\}$ where *h* and v represent horizental and vertical respectively is defined as the maximum number of occurrences multiplied by the length of the run with maximum occurrence b_m:

$$f_1^k(a) = R_k(a, b_m) \times b_m \quad , \quad b_m = arg_b\ max(R_k(a, b)) \tag{5.51}$$

And the second feature $f_2^k(a)$ is defined as the sum of every occurrences multiplied by its corresponding Run-length:

$$f_2^k(a) = \sum_b b \times R(a,b) \tag{5.52}$$

This way, each pixel (i,j) is mapped to a feature matrix $F_{i,j}$:

$$F_{i,j} = \begin{pmatrix} f_1^h(1) & f_2^h(1) & f_1^v(1) & f_2^v(1) \\ . & . & . & . \\ . & . & . & . \\ . & . & . & . \\ f_1^h(a) & f_2^h(a) & f_1^v(a) & f_2^v(a) \\ . & . & . & . \\ . & . & . & . \\ . & . & . & . \\ f_1^h(P) & f_2^h(P) & f_1^v(P) & f_2^v(P) \end{pmatrix} \tag{5.53}$$

Let us consider now each column $F_{i,j,c}$ of matrix $F_{i,j}$ as a signal that is a function of the grey level *a*. As shown in figure 5.27, these signals reveal different frequency contents. This motivates us to extract discriminative features from spatial-frequency representation of the signals. Therefore, each signal is decomposed into a detail $F_{i,j,c}^d$ and an approximation $F_{i,j,c}^a$ by means of $1D$ discrete wavelet transform (DWT):

$$F_{i,j,c}^a[u] = (F_{i,j} * l)[u] \tag{5.54}$$

$$F_{i,j,c}^d[u] = (F_{i,j} * h)[u] \tag{5.55}$$

Then, each DWT component (($F_{i,j,c}^d[u]$) and ($F_{i,j,c}^a[u]$)) is characterized by a set of statistical features, namely its weighted mean, weighted variance, maximum of signal and its index:

$$\rho_{1,c}^k = \frac{1}{P} \sum_{u=1}^{P} u \times F_{i,j,c}^k(u) \tag{5.56}$$

$$\rho_{2,c}^k = \frac{1}{P} \sum_{u=1}^{P} (u \times F_{i,j,c}^k(u) - \rho_{1,c}^k)^2 \tag{5.57}$$

$$\rho_{3,c}^k = maxF_{i,j,c}^k(u) \tag{5.58}$$

$$\rho_{4,c}^k = arg_u maxF_{i,j,c}^k(u) \tag{5.59}$$

Furthermore, spectral behavior of these components is also characterized by means of autoregressive (AR) model of order 5:

$$F_{i,j,c}^k(u) = \sum_{t=1}^{5} F_{i,j,c}^k(u-t) \times \varphi_{t,c}^k + n(u) \tag{5.60}$$

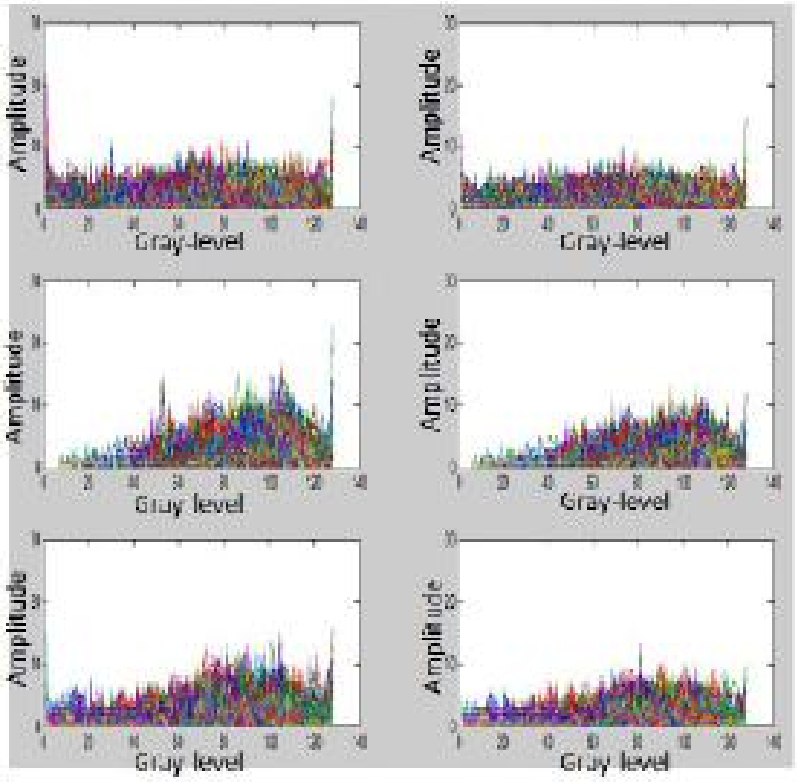

Figure 5.27.: Distribution of 5000 bundle feature vectors for each plaque type. Top to down: DC, fibro-lipid, and NC. Left to right: f_1^h and f_2^h.

where $n(u)$ is the white noise and $\varphi^k_{t,c}$ are the coefficients of the AR model. These coefficients are also used as features.

Finally, the feature vector of each pixel (i, j) is defined as follows:

$$X_{i,j} = \{\rho^k_{l,c}, \varphi^k_{t,c}, l \in \{1, ..., 4\}, t \in \{1, ..., 5\}, c \in \{1, ..., 4\}, k \in \{a, d\}\} \tag{5.61}$$

This vector is the input of the SVM classifier. This classifier was explained in the classification subsection previously.

The block diagram of the proposed algorithm is shown in figure 5.28.

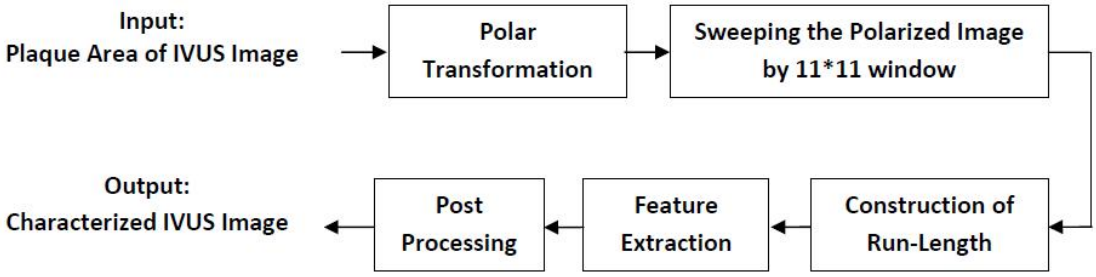

Figure 5.28.: Block diagram of the newly proposed modified Run-length method.

5.2.2. Result and Discussion of Algorithm I

The three feature extraction mentioned methods were then applied on the set of 200 frames. The characterized IVUS images were validated by their corresponding VH images and the accuracy, sensitivity, and specificity parameters were calculated for each technique. The results for this approach were compared to methods using LBP or co-occurrence-based features. The size of the neighborhood was empirically chosen to be 11×11 for all methods. This was done to get the optimum results for every method separately. For LBP method, five circles were then constructed in each neighborhood. Then, three features were extracted from each circle and the number of features for every pixel in LBP method thus sums up to 15. Extracting features from five circles with different radii can be thought of as a multi-resolution textural analysis. Total number of features in the co-occurrence method was 14 which include e.g. homogeneity, contrast, inverse difference moment, and so on. Results using different methods are presented below in table 5.1. According to the results, algorithm I is more capable to classify DC and NC plaques in comparison to LBP or co-occurrence methods.

Although, this approach reveals a higher overall accuracy, the co-occurrence and LBP methods performs better in characterizing the fibro-lipid regions. Figure 5.29 illustrates the images characterized by all methods with their corresponding IVUS and VH images. In this study, the sensitivity of all methods for the detection of NC was low (55%). This fact was caused by similarities between NC and DC in Gray-level IVUS images [30]. Furthermore, previous studies have showen that plaque areas adjacent to DC are frequently coded as NC tissue in VH images [76]. For a typical frame the proposed method took approximately 12 seconds to characterize the pixels, whereas the LBP took 2.6 minutes and

Table 5.1.: The Results of Algorithm I versus Other Techniques

Method	DC		FF		NC		Overall Accuracy
	Sensitivity	Specificity	Sensitivity	Specificity	Sensitivity	Specificity	
LBP	45%	96%	97%	42%	30 %	95%	71%
Co-occurrence	67%	95%	84%	80%	53%	83%	75%
Proposed method	70 %	95 %	84 %	75 %	55 %	82 %	77 %

the co-occurrence took nearly 60 minutes. Thus, in terms of time efficiency, the proposed method further outdoes the other two. A MATLAB implementation on an Intel Core 2 CPU2.00 GHz computer with 2.0 GB Ram was used in this work.

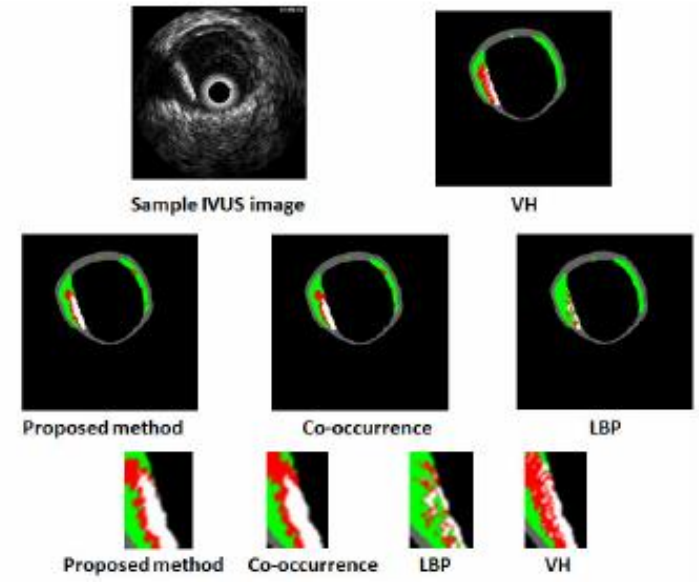

Figure 5.29.: The result of the feature extraction method in comparison with the Co-occurrence and LBP methods from left to right. (White is DC, Green is fibro-lipid, and Red is NC)

5.3. Algorithm II

For proposing this algorithm, this fact was taken into account that since each tissue shows different echogenic characteristics, the different plaque components can be characterized by their local frequency components. The best tool for this purpose is Wavelet Transform (WT). WT provides the best approximation of a space-frequency representation of an image, i.e. it permits to know which spectral components exist at which position in the input image. The main drawback of the WT is that it is translation non-invariant due to the decimation applied to the image after each decomposition level. Recently, another type of wavelet transforms known as Redundant Wavelet Transforms (RWT) has been introduced

[59]. In contrary to the classical WT, there is no decimation step after filtering the input image. This provides the decomposition to be translation invariant and since it preserves the size of images in each level of decomposition, the local spectral components can be retrieved without any interpolation step. To generalize such transform, the Wavelet Packet Transform (WPT) [16] has been introduced to decompose the whole frequency spectrum into multiple sub-bands of varying sizes. It has been shown to provide a more redundant representation for the analysis of complex textural information. By combining the RWT and WPT, image can be decomposed into multiple sub-band images (figure 5.30). This decomposition provides translation invariance in addition to the rotation invariance gained by the initial polar transform.

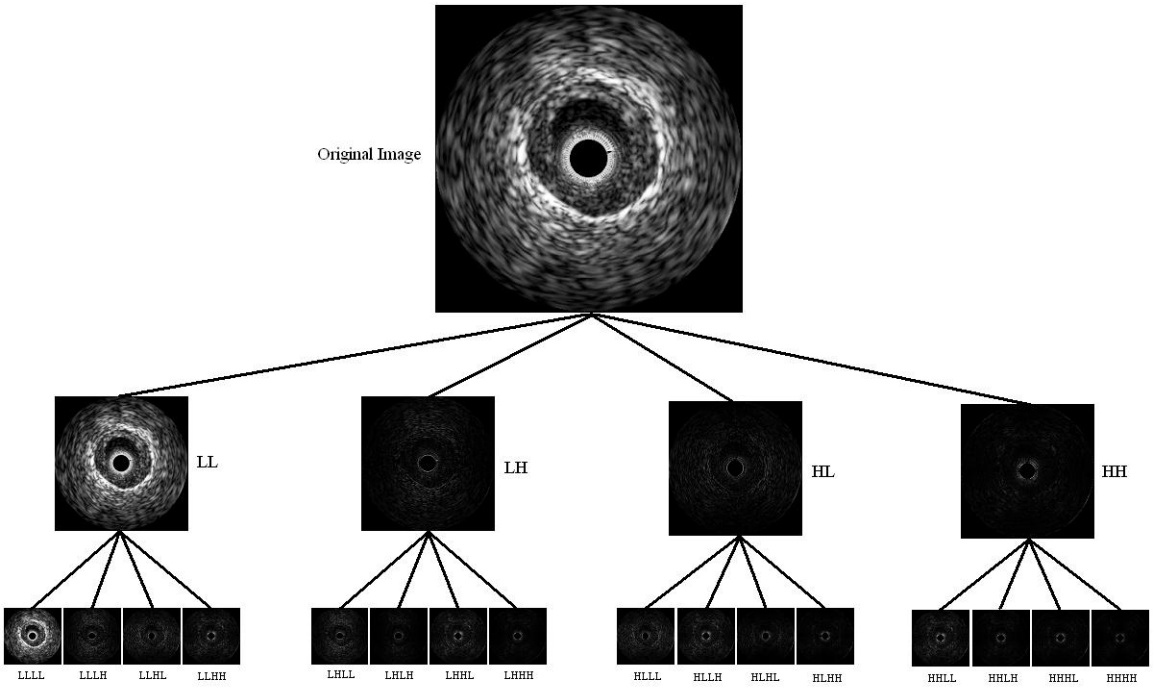

Figure 5.30.: Two level decomposition of RWT+WPT for an IVUS image.

5.3.1. Textural Feature Extraction

Let $\{I_k\}, k \in \{1, N\}$ be a collection of N sub-band images extracted from image *I* through redundant wavelet packet transform (RWPT). This section presents how to characterize each pixel (i, j) from *I* with textural descriptors extracted from the $\{I_k\}$. This provides an enhanced extraction of texture information by analyzing the different sub-band of the frequency spectrum. In this algorithm, the approach which is based on Run-length features is compared to Co-occurrence, and Local Binary pattern (LBP) methods. Each neighborhood is characterized with two Run-length matrices $R_k^x(a, b)$ and $R_k^y(a, b)$ corresponding respectively to *x* and *y* directions in sub-band *k*. The 11 Run-length-based features introduced in section 5.1.1 in equations 5.29-5.39 were used. Let us denote $f_k^{\theta,\lambda}(i, j)$, where $\theta = \{x, y\}$ and $\lambda = \{1, 2, ..., 11\}$. The 22 features extracted from the neighborhood $\{I_k(i+m, j+n)\}_{m,n}$

of each pixel (i, j) of each image I_k is then characterized by the following set of features $V_{i,j}^k$:

$$V_{i,j}^k = \{f_k^{\theta,\lambda}(i,j)\}_{\theta,\lambda} \tag{5.62}$$

As the principal objective in a classification problem is to extract features that are capable of discriminating different classes as much as possible, the best subset of the $\{V^k\}_{k\in\{1,N\}}$ has to be chosen out to provide an optimal discrimination power. To this end, an adapted discriminant measure(Fisher criterion) is introduced:

$$D(k,\theta,\lambda) = \frac{(\mu_p^{k,\theta,\lambda} - \mu_q^{k,\theta,\lambda})^2}{\sigma_p^{k,\theta,\lambda^2} - \sigma_q^{k,\theta,\lambda^2}} \tag{5.63}$$

where $\mu_p^{k,\theta,\lambda}$ and $\sigma_p^{k,\theta,\lambda^2}$ are respectively the mean and the variance of the component $f_k^{\theta,\lambda}$ of V^k in the P^{th} class. This measure takes high values when the feature is varied in classes such that it has maximum differences in the mean and minimum variances. After computing the Fisher criterion for each component of all the $\{V^k\}_{k\in\{1,N\}}$ sub-band which have higher values offer the best discrimination power. A variant of the Local Discriminant Basis (LDB) algorithm was proposed here which was introduced by Saito and Coifman [16] with Fisher's criterion. This algorithm selects the best subset of the $\{V^k\}_{k\in\{1,N\}}$ by computing its discrimination power as follows:

$$D(k) = \sum_{\theta}\sum_{\lambda} D(k,\theta,\lambda) \tag{5.64}$$

Each pixel (i, j) of I is then characterized by the subset of features denoted $\{V_{i,j}^k\}_{k\in\{1,N\}}$ with $M \subset \{1, N\}$.

5.3.2. Weighted Classification Structure based on SVM

For classification purposes, a structure of multi-class support vector machines is used. For each selected sub-band k with $k \in M$, a SVM is associated. However, all sub-bands do not have the same discrimination ability. Therefore, a weight is assigned to each classifier based on its discrimination ability. The final decision for a pixel is attained by considering the weighted votes of all SVMs. The block diagram of the proposed algorithm is shown in figure 5.31.

5.3.3. Result and Discussion of Algorithm II

The study group used for algorithm II is the same as the one used for algorithm I. The characterized IVUS images were validated by their corresponding VH images and the accuracy, sensitivity, and specificity parameters were calculated for each technique. Since the most important plaque components for atherosclerosis staging are lipid-rich tissues, necrotic core and calcifications, the classification was concentrated into these three classes. The Daubechies 4 wavelet, which has the ability of following small variations, is used for the RWPT decomposition. The number of decomposition levels was set to two, giving 21 sub-band images. The size of neighborhoods, on which features were extracted, was empirically chosen to be 9×9 for all methods. For LBP method, four circles were then

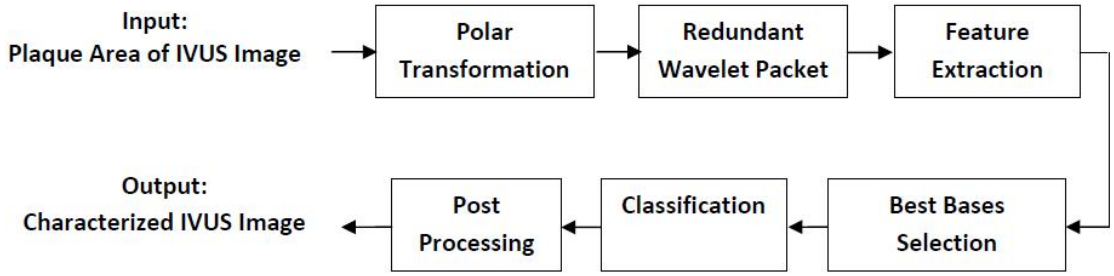

Figure 5.31.: Block Diagram of Algorithm II.

constructed in each neighborhood. Then, three features were extracted from each circle. After computing Fisher criterion for feature vectors of every sub-band images, a subset of 12 were selected based on their discrimination power and LDB procedure. Then, a weight was assigned to each based on their Fisher measure. The computed weights show that sub-band two (low-frequency) has the best discrimination power in comparison with the others. Again, the LIBSVM C++ implementation of the SVM algorithms was used. A grid-search was performed for optimal parameter selection and a 5-fold cross validation to evaluate the performance of all three methods. For a typical frame the Run-length method took approximately 2 minutes to extract the features, whereas the LBP needed 20 minutes and the co-occurrence nearly 120 minutes. In terms of time efficiency, the Run-length method outperforms the other two. A MATLAB implementation on an Intel Core 2 CPU 2.00 GHz computer with 2.0 GB Ram was used in this work. Table 5.2 illustrates the results using different methods besides the influence of the post-processing step. It can be inferred from the results that the Run-length feature extraction method has a better capability for classifying DC plaques, while LBP and co-occurrence for NC. Results also show the influence of the post-processing step on the sensitivity of the NC class. Therefore, one might use the textural features and the classification procedure for dividing the plaque area into two classes, i.e. DC and FF, and then use prior information on their intensity distributions to distinguish the NC regions from them. Still, the sensitivity of all methods for the detection of the NC was low (46%). This fact was caused by similarities between NC and DC in Gray-level IVUS images [76].

Table 5.2.: Accuracy of different techniques: Numbers within parenthesis and without relate respectively to before and after post-processing.

Technique	Overall Accuracy		DC	FF	NC
Run-length	(73%)72 %	Sensitivity(%)	(76)73	(97)85	(9)42
		Specificity(%)	(93)93	(57)79	(96)84
Co-Occurence	(71%)71%	Sensitivity(%)	(72)70	(97)84	(14)46
		Specificity(%)	(96)96	(58)80	(94)82
LBP	(66%)70%	Sensitivity(%)	(40)59	(97)85	(8)47
		Specificity(%)	(95)95	(37)78	(96)80

Also figure 5.32 illustrates the images characterized by all methods with their corresponding IVUS and VH images.

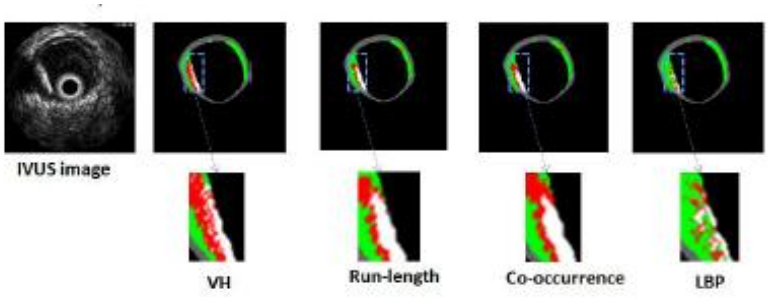

Figure 5.32.: The result of feature extraction methods (White is calcium, Green is fibro-fatty, and Red is Necrotic).

5.4. Algorithm III

In this algorithm some new facts were taken into account that were not noted in the previous algorithms. An important fact, which is mostly ignored in characterizing atherosclerosis plaques via features extracted from IVUS images, is to detect the acoustic shadowing behind Dense Calcified (DC) regions and treat them differently. These shadow regions which exist and displayed in the plaque area of some IVUS images appears as echo-soft; so, when treated within other parts of plaque area although they are mostly Calcium and Necrotic Core plaques but normally should be classified to the lipid or fibrofatty classes [53],[9]. The block diagram of the proposed algorithm is shown in figure 5.33.

5.4.1. Shadow Detection

Shadow areas appearing in IVUS gray scale images usually do not represent any useful information for plaque component analysis. However, the IVUS-VH method does not detect such regions and blindly treats them as normal plaque area which often leads to classification errors. By defining a specific plaque region as shadow region shown in figure 5.34 [72], we aim at reducing mentioned errors, which are caused by the nature of ultrasound imaging. Shadow regions are characterized by infra-low intensity regions behind ultra-high intensity areas along a scanline. Thereby, detection of these regions by using two thresholds are proposed: one threshold T_{high} to detect ultra-high intensity regions, which might belong to calcification or necrotic core, and the other threshold T_{low} to detect infra-low intensity regions. Let us consider an image I from gray level IVUS in polar domain. If Σ denoted as the ensemble of pixels belonging to a shadow region, these pixels x can be detected along a scanline as follows:

$$x = (i,j) \in \Sigma \text{ if } \begin{cases} I(i,j) < T_{low} \text{ and } I(i,j-1) \in \Sigma \\ \text{or } I(i,j) < T_{low} \text{ and } I(i,j-1) > T_{high} \end{cases} \tag{5.65}$$

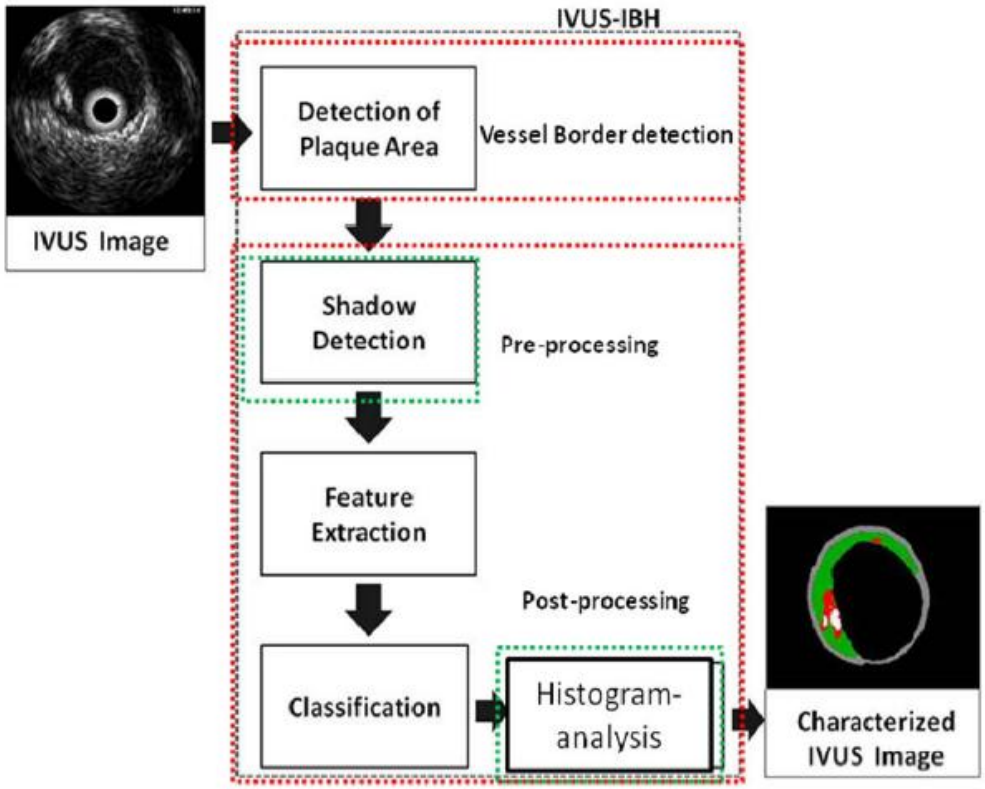

Figure 5.33.: Scheme of the workflow in the IBH-System(in GUI). First, an IVUS image is loaded. Then, the vessel's borders are detected using automatic border detection. Next, the textural features are extracted from the plaque area and then, SVM classifier is applied to classify the pixels of the plaque area in order to generate the color coded image representing the different plaque components. Finally, the post-processing is applied on SVM output.

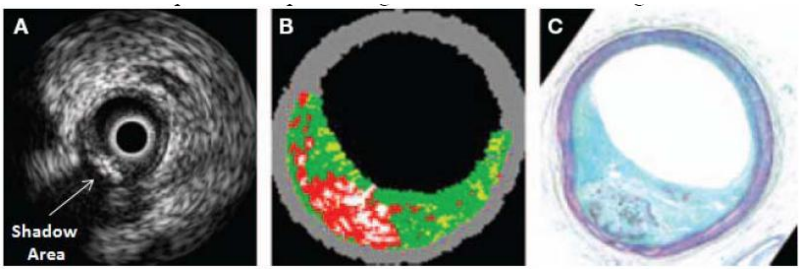

Figure 5.34.: The shadow region in a typical IVUS gray-scale image (left) its plaque constituents in IVUS-VH (middle) and its corresponding histopathalogy (right) [43].

5.4.2. Feature Extraction Methods

In order to characterize the rest of plaque area into the three pre-defined plaque components, two feature extraction methods are examined and compared. To achieve this purpose, local binary pattern (LBP) [62] and co-occurrence [32] feature extraction methods have been studied in [11] and have been reported to outperform other feature extraction methods. Moreover, it was reported in [90] that the Run-length method [83] is not an appropriate feature extraction method for characterizing IVUS images plaque area. In [21], both signal and image-based features were extracted. The co-occurrence, LBP, and Gabor-filtering feature extraction methods are used for texture-based feature extraction. Their results are compared to manual characterization of IVUS images by two experts and 90% accuracy is achieved. However, the manual characterization of IVUS images suffers from both inter-observer and intra-observer variability and especially uncertainty in characterizing soft plaques from each other, e.g. distinguishing between the FF and the NC tissues. Here, the performance of the features extracted from the Run-length matrix is compared with those extracted from the LBP method in both accuracy and time efficiency aspects. The co-occurrence feature extraction method is not included in this study, since the previous studies reveal that despite good performance of this method in atherosclerotic plaque characterization, its heavy computational burden leads to poor time efficiency. IVUS imaging provides circular cross-section areas of the blood vessel and it uses 256 scan lines so the lateral resolution is $360/256 = 1.41$ degrees and the axial resolution is about 40 microns. For the analysis, IVUS images are converted into polar coordinates to be orientation-independent for the feature extraction. In this manuscript, the data refers to the converted data. The polar transformed image is then swept by a sweeping window. The size of the sweeping window for both feature extraction techniques was empirically chosen as 9×9 pixels which each pixel is equal to $0.025mm$.

5.4.3. Practical Implementation

The proposed methods for border detection and plaque characterization in this study were implemented in MATLAB and to obtain a standalone executable application, the program with a graphical user interface (GUI) was compiled by C++ compiler in Microsoft Visual Studio 2005. An example of the GUI is illustrated in figure 5.35.

5.4.4. Result of Algorithm III

Considering the shadow region detection procedure, 8% of plaque area pixels belong to the shadow region. The characterized IVUS images were validated by their corresponding VH images. In order to demonstrate the influence of applying the pre-processing step, i.e. detecting the shadow region and assigning it to the fourth class, and the post-processing derived from the histogram analysis. In the post-processing step, the label assigned to a sample pixel and its gray-level are considered. Then, final labels of the pixelare decided by this step. For instance, suppose the classification section assign a pixel to the FF class and also the gray-level of that pixel is above 150. In this case, based on ThFF, the current label is declined and whether the gray-level is above ThDC (low)=200 or not, it will be assigned to the DC or NC class, respectively. Table 5.3 and table 5.4 illustrate the comparative results of

Figure 5.35.: An example of the GUI window: Besides analysis of plaque components the GUI also allows calculation of other vessel parameters such as total plaque areas or the degree of stenosis.

the two different feature extraction methods considering different conditions. Considering the VH as validating standard, the Kappa is computed to be 0.61 for the extended Run-length for both pixel-based and region-based(with a 9×9 pixels in a window) validations in the case of applying both pre-processing and post-processing steps.

Table 5.5 illustrates the P-value for the case of applying both shadow detection(pre-processing) and histogram-based post-processing and also using the new extended Run-length method as a technique for feature extraction.

Figure 5.36 shows the influence of shadow region detection pre-processing on the final reconstructed IBH image. Figure 5.37 illustrates the influence of post-processing derived from histogram analysis on the final reconstructed IBH image. Finally, figure 5.38 shows the final reconstructed IBH images for two feature extraction methods.

Moreover, table 5.3 also shows the statistical results of applying the proposed algorithm to these images. In most similar studies, when one wants to validate with correlated images a region-based validation method is used. It means that instead of comparing the result and its corresponding label pixel by pixel, the validation step is done by comparing regions, a window which contains more than one pixel. For example, the size of validation regions in Nair et al. is $1/3mm \times 1/3mm$, i.e. approximately a window of size 13×13 pixels. To handle this, a validation window of size $n \times n$ pixels is defined, where n can vary from one i.e. pixel-based validation, to 9. The label of a validation window is selected by looking at labels of its constituent pixels. In fact, it is assigned to a plaque component which is the majority. This experiment shows that the size of regions affects the results.

Table 5.3.: Results of pixel-based plaque characterization of vessels' plaque area using the Run-length method as feature extraction and SVM classifier. The cases of including the pre and post-processing steps or not is distinguished using "Yes" and "No" signs in the two left columns. The parameter ± Confidence Interval is shown for the Sensitivity, Specificity, and Accuracy parameters.

Histogram based post processing	**Shadow detection**	**DC**		**FF**		**NC**		**Overall Accuracy**
		Sensitivity	Specificity	Sensitivity	Specificity	Sensitivity	Specificity	
No	No	79% ± 6.5	93% ± 3.8	87% ± 5.1	38% ± 5.3	07% ± 3.3	97% ± 2.5	72% ± 6.3
No	Yes	79% ± 6.5	93% ± 3.7	96% ± 3	55% ± 6.6	12% ± 4.2	96% ± 2.7	74% ± 5.8
Yes	No	80% ± 6.5	93% ± 3.7	73% ± 6	64% ± 6.5	43% ± 6.6	80% ± 5.3	74% ± 6.4
Yes Pixel Based	Yes Pixel Based	79% ± 6.5	85% ± 3.6	81% ± 5.6	90% ± 5.3	52% ± 6.6	82% ± 5.5	75% ± 6.1
Yes Region Based: 9 × 9 Pixels	Yes Region Based: 9 × 9 Pixels	71% ± 4	97% ± 1	88% ± 1	87% ± 2	57% ± 4	88% ± 1	85% ± 3

Table 5.4.: Results of pixel-wise plaque characterization of vessels' plaque area using the LBP method as feature extraction and SVM classifier. The cases of including the pre and post-processing steps or not is distinguished using "Yes" and "No" signs in the two left columns. The parameter ± Confidence Interval is shown for the Sensitivity, Specificity, and Accuracy parameters.

Histogram based post processing	**Shadow detection**	**DC**		**FF**		**NC**		**Overall Accuracy**
		Sensitivity	Specificity	Sensitivity	Specificity	Sensitivity	Specificity	
No	No	68% ± 6.6	96% ± 3.2	97% ± 3	42% ± 6.6	06% ± 4.6	95% ± 3.2	66% ± 6.1
No	Yes	68% ± 6.6	94% ± 3.1	95% ± 3	45% ± 6.6	13% ± 4.5	94% ± 3.2	69% ± 6.6
Yes	No	69% ± 6.4	96% ± 3.2	70% ± 5.8	61% ± 5.2	39% ± 6.1	79% ± 5.7	67% ± 6.1
Yes	Yes	69% ± 6.4	95% ± 3.1	75% ± 5.8	81% ± 5.2	42% ± 6.6	76% ± 5.7	72% ± 5.8

Table 5.5.: The p-value shows differences of the case of applying both shadow detection preprocessing and post-processing and using the Run-length method as a technique for feature extraction against the Run-length method without pre-processing and histogram-based post-processing.

Parameter	Sensitivity DC	Sensitivity FF	Sensitivity NC	Specificity DC	Specificity FF	Specificity NC	Accuracy
p-value	0.02781	0.01827	0.00497	0.02607	0.00695	0.01397	0.02345

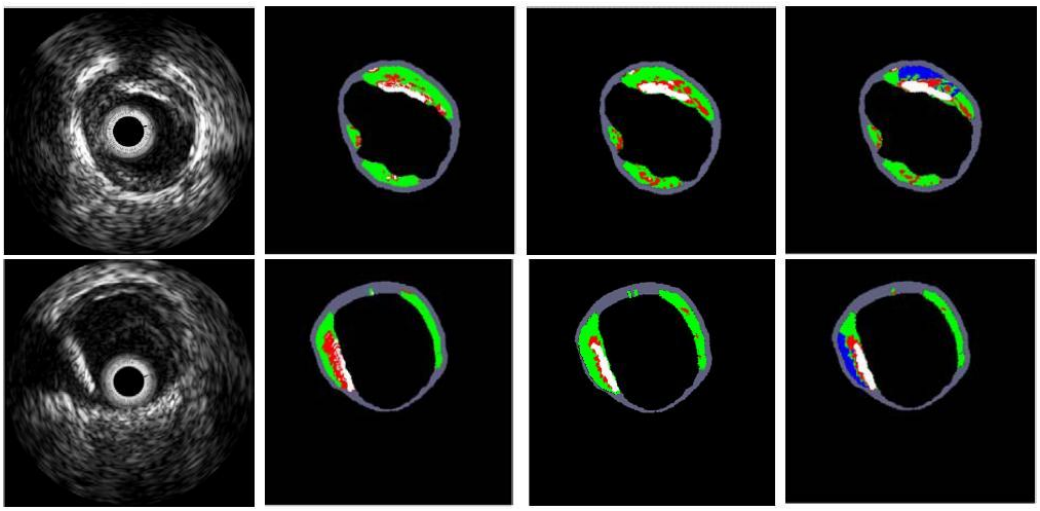

Figure 5.36.: The influence of applying the shadow detection section in the final constructed color-coded IBH images. The images are from left to right: a typical IVUS image, its corresponding VH image, IBH images without shadow section and with shadow detection section using the Run-length feature extraction method. Note that the illustrated IBH images are after applying the histogram-based post-processing technique. (The FF, NC, and DC plaques are shown in green, red, and white colors, respectively. The shadow region is colored with blue).

5.4.5. Discussion of Algorithm III

In Algorithm III, a complete algorithm was introduced for the IVUS image analysis including border detection (only in GUI) to plaque characterization with more emphasis in the latter part. This comprehensive image-based algorithm provides cardiologists with, not only the vessel's intima and media-adventitia borders but also with a color-coded IBH image in which the location and distribution of different plaque components of atherosclerotic plaques are illustrated. Furthermore, when cardiologists analyze a sequence of IVUS images, additional clinical parameters together with the percentage of different plaque components can be useful.

Perhaps, one of the important advantages of the proposed algorithm is to increase the longitudinal resolution of plaque composition analysis. The present VH-derived plaque composition analysis provides only ECG triggered images. As mentioned above, in an imaging procedure with the rate of 30 *frames/sec* only one IVUS frame out of approximately

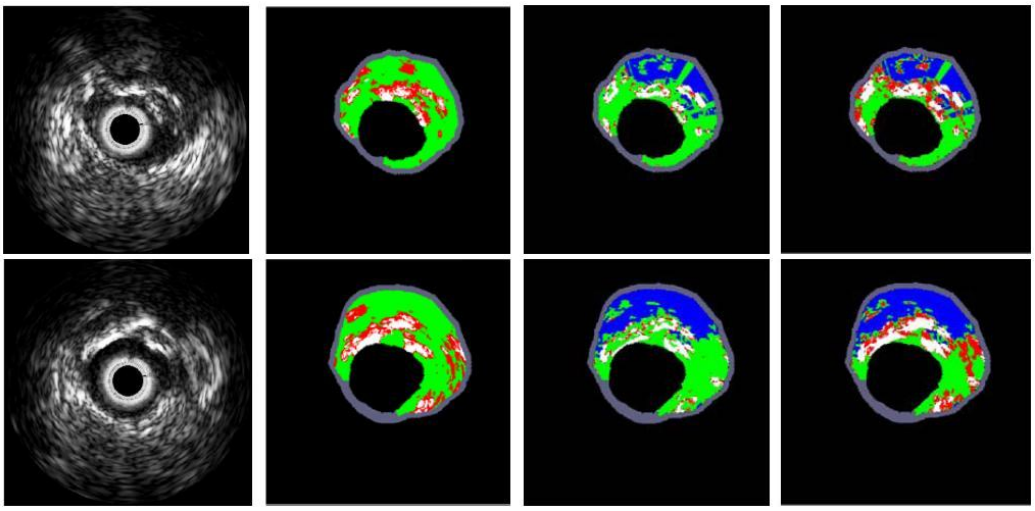

Figure 5.37.: The influence of applying the histogram-based post-processing section in the final constructed color-coded IBH images. The images are from left to right: a typical IVUS image, its corresponding VH image, IBH images before applying the histogram-based post-processing and after that using the LBP feature extraction method. Note that the illustrated IBH images are after applying the shadow detection technique. (The FF, NC, and DC plaques are shown in green, red, and white colors, respectively. The shadow region is colored with blue).

30 IVUS frames is considered to generate the color-coded VH image.

As it is shown in figure 5.33, the proposed algorithm contains different sections including plaque area detection, shadow region detection as a pre-processing, textural feature extraction, classification by SVM, and post-processing based on the data derived from the histogram analysis. The differences in the results of the tables 5.3 and 5.4 and also those illustrated in figure 5.37 show the influence of adding the shadow region detection as a pre-processing section. One of the obvious advantages to add the shadow region detection is to help algorithm to improve the detection of all three kinds of atherosclerosis plaque components.

Moreover, this technique provides us with a more general algorithm which can be more reliable when in studying patients with calcified plaques in which, a lateral shadow region behind the calcified area exists. Out of the total number of 191582 pixels was contained in the shadow region, 63%, 36%, and about 1% was respectively characterized into FF, NC, and DC plaques by the VH algorithm. Therefore, tables 5.3 and 5.4 show that in addition to improving the distinction of three plaque components, the shadow detection procedure has a direct influence on the detection of FF and NC. Differences of relative amounts of DC and NC between after and before shadow detection were calculated 5% and 4% are respectively.

One should note that the IVUS-IBH images in the 3^{rd} and 4^{th} column of figure 5.37 show small islands of green within the blue shadow regions. Once shadowing occurs due to calcium, the RF signal is attenuated and one doesn't expect to see these islands. This may be due to multiple reflections between the catheter and the calcium causing artifact.

By comparing the results of the table 5.3 and table 5.4, it can be concluded that the

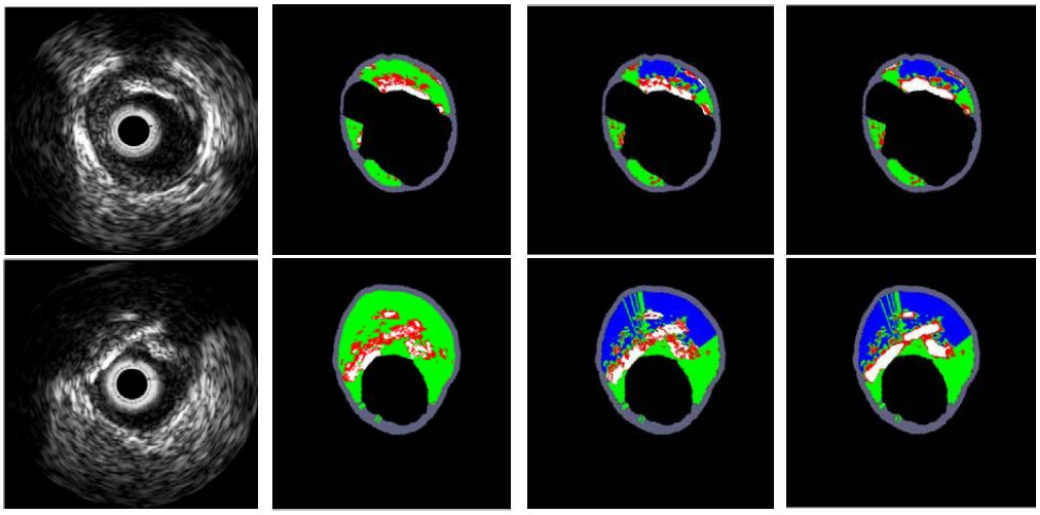

Figure 5.38.: The final constructed color-coded IBH images using the proposed algorithm. From left to right: An IVUS image, its related VH image and its IBH images using the Run-length and the LBP feature extraction methods.

new extended Run-length feature extraction method outperforms the LBP in classifying all plaque components. However, as illustrated in figure 5.38, it is quite clear that the color-coded image reconstructed with the use of LBP feature extraction method is more detailed. This may be caused by the multi-resolution characteristic of this method. Perhaps, one future direction is to combine these two feature extraction methods in order to benefit from their both detailed and accurate results.

The computation times of the feature extraction methods are as follows: for a typical frame, i.e. the plaque area containing around 5000 pixels out of the total 160000 IVUS image's pixels, the new extended Run-length method took approximately 7-20 seconds to extract the features whereas the LBP took 2-5 minutes. Thus, in terms of time efficiency, the new extended Run-length method further outperforms the LBP method. However a more optimized implementation in C++ will further speed up the algorithms as expected. The influence of the post-processing step after classification is highlighted in the differences in the sensitivity and specificity of the algorithm in characterizing NC and FF plaques, respectively. The extensive textural similarities between the NC regions and other plaque components defined by VH leads to preventing the classification part of the algorithm from identifying it; however, by studying the distribution of plaques' intensities in the dataset, it is concluded that in addition to textural features, there exists some rules for distinguishing the plaques in it (figure 5.33).

This Kappa =0.61(for both pixel-based and region-based validation) clearly represents that the classification results are in good agreement with VH after detecting and removing shadow regions. Moreover, the low values of CI and P-value show the reliability and consistency of these results obtained for this data-set. The P- values indicated in table 5.5 answer the following question If the method's performance is the same as the before applying shadow detection and post-processing, what is the probability of observing the current result. From a statistical point of view, the observed difference in these results compared

to the results of the methods before detecting shadow and applying post-processing is not accidental.

An interesting point it should be mentioned here is that the results presented suggest that the texture based algorithm based on IVUS gray-scale images produces similar images and has a modest co-relation to VH-IVUS, suggesting that most of the information in VH-IVUS tissue characterization comes from the intensity of the ultrasound signal, and less-so on the underlying radio-frequency data. In this study, all methods' sensitivity to detect the NC was low (maximum value is 57%). The fact that detection of NC by studying the IVUS images is not a straight-forward procedure has also been previously discussed in [30] and [60]. This phenomenon was caused by similarities between NC and DC in gray-level IVUS images. This fact supports the previous studies which have shown that plaque areas adjacent to dense calcium are frequently coded as necrotic tissue in VH images [76]. By considering selected cross sections that contained plaque areas with a homogeneous tissue composition as reported in [30], the accuracy results can be increased significantly. Although the sensitivity of detecting the calcified region was 79%, the algorithm performance to detect the focal calcified region in the images was more than 85%, which is another important point about these results. It derives from the fact that in the VH method the variation of pixels intensities assigned to the calcium class is very high (from 0 to 256) as can be observed in figure 5.26. However, since identifying focal calcified regions are more important than speckled calcification in the plaque area, the proposed algorithm shows increased reliability [92].

5.5. Algorithm IV

A definition of LBP and new extended Run-length (NRL) features and the experiences of the previous algorithms indicates that these two feature extraction methods assess the texture from two different aspects. Hence their combination may enhance the accuracy of texture analysis methods and in this case the accuracy of plaque characterization. Moreover, in the previous algorithms, post-processing was applied to take advantage of the gray-level distribution of each plaque type to confirm or correct the labels given to each pixel by the classifier. Improvement of the results after applying the post-processing stage proved that gray-level information are valuable information that are not completely included in the LBP, NRL, or other structural features. However, as the histograms of plaques are not distinctly separated from each other (figure 5.39), the post-processing method is not sufficiently reliable. Furthermore, shapes of histograms may differ from one dataset to another that demands the histogram analysis be repeated for every new dataset. This imposes an unnecessary computational load. Moreover, the sharp decision thresholds in the post-processing can destroy the effect of discriminative hyper-planes detected by the classifiers.

In this algorithm, algorithm IV, LBP and NRL were combined to benefit the advantages of both features. Also, in order to dispose of the post-processing stage and its shortcomings mentioned above, adding the gray-level information in the form of features was proposed in combination with LBP and NRL features to better classify the plaque types. These new features are the modified Hu Moments and a newly proposed neighboring gray-level feature.

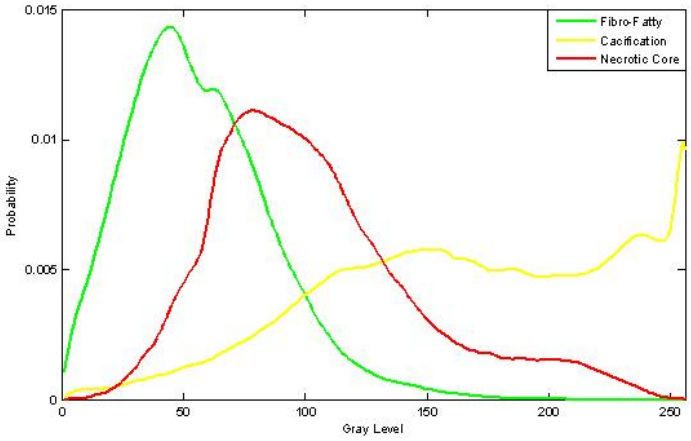

Figure 5.39.: Histogram of three plaque types in IVUS images: Fibro-Fatty (Green), Necrotic Core (Red) and Calcification (Yellow).

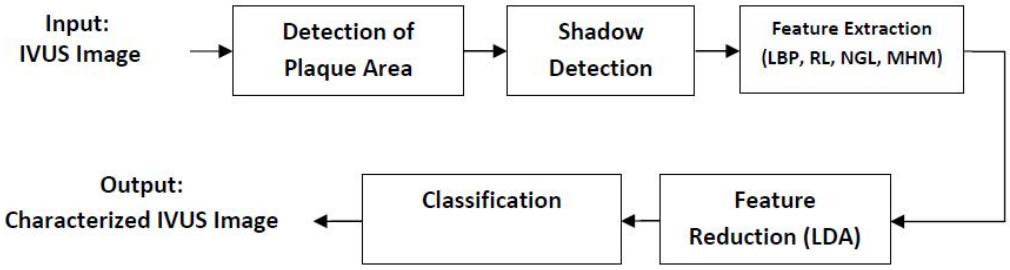

Figure 5.40.: Block diagram of Algorithm IV.

5.5.1. Neighboring Gray-Level (NGL) Feature

As mentioned above, the features used in the previous algorithms are structural features and do not take into account directly the gray-level values of the pixels contained in the sweeping windows. However, there exists valuable discriminative information in the distribution of the gray-levels and a new set of features capable of describing the useful gray-level information is proposed here. Suppose for each pixel (i, j) of the image I,a$(M + 1) \times (N + 1)$ neighborhood $I\{i + m, j + n\}$ with $m \in \{-\frac{M}{2}, \frac{M}{2}\}$ and $n \in \{-\frac{N}{2}, \frac{N}{2}\}$ is adopted. For the newly proposed gray-level feature, $M = N =$ 2is considered to have the smallest neighborhood, i.e. a 3×3 window. Let g_c be the gray value of the center pixel and $g_n, n = 1, 2, ..., 8$ be the gray values of the 8 neighbor pixels. So, nine gray-levels of the pixels contained in that window are used as a feature vector $F = (gc, g1, g2, ..., g8)$. Since these features are sensitive to translation and rotation, the features are sorted in an ascending order to get rid of these effects. An illustration of the mean neighborhood gray-level is shown in figure 5.41.

Figure 5.41.: Illustration of the neighboring gray-level feature (mean value of gray-levels is shown): Plaque Area in Polar Coordinates (left) and Mean neighborhood gray-level (right).

5.5.2. Modified Hu Moments (MHM)

The moments mix gray-level and position information of pixels of an image to yield a new feature for texture analysis [85]. Actually, the moments show how gray-levels distribute in an image.They are defined as follows:

$$m_{pq} = \sum_i \sum_j i^p j^q I(i, j) \tag{5.66}$$

That is called a moment of order $p + q$. However, these moments lack the invariance property (i.e. they are rotational, translational, and scale variant). Thereby, central moments are defined that are invariant to translation:

$$\mu_{pq} = \sum_i \sum_j (i - \bar{i})^p (j - \bar{j})^q I(i, j) \qquad \bar{i} = \frac{m_{10}}{m_{00}} \quad , \quad \bar{j} = \frac{m_{01}}{m_{00}} \tag{5.67}$$

But central moments are still scale and rotational invariant. A commonly used group of moments in texture analysis are Hu Moments described in table 5.6. Although Hu moments are rotational, translational, and scale invariant but they are not invariant to affine transforms, for example, multiplication of whole image pixels by a numeric constant. These affine transforms are associated to images with different acquisition gains.

Table 5.6.: Hu Moments Mathematical Expressions[75].

$$\phi_1 = \eta_{20} + \eta_{02} \qquad \phi_2 = (\eta_{20} - \eta_{02})^2 + 4\eta_{11}^2$$

$$\phi_3 = (\eta_{30} - 3\eta_{12})^2 + (3\eta_{21} - \eta_{03})^2 \qquad \phi_4 = (\eta_{30} + \eta_{12})^2 + (\eta_{21} + \eta_{03})^2$$

$$\phi_5 = (\eta_{30} - 3\eta_{12})(\eta_{30} + \eta_{12})\left[(\eta_{30} + \eta_{12})^2 - 3(\eta_{21} + \eta_{03})^2\right] + (3\eta_{21} - \eta_{03})(\eta_{21} + \eta_{03})\left[3(\eta_{21} + \eta_{03})^2 - (\eta_{21} + \eta_{03})^2\right]$$

$$\phi_6 = (\eta_{20} - \eta_{02})\left[(\eta_{30} + \eta_{12})^2 - (\eta_{21} + \eta_{03})^2\right] + 4\eta_{21}(\eta_{30} + \eta_{12})(\eta_{21} + \eta_{03})$$

$$\phi_7 = (3\eta_{21} - \eta_{03})(\eta_{30} + \eta_{12})\left[(\eta_{30} + \eta_{12})^2 - 3(\eta_{21} + \eta_{03})^2\right] + (3\eta_{12} - \eta_{30})(\eta_{21} + \eta_{03})\left[3(\eta_{30} + \eta_{12})^2 - (\eta_{21} + \eta_{03})^2\right]$$

$$\text{where } \eta_{pq} = \frac{\mu_{pq}}{\mu_{00}^{\gamma}}, \quad \gamma = \frac{p+q}{2} + 1, \text{for: } p + q = 2, 3, \ldots$$

In order to solve this problem, a new set of invariants were proposed in [75]. Suppose that:

$$F_P(u) = sign(u).|u|^P \tag{5.68}$$

the new features are then described as follows:

$$f_1 = \frac{F_2(\phi_2)}{\phi_1} \tag{5.69}$$

Figure 5.42.: Illustration of Hu feature f_1 : Plaque Area in Polar Coordinates (left) and f_1 (right).

$$f_2 = \frac{F_3(\phi_3)}{\phi_1} \tag{5.70}$$

$$f_3 = \frac{F_3(\phi_4)}{\phi_1} \tag{5.71}$$

Figure 5.43.: Illustration of Hu feature f_2 : Plaque Area in Polar Coordinates (left) and f_2 (right).

Figure 5.44.: Illustration of Hu feature f_3 : Plaque Area in Polar Coordinates (left) and f_3 (right).

$$f_4 = \frac{F_6(\phi_5)}{\phi_1} \tag{5.72}$$

Figure 5.45.: Illustration of Hu feature f_4 : Plaque Area in Polar Coordinates (left) and f_4 (right).

$$f_5 = \frac{F_4(\phi_6)}{\phi_1} \tag{5.73}$$

$$f_6 = \frac{F_6(\phi_7)}{\phi_1} \tag{5.74}$$

This set has shown lower sensitivity to translation, rotation, scale and affine transforms than the conventional Hu Moments.

5.5.3. Result of Algorithm IV

The study group used for algorithm IV is the same as the one used for algorithm III. After shadow detection, the LBP, NRL, NGL and MHM features were extracted from the remaining plaque area. The characterized IVUS images were validated by their corresponding VH images.Sensitivity, specificity and accuracy parameters were then calculated in order to assess the performance of the new algorithm. Results are shown in table 5.7. In order to find out the impact of the new features the results were compared to the case that NRL and LBP was concerned.

Figure 5.46.: Illustration of Hu feature f_5 : Plaque Area in Polar Coordinates (left) and f_5 (right).

Figure 5.47.: Illustration of Hu feature f_6 : Plaque Area in Polar Coordinates (left) and f_6 (right).

Table 5.7.: The Results of Algorithm IV versus other techniques.

Method	**DC**		**FF**		**NC**		**Overall**
	Sensitivity	Specificity	Sensitivity	Specificity	Sensitivity	Specificity	**Accuracy**
LBP	58%	85%	83%	81%	46%	77%	62%
NRL	79%	85%	81%	90%	52%	82%	71%
LBP+NRL	78%	86%	82%	90%	56%	82%	72%
LBP+NRL+NGL+MHM	80%	86%	80%	92%	60%	81%	73%

Results of table 5.7 shows that the combination of features enhanced the classification accuracy and especially the detection of Necrotic Core (concluded based on sensitivity and specificity of NC). Also figures 5.48 and 5.49 illustrate the images characterized by all methods with their corresponding IVUS and VH images.

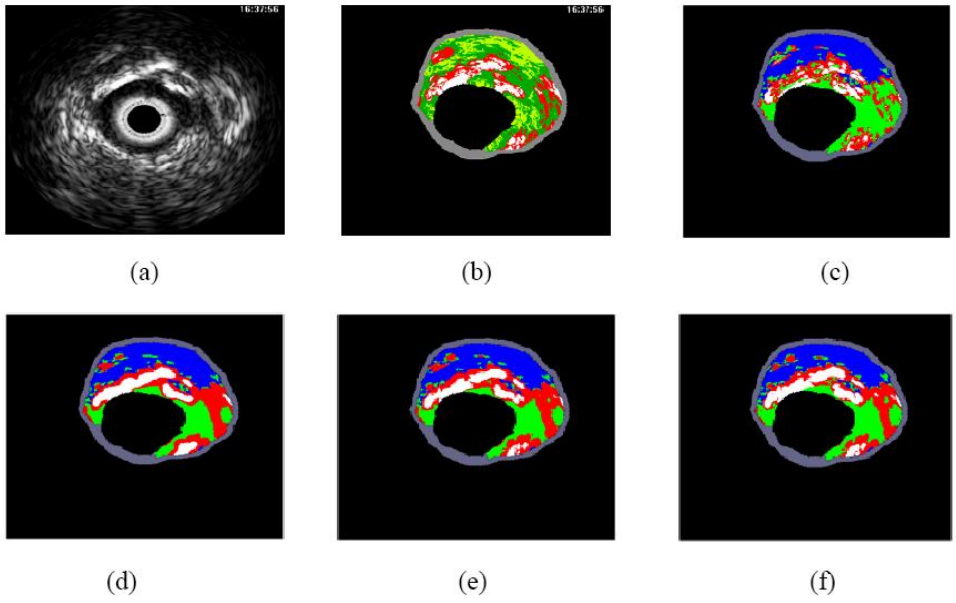

Figure 5.48.: (a) IVUS image, (b) its corresponding VH image, (c) reconstructed image by LBP method, (d) reconstructed image by NRL method, (e) reconstructed image by LBP+NRL method and (f) reconstructed image by Algorithm IV.

Combination of different types of features results in large feature vectors and hence a complex feature space. Classification in such feature spaces is very time-consuming. In such cases, in order to increase the efficiency of classifiers, feature reduction methods are applied to feature vectors before they are fed to the classifiers. LDA was chosen that has been best suited to this work.

5.5.4. Linear Discriminant Analysis

LDA was applied to the feature space. However, the question is how to choose the L (L $<$ # of features) most significant directions? In LDA method, each direction is given a value that indicates the separation ability of that direction. In order to choose the L most significant directions, we start with the most significant direction and determine its separation ability (i.e. the ratio of its value to the sum of all directions' values). Then the second most significant direction is added to the first one and its separation ability is calculated. This procedure is repeated until adding directions does not change the separation value effectively. Thereby, the number at which this happen is the optimum number of directions. For example in this case, adding more directions to the five first most significant directions

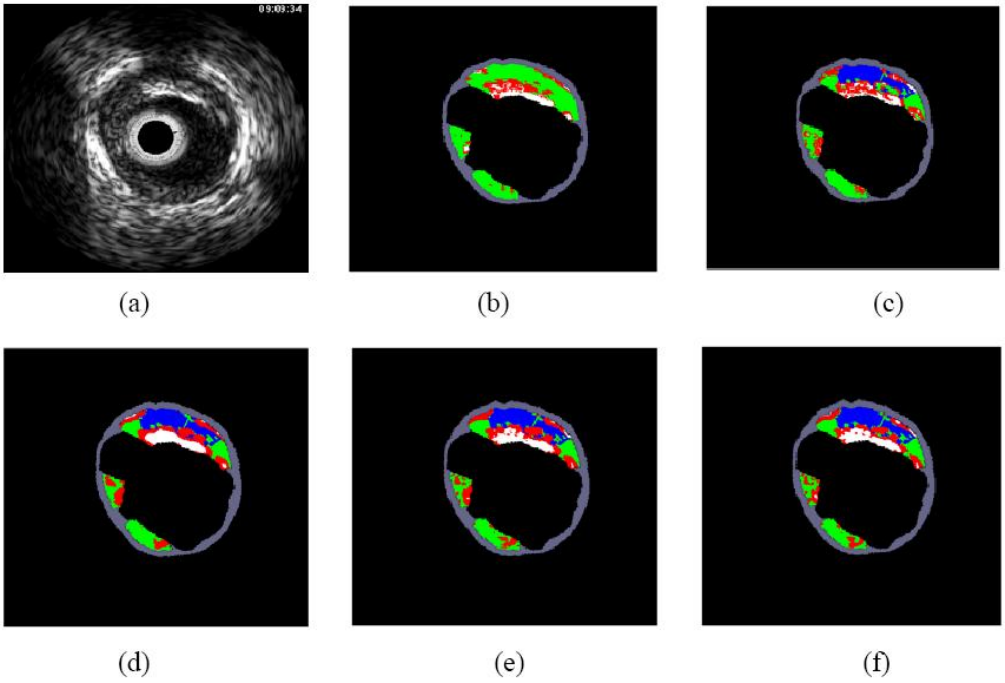

Figure 5.49.: (a) IVUS image, (b) its corresponding VH image, (c) reconstructed image by LBP method, (d) reconstructed image by NRL method, (e) reconstructed image by LBP+NRL method and (f) reconstructed image by Algorithm IV.

Table 5.8.: ECOC code map used in the classification.

Classes	Classifier 1	Classifier 2	Classifier 3
Dense Calcium	1	1	0
Fibro-Lipid	-1	0	1
Necrotic Core	0	-1	-1

does not affect the percentage of separation (figure 5.50). So five is the optimum number of directions.

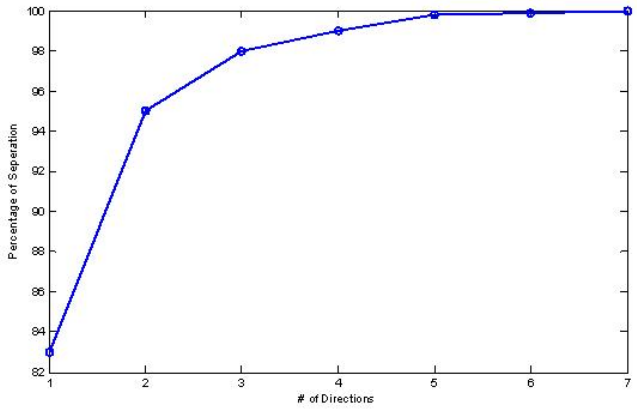

Figure 5.50.: Separation Percentage does not change effectively selecting more than 5 LDA directions.

Error-Correcting Output Codes(ECOC) Classifier

The ECOC technique can be broken down into two distinct stages: encoding and decoding. Given a set of classes, the coding stage designs a codeword (a sequence of bits of a code representing each class, where each bit identifies the membership of the class for a given binary classifier) for each class based on different binary problems. The decoding stage makes a classification decision for a given test sample based on the value of the output code [21]. Given a set of N_C classes to be learned, at the coding step of the ECOC framework, different bi-partitions (groups of classes) are formed, and binary classifiers (dichotomies) are trained. As a result, a codeword of length n is obtained for each class, where each bit of the code corresponds to the response of a given dichotomy: ± 1 if the class is considered by the dichotomy ($+$ or $-$ is decided by the dichotomy) and 0 if the class is not considered by the dichotomy. Figure 5.51 shows an example of ECOC for a three class problem (C_1, C_2 and C_3). Three dichotomies $\{h_1, h_2, h_3\}$ are formed for a three-class problem where each dichotomy learns to split a pair of classes. For example, the first classifier h_1 is trained to discriminate C_1 versus C_2 ignoring C_3. According to these dichotomies, a code is assigned to each class. The white regions represent the code 1 (considered as positive for its respective dichotomy h_i), the dark regions represent the code -1 (considered as negative for its respective dichotomy h_i), and the grey regions represent the code 0 (not considered classes by the current dichotomy).

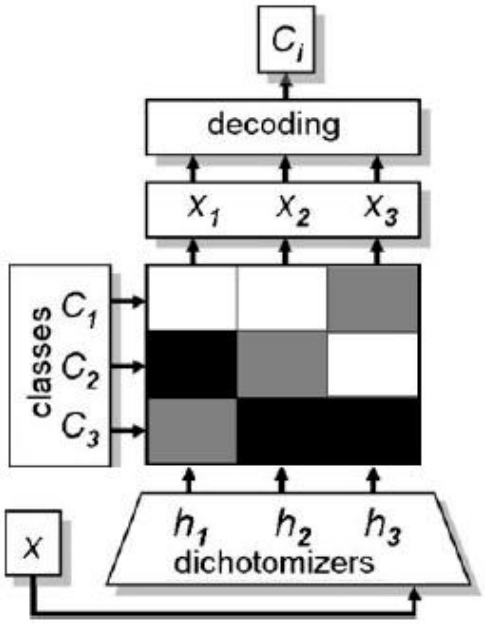

Figure 5.51.: Example of ECOC classification for a three-class problem [21].

5.5.5. Result of Algorithm IV After Applying LDA and ECOC

Results are shown in table 5.9. According to the results, applying LDA would not severely affect the results while reducing the classification time. Furthermore, as SVM and ECOC result in nearly same accuracies, it can be concluded that this is the highest results achievable with these features.

Table 5.9.: The Results of Algorithm IV evaluated with different classifiers with and without LDA.

Method	Feature Reduction	Classifier	Metric	DC	FF	NC	Overall Accuracy
NRL+LBP+NGL+MHM	None	SVM	Sensitivity	80%	80%	60%	73%
			Specificity	86%	92%	81%	
NRL+LBP+NGL+MHM	LDA	SVM	Sensitivity	79 %	78%	59%	72 %
			Specificity	86%	92%	81%	
NRL+LBP+NGL+MHM	None	ECOC	Sensitivity	79%	80%	61%	74%
			Specificity	87%	91%	82%	
NRL+LBP+NGL+MHM	LDA	ECOC	Sensitivity	80%	80%	60%	73%
			Specificity	87%	91%	82%	

Discussion of Algorithm IV

Algorithm IV is an improvement of the previous algorithms. It is mainly designed for, first, removing the histogram-based post-processing stage by adding some gray-level features

at the feature extraction stage and, secondly, assessing the performance of combination of the previously introduced texture features. Since combination of several features would lead to a high dimensional feature vector of (49 features), LDA is used to optimally reduce the number of features. At the classification stage, also ECOC classifier is used (rather than SVM classifier) in order to assess the reliability of the obtained results.

It is concluded from table 5.7 that the proposed gray-level based features, NGL and MHM, can successfully play the role of histogram-based post-processing step. Furthermore, combination of features although increases the feature vector dimension, but improves the accuracy of plaque characterization algorithm especially in identifying NC plaque component. Moreover, comparison of figure 5.48 (e) to figures 5.48 (c) and (d) shows that a more detailed image is produced combining NRL and LBP.

Also, the results in table 5.9 show that applying LDA would not severely affect the results and almost the same results are yielded. However, using this method reduces the complexity of feature space that helps SVM to find the discrimination hyper-planes faster and easier. Furthermore, based on this Table, the results obtained with SVM and ECOC are close to each other. An interpretation is that this is the highest achievable accuracy using image based methods in comparison to VH.

The major contribution of this algorithm is the improvement of in detecting NC class comparing to the previous algorithms. Considering loss of information in the procedure of transforming RF signal to IVUS image and the reverberation phenomenon in the shadow region, it is really promising to obtain these results. These results support the idea that most discriminative information used in VH analysis comes from the amplitude of RF signals.

Table 5.10 shows a comparison chart of four algorithms proposed in this chapter.

Table 5.10.: Summary of four algorithms proposed in this chapter.

Method	Contribution	DC Sen.(Spe.)	FF Sen.(Spe.)	NC Sen.(Spe.)	Accuracy
Algorithm I [Published in ISBI 2009]	-Modified Run-Length	70 %(95 %)	84 %(75 %)	55 %(82 %)	77 %
Algorithm II [Published in SPIE 2010]	-Redundant Wavelet- Packet Transform	73 %(93 %)	85 %(79 %)	42 %(84 %)	72 %
Algorithm III [Accepted in UBM Journal]	-Shadow Detection -GUI	79 %(85 %)	81 %(90 %)	52 %(82 %)	75 %
Algorithm IV (SVM) (ECOC) [Under Submission IEEE TITB Journal]	-Introducing New Feature -Feature Combination -Removing Post-Processing -LRE	79 %(86 %) 80 %(87 %)	78 %(92 %) 80 %(91 %)	59 %(81 %) 60 %(82 %)	72 % 73 %

6. Chapter Six: Validation

A five-fold cross validation approach is considered for validating the proposed algorithms. In this validation scheme, first, the feature vectors extracted from all images of the dataset are joined with each other to form a feature matrix. Then, this matrix is shuffled so that the feature vectors of different classes are distributed randomly. After shuffling, this matrix is divided into five equal parts. In each validation step, four parts are considered as training dataset used to train the classifier. The trained classifier is then tested with the remaining part. This procedure is repeated five times, each time with a new part as test data. The steps of a five-fold cross validation are shown in figure 6.1. Finally, the averages of the results derived from all steps are reported as the total result of classifier. These results are known to be more reliable than the other validation methods when sufficient number data is available.

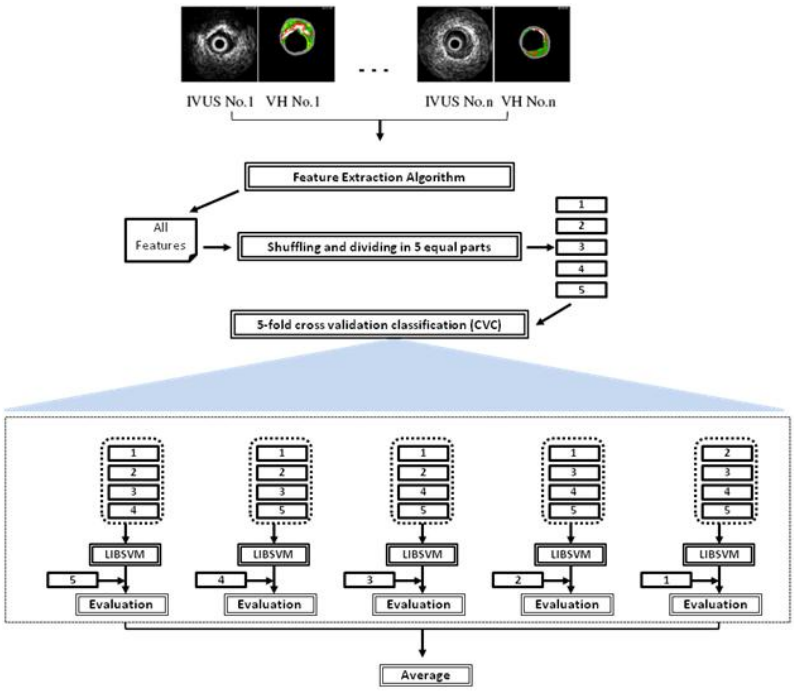

Figure 6.1.: Illustration of 5-fold cross validation

6.1. In-Vivo Validation

For *in vivo* validation, 120 new IVUS images, which were not included in the classification neither as training data nor as test data, were considered to be characterized using algorithm IV. For this purpose, a SVM classifier was trained using the whole dataset excluding these images. Figure 6.2 shows the reconstructed images after applying Algorithm IV to three different IVUS images. Average accuracy for the images that participated in *in-vivo validation* was measured 78%.

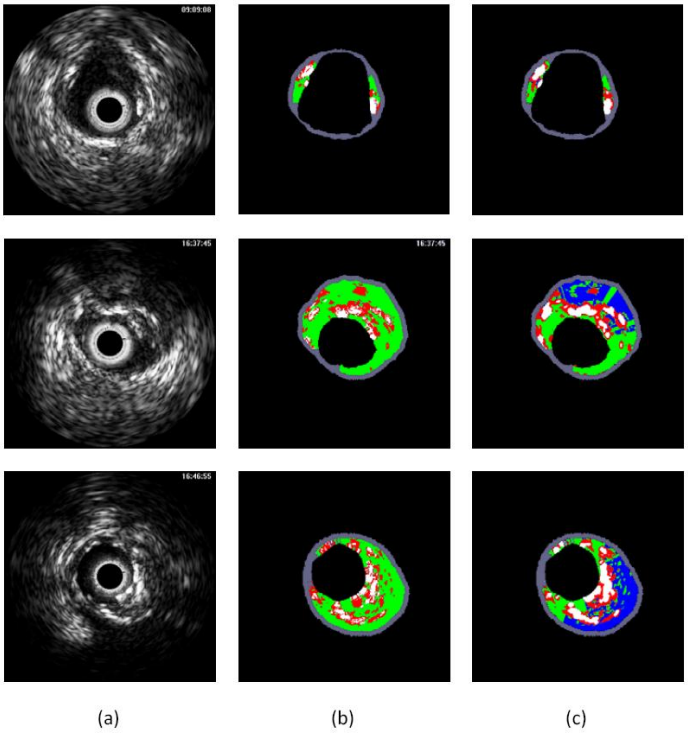

Figure 6.2.: (a) IVUS image, (b) its corresponding VH image and (c) reconstructed image by Algorithm IV.

6.1.1. Statistical Analysis of In-Vivo Validation

The VH and Algorithm IV interpretation of the plaque components of 120 images tested *in-vivo* are reported in table 6.1. The sensitivity, specificity and accuracy of each plaque components are listed in table 6.2. The kappa value was calculated to be 0.639 indicating good agreement. The bold numbers in table 6.1 illustrate the number of pixels characterized as the same plaque component by two methods, and the bold number at the last column shows the total number of pixels which have been characterized in 120 images collectively. The truth table shown in table 6.1 contains a great amount of information which one can use to compare the proposed method to VH. First, the number of pixels detected in the proposed method is explicitly compared to VHs'. For example, on one hand the first row of the numbers show that among 74240 pixels which detected as DC in VH im-

Table 6.1.: Truth table to show the degree of agreement between the Algorithm IV and VH classification for *in-vivo* validation.

VH Plaque Component	DC in Proposed Method	FF in Proposed Method	NC in Proposed Method	Total in VH
DC in VH	**54425**	4431	15384	74240
FF in VH	2430	**359326**	19229	380985
NC in VH	10884	37279	**45221**	93384
Total in Proposed Method	67739	401036	79834	**548609**

Table 6.2.: The Results of Algorithm IV as *in-vivo* validation with 120 Images.

	Sensitivity	Specificity	Accuracy
Dense Calcium (DC)	80.1% $\pm$ 0.3	94.5% $\pm$ 0.2	92.8%
Fibro-Lipid (FF)	89.6% $\pm$ 0.09	98.91% $\pm$ 0.03	92.1%
Necrotic Core (NC)	56.6% $\pm$ 0.3	86.8% $\pm$ 0.2	82.4%

ages used in this test collectively, the proposed algorithm classified the 54425 pixels as DC correctly (True Positive for DC), 4431 pixels as FF plus 15384 pixels as NC which are not correct (False Negative for DC). On the other hand, the first column of the numbers shows that among the 67739 pixels which the proposed method classified as DC, excluding the 54425 pixels which are true, 2430 pixels misclassified as FF (False Positive for DC) and 10884 pixels misclassified as NC (False Positive for DC). Analyzing the other rows and columns will determine the similar parameter for FF and NC too.

6.2. Ex-Vivo Validation

In order to test the reliability of the newly proposed algorithm (Algorithm IV), it was decided to validate with two reliable histology datasets considered as *ex-vivo* validation. The first histology samples were processed and prepared as mentioned in 6.2.1.i and 6.2.5.ii by our medical partner group at Cardiology Department in University of Munich [71]. The second one is the dataset used in Katouzian et al. [37]. In addition to histology images, this dataset contains the images reconstructed from the plaque characterization algorithm proposed by Katouzain et al [38].

6.2.1. Dataset 1:

a. Specimen handling and processing

Six human coronary arteries (two left anterior descending arteries; two left circumflex arteries; two right coronary arteries) from 3 cadavers (mean age 70$\pm$9 years, all men, all non-cardiac death) were imaged with IVUS within 12 hours post mortem (mean time: 9$\pm$1 h). After harvesting, the hearts were stored at 9^0C until imaging. The study was approved by the Institutional Ethics Committee of the University of Munich.

b. IVUS Imaging

After cannulation of the ostium of each coronary artery a pressure of 90 mmHg was established using a 0.9% sodium chloride solution. A 0.014-inch guide wire was inserted into the coronary artery lumen under fluoroscopic guidance. An external marker (surgical suture) was applied to the vessel at the distal (first image) and proximal (final image) position of the probe, which later enabled accurate correlation of IVUS and histology images. The IVUS probes were inserted and advanced to distal end of the vessel. An electronic probe (In-Vision Gold, Volcano Therapeutics, Inc., Rancho Cordova, California, USA) with a synthetic aperture 2.9 F and a frequency of 20 MHz was used. A motorized pullback was performed along the entire vessel with a speed of 1.0 mm/s using a dedicated pullback device (R-100 research pullback device, Volcano Therapeutics, Inc.). IVUS images were stored digitally in DICOM format. Immediately after the IVUS imaging, specimens were fixed with the 10% neutral-buffered formalin and histology was performed.

c. Histology

All vessel specimens were dissected from the heart and 5mm blocks were cut starting from the distal marker. Each tissue block was numbered, decalcified in a standard ethylene diamine-tetra-acetic acid-4 Na-20% citric acid solution for 10 hours, and then embedded in paraffin. From each block, at least two consecutive 4 mm thick slices were cut every millimetre using a microtome. All cross-sections were stained with haematoxylin and eosin and every second slice with Elastica-van Gieson. These stains routinely allow for the identification of necrotic-lipid rich, calcium and fibrous tissue. See figure 6.3.b.

d. Manual image analysis

IVUS images were correlated with the corresponding histology slides. All images were divided into four quadrants. Four plaque componentss for tissue characterization of the vessel wall: normal, fibrous-lipid, calcium and necrotic-lipid rich (necrotic) plaques were used. Each of the plaque components was assigned to a different colour: grey for normal, green for fibrous-lipid, white for calcium and red for necrotic tissue. Every part of the vessel wall in the IVUS images within the lumen-intima and media-adventitia borders was classified to consist of one of these tissue types using histology as the gold standard (see figure 6.3.c). For histological classification, a modified grading system in accordance with the Committee on Vascular Lesions of the Council on Atherosclerosis [87] and [93] were used. Normal vessel wall was defined as a regular three-layered appearance without evidence of intimal thickening. In addition, early lesions (corresponding to plaque type I-III [93]) were defined as normal because these early changes are to a certain degree reversible [36] and due to their inferior resolution are not detectable in IVUS. Fibrous plaque was defined as accumulation of predominant fibrous tissue corresponding to plaque type VIII [93]. Necrotic-lipid rich plaque was defined as accumulation of predominant lipid rich necrotic tissue corresponding to plaque type IV [93]. Plaques were defined as calcified when there was evidence of calcium deposits in the tissue corresponding to plaque type VII [93].

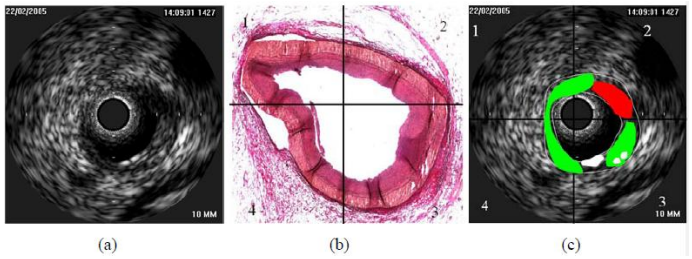

Figure 6.3.: a) IVUS image, b) Histology and c) Manually analysed image.

6.2.2. Results of Ex-Vivo Validation (Dataset 1)

The images used in *ex-vivo* validation were not considered in previous analysis of this research. For *ex-vivo* validation, a SVM classifier was trained using the whole dataset and VH images as labels. Figure 6.4 shows the results of applying the Algorithm IV to two different IVUS images. These results are validated and compared with 10 manually analyzed images considered as reference in this work. Also, table 6.3 shows the statistical results of applying Algorithm IV to these images.

In most similar studies, when one wants to validate with histology images a region-based validation method is used. It means that instead of comparing the result and its corresponding label pixel by pixel, the validation step is done by comparing regions, a window which contains more than one pixel. For example, the size of validation regions in Nair et al [58] is $1/3\ mm \times 1/3\ mm$, i.e. approximately a window of size 13×13 pixels. To handle this, a validation window of size $n \times n$ pixels, where n can vary from one (pixel-based validation) to 13 was defined. The label of a validation window was selected by looking at labels of its constituent pixels. In fact, it is assigned to a plaque component which is the majority. Figure 6.5 shows different accuracies achieved through different window sizes from the pixel-based validation ($0.025\ mm \times 0.025\ mm$ pixels) till the region-based validation ($0.3\ mm \times 0.3\ mm$ regions). This figure shows that the size of regions affects the results.

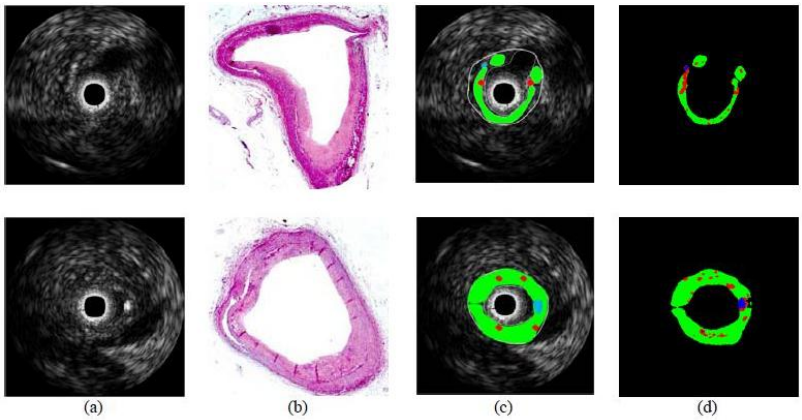

Figure 6.4.: (a) IVUS cross section, (b) Histology image, (c) Manually analyzed image, and (d) Result of algorithm IV.

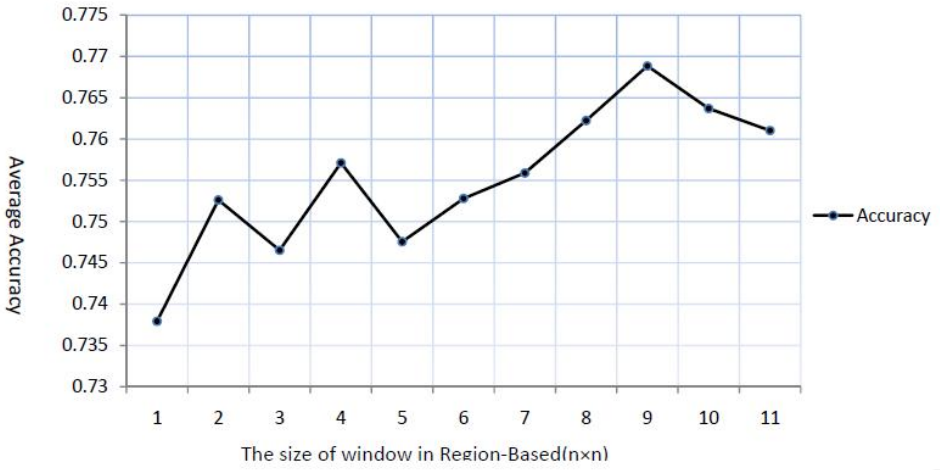

Figure 6.5.: Variable accuracies show the effect of window size in validation against the pixel-based validation (n=1 on x-axis).

Table 6.3.: The Result of ex-vivo validation: Algorithm IV validated with histology pictures using pixel-based and region-based validation (Data set 1).

	DC		**FF**		**NC**		**Overall**
	Sensitivity	Specificity	Sensitivity	Specificity	Sensitivity	Specificity	**Accuracy**
Algorithm IV	55% ± 15	97% ± 2	77% ± 9	50% ± 15	47% ± 9	77% ± 9	74% ± 8
Algorithm IV (9×9)	47% ± 19	98% ± 2	82% ± 8	58% ± 9	38% ± 17	83% ± 8	77% ± 8

6.2.3. Statistical Analysis of Ex-Vivo Validation (Dataset 1)

As mentioned in previous section, data set one in *ex-vivo* validation were validated using both the pixel-based and region-based validation methods. Their sensitivity, specificity, and accuracy for three plaque components are reported separately in tables 6.5 and 6.6. When predicting the tissue types in *ex-vivo* validation, the kappa value for pixel-wised method (kappa = 0.487) was a little less than region-based method (kappa=0.533) but both presenting the moderate agreement.

Table 6.4.: Truth table to show the degree of agreement between the Algorithm IV and histology images of dataset1 for *ex-vivo* validation (Pixel-based).

VH Plaque Component	DC in Proposed Method	FF in Proposed Method	NC in Proposed Method	Total in VH
DC in VH	**1169**	149	654	1972
FF in VH	261	**36908**	4785	41954
NC in VH	812	3815	**5668**	10295
Total in Proposed Method	2242	40872	11107	**54221**

Table 6.5.: Truth table to show the degree of agreement between the Algorithm IV and histology images of dataset1 for *ex-vivo* validation (Region-based:9×9) .

VH Plaque Component	DC in Proposed Method	FF in Proposed Method	NC in Proposed Method	Total in VH
DC in VH	**32**	6	20	58
FF in VH	11	**973**	88	1072
NC in VH	13	85	**131**	229
Total in Proposed Method	56	1064	239	**1359**

6.2.4. Dataset 2

An acquisition of the cross-sectional ultrasound images of right coronary arteries (RCA), left anterior descending (LAD), and left circumflex (LCX) coronary arteries for this dataset were performed with a 40-MHz rotating single-element Boston Scientific (Fremont CA) transducer. The catheter pullback speed was equal to 0.5 mm/s and the frame rate was 30 frames/s. Each raw frame contains 256 lines with 2048 samples per line. In order to construct a 256×256-pixel IVUS image, the envelope of each RF signal was computed by the corresponding analytical signal and then it was decimated by eight samples. A logarithmic compression was also used to enhance the image quality. Then, the 8-bit quantization was used, and the resulting gray-scale image transformed to Cartesian coordinates to generate a typical IVUS frame (figure 6.7.a). For extraction histology images, arteries of human hearts obtained from two sources, i.e. autopsy and transplant surgery, are dissected from the heart and oriented in a tissue cage fixture (figure 6.6). Then, they are stained with Movat Pentachrome. Movat Pentachrome colors cytoplasm in red, elastic fibers in black, collagen and reticulum fibers in yellow to greenish, and proteoglycans in blue. Then pictures are taken from these sections and homogenous parts are marked by pathologists (figure 6.7.b). Then these marked images are mapped on IVUS images (figure 6.7.c) and tissue color map images are extracted (figure 6.7.d).

Table 6.6.: The Result of *ex-vivo* validation: Algorithm IV validated with histology pictures (Data set 1). The parameter ± confidence Interval is shown for the Sensitivity, Specificity and Accuracy parameters.

	Sensitivity		Specificity		Accuracy	
	Pixel wised	Region based	Pixel wised	Region based	Pixel wised	Region based
Dense Calcium (DC)	59.3% ± 2.2	55.2% ± 13	97.5% ± 0.6	98% ± 3.4	96%	96%
Fibro-Lipid (FF)	87.9% ± 0.31	90.8% ± 1.7	67.7% ± 0.45	68.3% ± 2.8	85.4%	86%
Necrotic Core (NC)	55.1% ± 0.1	57.2% ± 6.4	87.6% ± 0.7	90.4% ± 3.8	79.9%	85%

Figure 6.6.: Tissue cage fixture: The artery is fixed in the cage and an automatic pullback is performed in saline and human blood. The histology sections are taken at every 2 mm using side rods after the artery was fixed by formaldehyde [38].

6.2.5. Results of Ex-Vivo Validation (Dataset 2)

In the dataset two, which was used for ex-vivo validation, a SVM classifier was trained using 50 tissue color map images extracted through histology pictures as shown in figure 6.7.d (i.e. manually painted image based on histology image by expert pathologist).

Figure 6.8.c shows the results of applying the Algorithm IV to four different gray-scale IVUS images. These results were validated with other tissue color map images which were not included in training dataset.

6.2.6. Statistical Analysis of Ex-Vivo Validation (Dataset 2)

Kappa value 0.454 for this *ex-vivo* validation indicates the moderate agreement between algorithm IV and histology images in table 6.7 as gold standard. Furthermore kappa value 0.628 for comparing the result of algorithm IV with histology images shown in table 6.8 indicates the good agreement. Table 6.10 shows a comparison of *In-Vivo* and *Ex-Vivo* validation methods in this chapter.

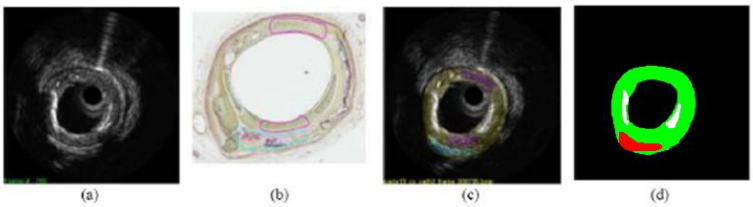

Figure 6.7.: (a): IVUS cross section, (b): Movat Histology image, (c) tissue color map imposed on the IVUS image, and (d) tissue color map: White is DC, green is fibro-lipid and red is NC [38].

6.3. Longitudinal Resolution Enhancement (LRE)

As mentioned before, one of the limitations of VH is its ECG gated acquisition. Using the ECG gated acquisition, in one cardiac cycle, the RF spectrum from only one IVUS frame with the synchronization of R-wave is acquired and analyzed. Therefore the distance between each VH images can be derived from the R-R interval (s) and the pullback speed of the IVUS catheter (mm/s) as follows [60]:

$$Distance\ \ between\ \ two\ \ VH\ \ \ images(mm) = R - R\ \ interval \times Pullback\ \ speed \quad (6.1)$$

At the same time, gray-scale IVUS images are, normally, produced at a rate of $30 frames/sec$. Therefore, comparing to gray-scale IVUS, the longitudinal resolution for VH is highly reduced. Considering a heart rate of 60 $beats/min$ and pullback speed of 1 mm/sec, for example, RF analysis is performed for only $1 frame/mm$ ($1 frame/s$). However, using the proposed algorithms of Image Based Histology (IBH), the longitudinal resolution would increase up to $30 frames/mm$ (figure 6.9).

In order to envisage the longitudinal resolution enhancement, plaque characterization based on the proposed algorithms were implemented on IVUS frames between each two consequential VH images. Plaque component abundances, which contribute to each tissue type characterized by the proposed method, are displayed in three different charts in figures 6.10 to 6.12.

The points in each chart refer to the plaque component abundances in VH images. The ones of other IVUS frames between two sequential VH frames are computed using the proposed method and displayed by lines. The large changes in plaque component abundances between two VH -IVUS frames is reasonable, since they can be related to different sections of the vessel of about 1 mm distance. However, the rapid changes between two points on the line, which is described and highlighted using an IVUS and its corresponding characterized image, are because of existing different plaque components which were ignored by using VH. Moreover, one should note that these variations might be resulted from differences in the detected plaque area as well.

In order to have a better imagination of plaque structures, a 3D view of plaques was created. Figure 6.13 show the 3D view of Dense Calcium, Necrotic Core and Fibro-Fatty reconstructed from VH images and IBH images.

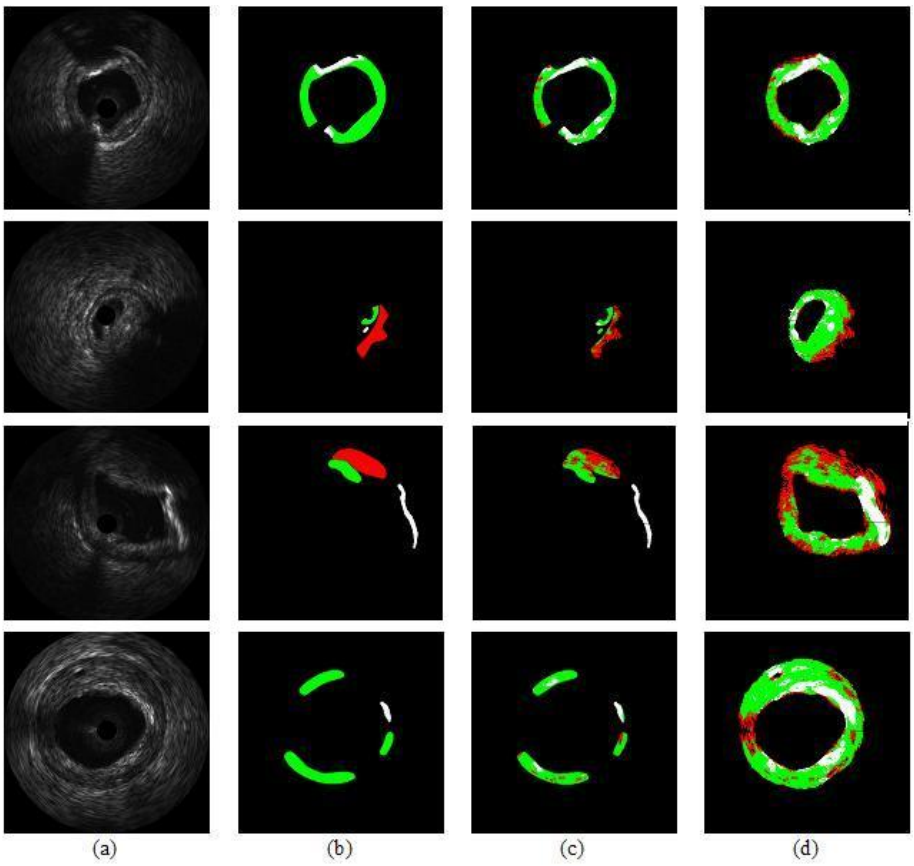

Figure 6.8.: (a) Gray-scale IVUS image, (b) Manually painted image based on Histology image with Fibrotic+Fibrofatty (green), Calcium (white), and Necrotic (red) components, (c) Characterized image using Algorithm IV after training by (b) on the manually detected plaque area, and (d) Characterized image using Algorithm IV after training by (b) on the whole plaque area detected by expert.

Table 6.7.: Truth table to show the degree of agreement between the Algorithm IV and histology images of dataset 2 for *ex-vivo* validation (Pixel-based).

VH Plaque Component	DC in Proposed Method	FF in Proposed Method	NC in Proposed Method	Total in VH
DC in VH	**5503**	4710	40	10253
FF in VH	2760	**26776**	1629	31165
NC in VH	142	2040	**2208**	4390
Total in Proposed Method	8405	33526	3877	**45808**

Table 6.8.: Truth table to show the degree of agreement between the Algorithm IV and histology images of dataset 2 for *ex-vivo* validation (Region-based).

VH Plaque Component	DC in Proposed Method	FF in Proposed Method	NC in Proposed Method	Total in VH
DC in VH	**136**	85	0	221
FF in VH	23	**844**	26	893
NC in VH	1	39	**61**	101
Total in Proposed Method	160	968	87	**1215**

Table 6.9.: The Result of *ex-vivo* validation: Algorithm IV validated with histology pictures (Data set 2). The parameter $\pm$ confidence Interval is shown for the Sensitivity, Specificity and Accuracy parameters.

	Sensitivity		Specificity		Accuracy	
	Pixel wised	Region based	Pixel wised	Region based	Pixel wised	Region based
Dense Calcium (DC)	65.5% $\pm$ 1	85% $\pm$ 5.5	87.3% $\pm$ 0.7	92% $\pm$ 4.2	83.3%	91%
Fibro-Lipid (FF)	79.9% $\pm$ 0.4	87% $\pm$ 2	64.3% $\pm$ 0.5	80% $\pm$ 2.5	75.7%	86%
Necrotic Core (NC)	56.9% $\pm$ 1.6	70% $\pm$ 9.6	94.8% $\pm$ 0.7	96.54% $\pm$ 3.9	91.6%	95%

Table 6.10.: Summary of applied validation methods (*In-Vivo* and *Ex-Vivo*).

Validation	Data Sets	Pixel-based		Region-based	
		Accuracy	Kappa	Accuracy	Kappa
In vivo	120 IVUS Images	>82 %	0.639	-	-
Ex vivo	Data Set #1	>79 %	0.487	>85 %	0.533
	Data Set #2	>75 %	0.454	>86 %	0.628

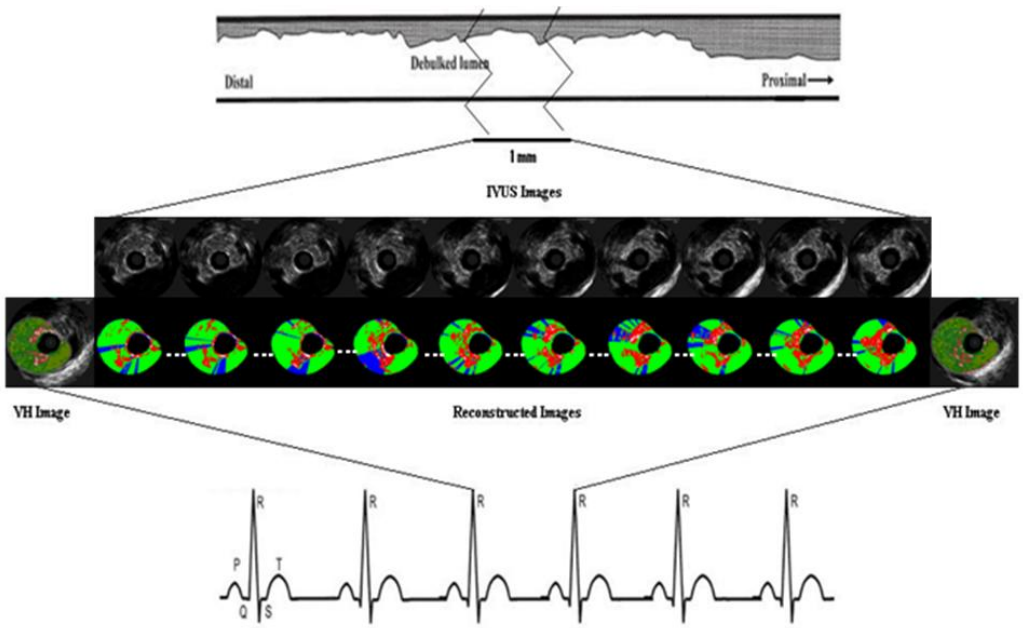

Figure 6.9.: Illustration of enhancement of the longitudinal resolution of atherosclerosis plaque composition characterization of gray scale IVUS using IVUS-IBH method compared to VH. Gray-scale IVUS images are, normally, produced at a rate of $30 frame/sec$. Considering a heart rate of 60 $beats/min$ and pullback speed of $1 mm/sec$, for example, RF analysis is performed for only one $frame/millimeter$ (or $1 frame/s$). Therefore VH has a much lower longitudinal resolution than gray-scale IVUS.

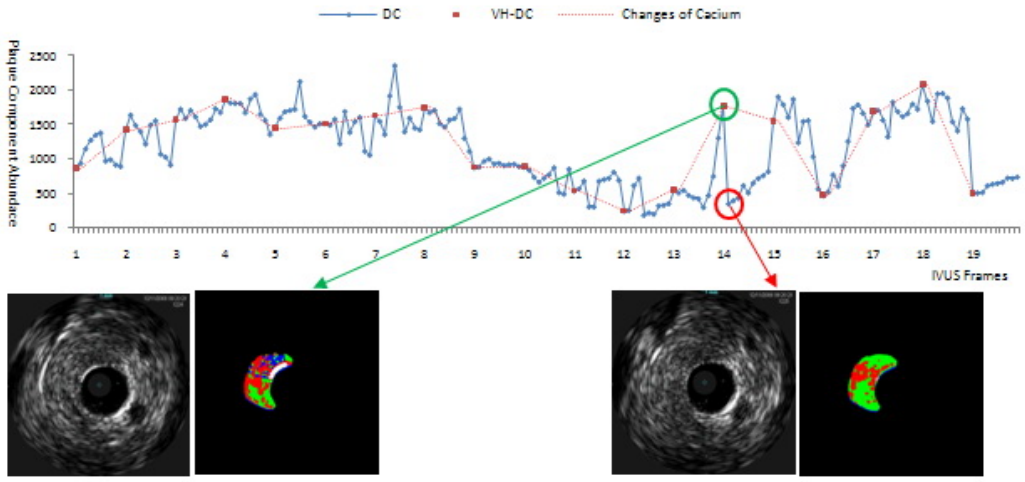

Figure 6.10.: Illustration of Calcium plaque changes between VH slides.

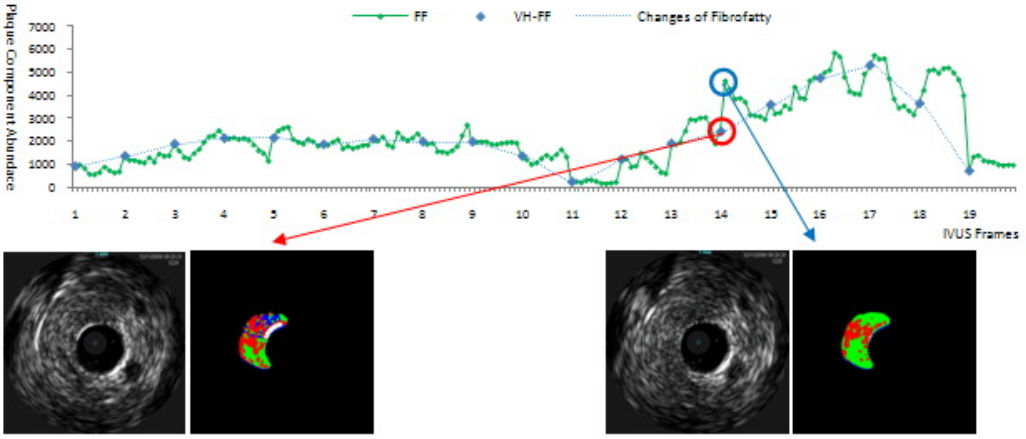

Figure 6.11.: Illustration of Fibro-Fatty plaque changes between VH slides.

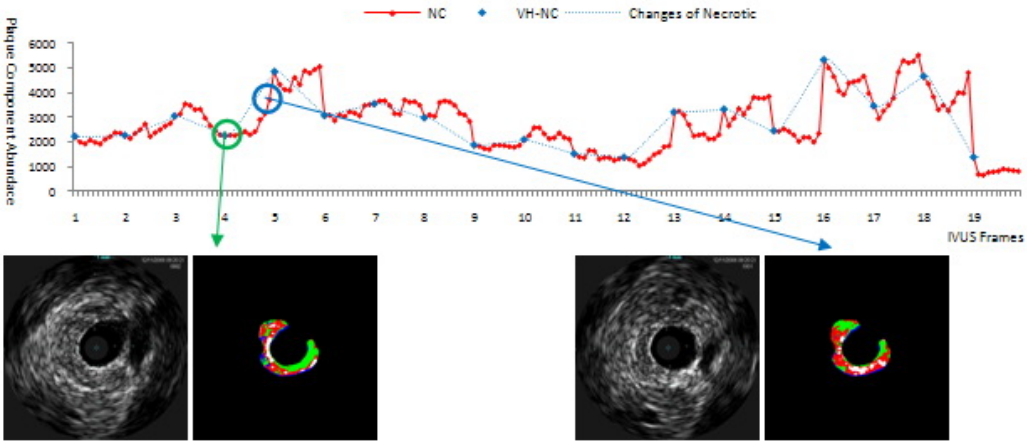

Figure 6.12.: Illustration of Necrotic plaque changes between VH slides.

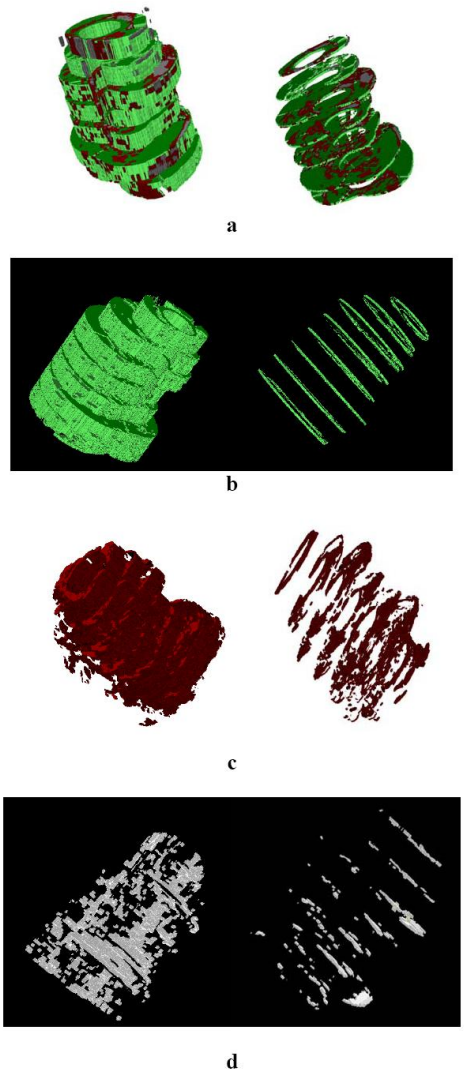

Figure 6.13.: The three-dimensional (3D) view of both the vessel and the distribution of different plaque components in the plaque area before and after IBH proposed algorithm that highlight longitudinal resolution enhancement a)All plaque components b)Dense Calcium c)Fibro-Fatty d)Necrotic Core.

7. Chapter Seven: Discussion and Conclusion

This chapter summarizes the achievements made in the dissertation, followed by a discussion of current problems and a presentation of ideas for future work to further advance the IVUS plaque characterization solution.

7.1. Summary

This work introduces the use of classical pattern recognition and image processing (especially texture analysis) tools to characterize plaque components in IVUS images. A new framework for near-real time automatic IVUS structure analysis and tissue characterization to improve longitudinal resolution of plaque component analysis is designed in this work. The following summarizes the main contribution of each part of the work described in this document:

In Chapter 1, biological concerns of this project were investigated. In that chapter, it is stated how IVUS images would help physicians to assess coronary diseases and what kind of information these images would provide. Also in this chapter different plaque components were introduced and the capability of IVUS images for identifying vulnerable plaques were compared to the capability of other image modalities in practice. VH, a technique based on backscatter RF signal analysis, that provides color-coded tissue map of plaque composition superimposed IVUS images were introduced and its applications were discussed. At the end of chapter 1 current problems with IVUS images were highlighted and the overall strategy to solve parts of these problems was noted.

In order to assess more accurately the IVUS images, principals of IVUS images were introduced in Chapter 2. Physics of ultrasound, IVUS image formation and problems with IVUS image acquisition (mainly artifacts) were points mentioned in Chapter 2.

Chapter 3 was about the border detection in IVUS images as the primary meanwhile important stage for plaque characterization. In that chapter the previous methods for IVUS border detection were introduced and the shortcomings of each discussed. Then the proposed method for border detection was presented and evaluated with several common metrics.

In Chapter 4, the state-of-the-arts on plaque characterization in IVUS images were presented. RF-based and Image-based approaches to plaque characterization problem were discussed and new methods based on each approach were introduced. Also it was mentioned that each of these approaches has its own advantages and disadvantages.

In Chapter 5, the main steps of the strategy for plaque characterization i.e. polar transformation, shadow detection, feature extraction and classificationfor were introduced. Moreover, basic materials for each step were introduced. Finally four algorithms were proposed. In algorithm I, by using wavelet transform and AR model, some new features were

extracted from run-length matrix of 11×11 sweeping windows. Plaque characterization was then done using SVM classification and post-processing. In algorithm II, 11 run-length (RL) features were extracted from significant subsets of the redundant wavelet decomposition of IVUS images and the classification and post processing methods were the same as algorithm I. Results showed the effectiveness of the RL features in comparison to the co-occurrence and the LBP methods in terms of both time efficiency and classification accuracy. However, one of the limitations of RL features are their sensitivity to the artifacts especially the speckle noise since these artifacts tend to change the composition of the RL matrices by breaking potentially long runs into shorter runs, or by introducing runs with abnormal intensities.

Experiences of the two previous algorithms showed that shadow regions of IVUS images should not be processed like other regions. Applying texture analysis method accustomed to normal parts of the IVUS image to shadow parts may result in misclassification because gray-levels are diminished in shadow regions and textures are altered. Thereby, in algorithm III, the shadow regions were removed before plaque characterization. The features were classical LBP and RL features and plaque characterization was done using SVM classification and post-processing. Shadow detection improved the distinction of three plaque components especially separation of dense calcium from necrotic core. Sensitivity and specificity of DC and NC nearly 5% improved that can highlight influence of shadow detection on the clinical analysis and possible decisions. Also, a Graphic User Interface (GUI) was designed as an effective image processing tool for IVUS-Image Based Histology (IBH) which enables cardiologists with complete IVUS image processing from border detection to plaque characterization. It also provides some additional information including "Clinical Reports" related to the progress of disease such as Eccentricity,% Plaque Area, % Area Stenosis, Plaque Cross Sectional Area (CSA) and portion of each atherosclerosis plaque component with respect to the plaque area in each IVUS cross section.

Owing to different discrimination properties of feature extraction methods compared in the last three algorithms, in algorithm IV, these methods were combined to check the effect of feature combination. Also stated the gray-level information in the form of 9 features instead of applying unreliable post-processing stage. Moreover, in this algorithm, the performance of feature reduction was investigated in reducing the complexity of feature space while not decreasing the accuracy. The impact of classifiers for plaque characterization comparing SVM classifier to ECOC classifier was also analyzed.

In chapter 6, *In-vivo* and *ex-vivo* validation procedures were used, where the results proved the efficiency of algorithm IV for vessel plaque characterization via IVUS images. For in-vivo validation, new IVUS images which were not included in the classification neither as training data nor as test data, were considered to be characterized using algorithm IV. *Ex-vivo* validation was applied by using a different histology datasets to test the reliability of the algorithm IV. Achieving an accuracy of 71% for pixel-based validation and accuracy of 86% for region-based validation shows the robustness of algorithm IV.

At the end of Chapter 6, it was explained how the proposed algorithms enhance the longitudinal resolution of plaque composition analysis. The present VH-derived plaque composition analysis provides only ECG triggered images. That means in an imaging procedure with the rate of 30 frames/s just one IVUS frame out of approximately 30 IVUS frames is considered to generate the color-coded VH image. It can be concluded that in a typical VH imaging procedure about 96% of data will be discarded. The results showed

that different plaque types may have large variations between two consequent ECG-gated IVUS images that are not detectable by just VH images. However, by adding 29 more plaque images, the proposed algorithms help to have better understanding of plaque violations. Increasing the longitudinal resolution becomes more interesting when one tends to have a 3D view of both the vessel and the distribution of different plaque components in the plaque area. In 3D view, the location and distribution of different plaque components of the atherosclerosis is more understandable for cardiologists and furthermore, additional parameters such as "Clinical Reports" together with the percentage of different plaque components can be derived more precisely.

7.2. Discussion and Future Works

In each algorithm, new features and new methods for plaque characterization and compared them with previous methods were proposed. Furthermore, in each algorithm,the shortcomings of the previous algorithms were removed. The overall accuracy of 77 % and kappa 0.62 shows the power of our algorithms and their improvement to previously proposed methods. From the results, it was realized that the necrotic core is hard to detect and increment in overall accuracy depends more on better recognition of this plaque component. It is worth mentioning that accuracy, sensitivity and specificity values are changed by different validation methods. For instance, the region-based validation (0.3 $mm \times 0.3mm$ regions) yielded better results than pixel-based validation (0.025 $mm \times 0.025mm$ pixels). The size of regions affects the results. Comparing reconstructed images to VH images showed that the proposed texture based algorithms produce similar images and have a modest correlation to VH-IVUS, suggesting that most of the information in VH-IVUS tissue characterization comes from the intensity of the ultrasound signal, and less-so on the underlying radio-frequency data. However, it should be taken into account that the texture of tissue in IVUS images is very different with different frequencies, different transducer bandwidths and different transducer geometries. It may also be different between phased array and mechanically rotating transducers, especially with non-uniform rotational distortion comes into play. Achieving the same results with different classifiers (SVM and ECOC) and also after applying feature reduction method (LDA) confirms that these are the best results achievable with these features and higher accuracies demand overcoming the shortcomings that some of them mentioned in the previous paragraphs. Furthermore, VH-IVUS has still limitations to be considered as the gold standard. VH-IVUS is available clinically, and the use of VH-IVUS for observational research studies, such as natural history studies, is appropriate, but there is no data to suggest that VH-IVUS should be used to change clinical treatment. Therefore, in order to check the reliability of this work, in *ex-vivo* validation section, the results of the proposed algorithms were compared to two different databases containing histology images. Achieving almost the same results reveals the power of the algorithms. In order to enhance the proposed methods, the following future works are suggested:

1. Trying to separate fibrous parts from fibro-fatty parts to have the typical 4 plaque map like VH images that is more tangible for physicians.

2. Studying the shadow regions separately to characterize the plaque components in

those regions in order to have a complete view of plaque components in IVUS cross sections.

3. Trying to merge RF-based and image-based methods to benefit the advantages of both and compensate the shortcomings of each.

4. Assessing sequential IVUS cross sections in order to correct the misclassified pixels and have a 3D view of the plaque in coronary vessel.

5. Trying to identify stents and thrombus that are clinically important.

Appendix

A. List of Publications

1. Arash Taki, Holger Hetterich, Alireza Roodaki, S.Kamaledin Setarehdan, Gozde Unal, Johannes Rieber, Nassir Navab and Andreas König, *A new approach for improving coronary plaque component,analysis based on intravascular ultrasound images*, Accepted in International Journal of Ultrasound in Medicine and Biology(March 2010).

2. Arash Taki, Mohamad Maadani, S.Kamledin Setarehdan, Alireza Roodaki, H.Reza Sanaati and Nassir Navab, *Detection of atherosclerotic plaque composition using intravascular images* , Iranian Heart Journal, Volume 10, No.3(Fall 2009).

3. Arash Taki, Oliver Pauly, S.Kamaledin Setarehdan, Gozde Unal and Nassir Navab, *IVUS-based histology of atherosclerotic plaques: improving longitudinal resolution*, SPIE Medical Imaging, San Diego, California, USA, 13-18 February 2010.

4. Arash Taki, Ali Bigdelou, Alireza Roodaki, S.Kamaledin Setarehdan, Gozde Unal and Nassir Navab, *A new tool for automated border detection and characterization of atherosclerotic plaque Composition in IVUS Images*, Computers in Cardiology (CinC 2009), Park City, Utah, September 13-16, 2009.

5. Arash Taki, Alireza Roodaki, Oliver Pauly, S.Kamaledin Setarehdan, Gozde Unal and Nassir Navab, *A new method for characterization of coronary plaque composition via IVUS images*, IEEE International Symposium on Biomedical Imaging: From Nano to Macro (ISBI 2009), Boston, Massachusetts, USA, June 28 - July 1, 2009.

6. Arash Taki, Sara Avansari, Alireza Roodaki, S.Kamaledin Setarehdan and Nassir Navab, *Developing new tool for automatic analysis of IVUS images: from border detection to plaque characterization*, International Journal of Computer Assisted Radiology and Surgery, Volume 4, June 2009.

7. Alireza Roodaki, Arash Taki, S.Kamaledin Setarehdan and Nassir Navab, *Modified wavelet transform features for Characterizing different plaque types in IVUS images; A feasibility study* , 9^{th} International Conference on Signal Processing (ICSP08) Oct. 26-29, 2008, Beijing, China.

8. Arash Taki, Zahra Najafi, Alireza Roodaki, S.Kamaledin Setarehdan, Reza zoroofi, Andreas König and Nassir Navab, *Automatic segmentation of calcified plaques and vessel borders in IVUS images*, International Journal of Computer Assisted Radiology and Surgery(2008) 3:347-354, September 2008.

9. Arash Taki, Alireza Roodaki, S.Kamaledin Setarehdan, Petr Heider and Nassir Navab, *Assessment of Automatic Classification of Artery Plaque Composition in IVUS Images Using Histology Correlation*, 22^{nd} International Congress and Exhibition June 25-28, 2008, Barcelona, Spain.

10. Alireza Roodaki, Zahra Najafi, Amin Soltanzadi, Arash Taki, S.Kamaledin Setarehdan and Nassir Navab, *Detection of Outer Layer of the Vessel Wall and Characterization of Calcified Plaques in IVUS Images*, 13^{th} Int'l CSI Computer Conference, CSICC08, Kish Island, Iran, March 2008.

11. Zahra Najafi, Arash Taki, S.Kamaledin Setarehdan, Reza Zoroofi, Andreas Konig and Nassir Navab, *A new method for automatic border detection in IVUS images and 3D visualization of segmented frames*, The 4^{th} Visual Information Engineering 2007 Conference: VIE 2007, London, July 2007.

12. Arash Taki, Zahra Najafi, S.Kamaledin Setarehdan, Reza Zoroofi and Nassir Navab, *A new automatic border detection method for lumen and mediaadventitia boundaries in IVUS images*, June, 2007, Proceedings of 21st International Congress of Computer Assisted Radiology and Surgery (CARS 2007), Berlin, Germany.

13. Amin Soltanzadi, Zahra Najafi, Alireza Roodaki, Arash Taki, S. Kamaledin Setarehdan, Reza Zoroofi and Nassir Navab, *Full Automatic Border Extraction of Coronary Arteries in IVUS Images Using Deformable Models*, 14^{th} Conference on Medical Engineering, Tehran-Iran, Dec. 2007.

B. List of Abbreviations

ACC. Anisotropic Contour Closing
ACS. Acute Coronary Syndrome
AD. Average Distance
AIC. Akaike's Information Criterion
AMI. Myocardial Infarction
AR. Autoregressive
ARMA. Autoregressive Moving Average
AUC. Area Under Curve
BWS. Black-White Symmetry
CAD. Coronary Artery Disease
CI. Confidence interval
CL. Component labeling
CSA. Cross-Sectional Area
CT. Computed Tomography
DC. Dense Calcium
DD. Degree of Direction
DP. Dynamic Programming
DWPF. Discrete wavelet Packet Frame
DWT. Discrete Wavelet Transform
EBCT. Electron Beam Computed Tomography
ECG. Electro Cardio Gram
ECOC. Error-Correcting Output Codes
EEM. External Elastic Membrane
FF. Fibro-Fatty
FPE. Final Prediction Error
FT. Fibrous Tissue
GS. Geometric Symmetry
GUI. Graphical User Interface
HD. Hausdorff Distance
HT. Hilbert Transform
IBH. Image Based Histology
IVUS. Intravascular Ultrasound
k-NN. k-Nearest Neighbors
LAD. Left Anterior Descending
LBP. Local Binary Pattern
LCX. Left Circumflex
LDA. Linear Discriminant Analysis
LDB. Local Discreminant Basis
MA. Media-Adventia

MBF. Mid-Band Fit
MHM . Modified Hu Moments
MI. Myocardial Infarction
MIDL. Minimum Description Length
MLD. Minimum Lumen Diameter
MRI. Magnetic Resonance Imaging
MSE. Mean Square Error
NC. Necrotic Core
NGL. Neighboring Gray Level
NGTDM. Neighborhood Gray-Tone Difference Matrix Method
NMR. Nuclear Magnetic Resonance
NSD. Normalized Standard Deviation
NURD. Non-Uniform Rotational Distortion
OCT. Optical Coherence Tomography
PCI. Percutaneous Coronary Intervention
PDF. Probability Density Function
PH. Prognosis Histology
POI. Pixel of Interest
PSF. Point Spread Function
RAD. Restricted Anisotropic Diffusion
RBF. Radial Basis Function
RCA. Right Coronary Artery
RF. Radio Frequency
ROC. Receiver-Operating-Characteristic
RWPT. Redundant wavelet packet transform
RWT. Redundant wavelet transform
SNR. Signal-to-Noise Radio
SVM. Support Vector Machine
TCFA. Thin Cap Fibroatheroma
TGC. Time Gain Compensation
TU. Texture Unit
UCT. Ultrafast Computed Tomography
VH. Virtual Histology
VP. Vulnerable Plaque
WI. William Index
WPT. Wavelet Packet Transform
WS. Watershed segmentation
WT. Wavelet Transform

C. Quantitative Analysis for Clinical Reports of IVUS Imaging

Basic quantitative analysis of IVUS images can be performed using the GUI which was introduced in Algorithm III described in Chapter 5. Cross sectional area (CSA) can be traced for both the lumen and media-adventitia borders and thus facilitates a calculation of percent plaque area. The measurements of minimum and maximum diameters of lumen and of minimum and maximum thicknesses of plaque area are calculated. Plaque thickness can also be estimated as the difference between the vessel and lumen CSAs and plaque eccentricity can be derived in a number of ways. (see figure C.1).

$$Eccenricity = \frac{Maximum\ plaque\ thickness}{Minimum\ plaque\ thickness} \tag{C.1}$$

$$\%\ Area\ stenosis = \frac{Reference\ lumen\ CSA\ -\ Lesion\ lumen\ CSA}{Reference\ lumen\ CSA} \tag{C.2}$$

$$\%\ Plaque\ area = \frac{Plaque\ CSA}{MA\ CSA} \quad and \quad Plaque\ CSA = MA\ CSA\ -\ Lumen\ CSA \tag{C.3}$$

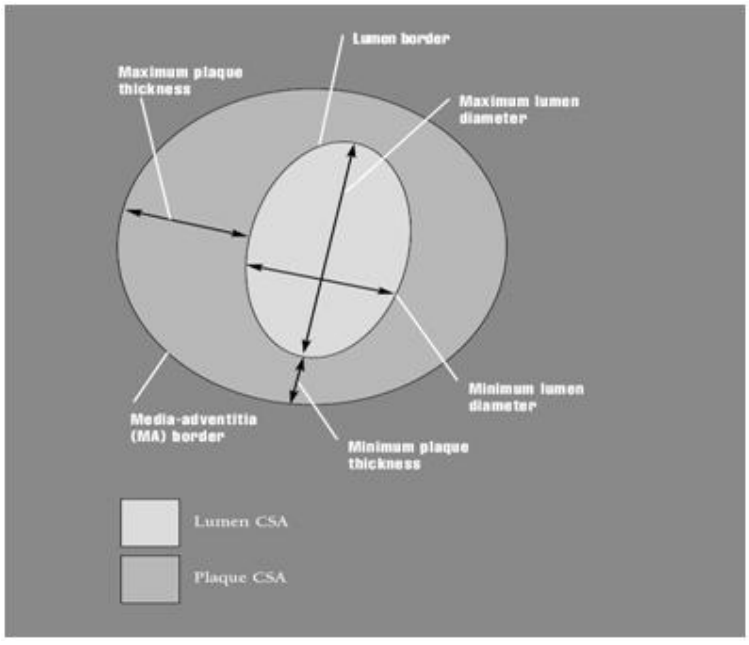

Figure C.1.: Parameters and measures required for analysis of IVUS images[14].

Bibliography

[1] P. Agostoni, J.A. Schaar, and P.W. Serruys. The challenge of vulnerable plaque detection in the cardiac catheterization laboratory. *Cardiovascular Medicine*, 7:349–358, 2004.

[2] J.A. Ambrose, S.L. Winters, R.R. Arora, A. Eng, A. Riccio, R. Gorlin, and V. Fuster. Angiographic evolution of coronary artery morphology in unstable angina. *The American Journal of Cardiology*, 7:472–478, 1986.

[3] C.M. Bishop. *Pattern Recognition and Matchine Learning*. Springer Science, 1st edition, 2006.

[4] E.G.P. Bovenkamp, J. Dijkstra, J.G. Bosch, and J.H.C. Reiber. Multi agent segmentation of ivus images. *The Journal of the Pattern Recognition Society*, 37(4):647–663, 2004.

[5] P.A. Brathwaite, K.B. Chandran, D.D. McPherson, and E.L. Dove. Lumen detection in human ivus images using region-growing. *Computers in Cardiology*, pages 37–40, 1996.

[6] M.E. Brezinski. Optical coherence tomography for identifying unstable coronary plaque. *International Journal of Cardiology*, 107:154–165, 2006.

[7] S.L. Bridal, P. Fornes, P. Bruneval, and G. Berger. Parametric (integrated backscatter and attenuation) images constructed using backscattered radio frequency signals (25-56 mhz) from human aortae in vitro. *Ultrasound in medicine biology*, 23:215–229, 1997.

[8] N. Bruining, C. Von Birgelen, F. Prati, M.T. Mallus, W. Li, W. Den Hoed, M. Patijn, P.J. De Feyter, P.W. Serruys, and J.R.T.C Roelandt. Dynamic three dimensional reconstruction of icus images based on an ecg gated pull back device. *Computers in Cardiology*, pages 633–636, 2000.

[9] N. Bruining, S. Verheye, M. Knaapen, P. Somers, J.R.T.C. Roelandt, E. Regar, I. Heller, S. De Winter, J. Ligthart, G.Van Langenhove, P.J. De Feijter, P.W. Serruys, and R. Hamers. Three-dimensional and quantitative analysis of atherosclerotic plaque composition by automated differential echogenicity. *Catheterization and Cardiovascular Interventions*, 70(7):968–978, 2007.

[10] E. Brusseau, C.L. de Korte, F. Mastik, J. Schaar, and A.F.W. van der Steen. Fully automatic luminal contour segmentation in intracoronary ultrasound imaging: a statistical approach. *IEEE Transactions on Medical Imaging*, 23(5):554–566, 2004.

[11] K.L. Caballero, J. Barajas, O. Pujol, N. Savatella, and P. Radeva. In vivo ivus tissue classification: a comparison between rf signal analysis and reconstructed images. *Iberoamerican Congress on Pattern Recognition(CIARP)*, 4225:137–146, 2006.

[12] M.H.R. Cardinal, J. Meunier, G. Soulez, R.L. Maurice, E. Therasse, and G. Cloutier. Intravascular ultrasound image segmentation: A three-dimensional fast-marching method based on gray level distributions. *IEEE Transactions on Medical Imaging*, 25(5), 2006.

[13] C. Chang and C. Lin. Libsvm:a library for support vector machines. *Software available at http://www.csie.ntu.edu.tw/ cjlin/libsvm*, 2001.

[14] D. Charles, SH. Liberty, W. Anderson, and N.G. Vincent. *The ABCs of IVUS*. Boston Scientific, 2001.

[15] D. Cheeke, J.D. Cheeke, and C.N. Cheeke. *Fundamentals and applications of ultrasonic waves*. CRC PRESS, 1st edition, 2002.

[16] R.R. Coifman and M.V. Wickerhauser. Entropy based algorithm for best basis selection. *IEEE Transactions on Information Theory*, 38(2):713–718, 1992.

[17] M.J. Davies, W.F. Fulton, and W.B. Robertson. The relation of coronary thrombosis to ischaemic myocardial necrosis. *Journal of Pathology*, (127):99–110, 1979.

[18] P.J. Dhawale, N. Griffin, D.L. Wilson, and J.M. Hodgson. Calibrated 3-d reconstruction of intracoronary ultrasound images with cardiac gating and catheter motion compensation. *Computers in Cardiology Proceeding*, pages 31–34, 1992.

[19] J. Dijkstra, G. Koning, and J.H.C. Reiber. Quantitative measurements in ivus images. *International Journal of Cardiac Imaging*, 15:513–522, 1999.

[20] B.H. Romeny E.J.L. Brunenberg, O. Pujol and P. Radeva. Automatic ivus segmentation using feature extraction and snakes. *Medical Image Computing and Computer-Assisted Intervention(MICCAI)*, 41-91, 2006.

[21] S. Escalera, O. Pujol, J. Mauri, and P. Radeva. Intravascular ultrasound tissue characterization with sub-class error-correcting output codes. *Journal of Signal Processing Systems*, 55(1-3):35–47, 2009.

[22] E. Falk and A. Fernandez-Ortiz. Role of thrombosis in atherosclerosis and its complications. *The American Journal of Cardiology*, 75:3B–11B, 1995.

[23] L. Fan, D.M. Herrington, and P. Santago. 3d ultrasound image segmentation using multiple incomplete feature sets. *Proceedings of the SPIE- The International Society for Optical Engineering*, 3661:948–956, 1999.

[24] R.E. Fan, P.H. Chen, and C.J. Lin. Working set selection using the second order information for training support vector machine. *Machine Learning Research*, pages 1889–1918, 2005.

[25] S. Fu, Q. Ruan, W. Wang, and Y. Li. Feature preserving nonlinear diffusion for ultrasonic image denoising and edge enhancement. *Transaction on engineering, computing and technology*, pages 1305–1313, 2004.

[26] M.M. Galloway. Texture analysis using gray level run lengths. *Journal of Computer Graphics and Image Processing*, 4:172–179, 1975.

[27] D. Gil, A. Hernandez, O. Rodriguez, J. Mauri, and P. Radeva. Statistical strategy for anisotropic adventitia modelling in ivus. *IEEE Transaction on Medical Imaging*, 25(6):768–778, 2006.

[28] D. Gil, P. Radeva, J. Saludes, and J. Mauri. Segmentation of artery wall in coronary ivus images: A probabilistic approach. *Computers in Cardiology*, pages 687–690, 2000.

[29] R. Gil, C.V. Birgelen, F. Prati, C.D. Mario, J. Ligthart, and P.W. Serruys. Usefulness of three dimensional reconstruction for interpretation and quantitative analysis of intracoronary ultrasound during stent deployment. *The American Journal of Cardiology*, 77(9):761–764, 1996.

[30] N. Gonzalo, H.M. Garcia-Garcia, J. Ligthart, G. Rodriguez-Granillo, E. Meliga, Y. Onuma, J.C.H. Schuurbiers, N. Bruining, and P.W. Serruys. Coronary plaque composition as assessed by grayscale ultrasound and radiofrequency spectral data analysis. *International Journal of Cardiovascular Imaging*, 24:811–818, 2008.

[31] M.B. Hansen, J. Moller, and F.A. Togersen. Bayesian contour detection in a time series of ultrasound images through dynamic deformable template models. *IEEE Transactions on Image Processing*, 3(2):213–228, 2002.

[32] R. Haralick, K. Shanmugam, and I. Dinstein. Textural features of image classification. *IEEE Trans Syst Man Cyber*, 6:610–621, 1973.

[33] A. Hernandez, D. Gil, and P. Radeva. On the usefulness of supervised learning for vessel border detection in intravascular imaging. *Frontiers in Artificial Intelligence and Applications*, 131:67–74, 2005.

[34] A.H. Hernandez, D.G. Gil1, P.R. Radeva1, and E.N. Nofrerias. Anisotropic processing of image structures for adventitia detection in intravascular ultrasound images. *Computers in Cardiology*, pages 229–232, 2004.

[35] H. Hoff, A. Korbijn, T.H. Smith, J.F. Klinkhamer, and N. Bom. Imaging artifacts in mechanically driven ultrasound catheters. *International Journal of Cardiac Imaging*, 4:195–199, 1989.

[36] M. Kass, A. Witkin, and D. Terzopoulos. Snakes: Active contour models. *International Journal of Computer Vision*, 1(4):321–331, 1987.

[37] A. Katouzian, B. Baseri, E.E. Konofagou, and A.F. Laine. An alternative approach to spectrum-based atherosclerotic plaque characterization techniques using intravascular ultrasound (ivus) backscattered signals. *2nd Workshop on Computer Vision for Intravascular and Intracardiac Imaging, MICCAI.*, 2008.

[38] A. Katouzian, S. Sathyanarayana, B. Baseri, E.E. Konofagou, and G. Carlier. Challenges in atherosclerotic plaque characterization with intravascular ultrasound (ivus): from data collection to classification. *IEEE Transactions on Information Technology in Biomedicine*, 12(3):315–327, 2008.

[39] P. Kearney and R. Erbel. Imaging in the characterization laboratory, in beyond angiography, intravascular ultrasound, state of the art. *Congress of the ESC*, 1998.

[40] S. Kichenassamy, A. Kumar, P.J. Olver, A. Tannenbaum, and A.J. Yezzi. Gradient flows and geometric active contour models. *International Conference on Computer Vision (ICCV)*, pages 810–815, 1995.

[41] J.D. Klingensmith, D.G. Vince, B.D. Kuban, R. Shekhar, E.M. Tuzcu, S.E. Nissen, and J.F. Cornhill. Assessment of coronary compensatory enlargement by three-dimensional intravascular ultrasound. *International Journal of Cardiovascular Imaging*, 16:87–98, 2000.

[42] F.D. Kolodgie, A.P. Burke, A. Farb, H.K. Gold, J. Yuan, J. Narula, A.V. Finn, and R. Virmani. The thin-cap fibroatheroma: a type of vulnerable plaque: the major precursor lesion to acute coronary syndromes. *Current Opinion in Cardiology*, 16:285–292, 2001.

[43] A. König, M.P. Margolis, R. Virmani, D. Holmes, and V. Klauss. Technology insight: in vivo coronary plaque classification by intravascular ultrasonography radiofrequency analysis. *Cardiovascular Medicine*, 5(4):219–229, 2008.

[44] G. Kovalski, R. Beyar, R. Shofti, and H. Azhari. Three-dimensional automatic quantitative analysis of intravascular ultrasound images. *Ultrasound in Medicine and Biology*, 26:527–537, 2000.

[45] J. Lau, D. Kent, A. Tatsioni, Y. Sun, CH. Wang, P. Chew, B. Kupelnick, and H. Jordan. *Vulnerable Plaques: A Brief Review of the Concept and Proposed Approaches to Diagnosis and Treatment*. Agency for Healthcare Research and Quality, 2004.

[46] H. Liang, Y. Zhu, and M. Friedman. Ivus image segmentation based on contrast. *Medical Imaging conference*, 4684:1727–1733, 2002.

[47] F.L. Lizzi, M. Astor, E.J. Feleppa, M. Shao, and A. Kalisz. Statistical framework for ultrasonic spectral parameter imaging. *Ultrasound in Medicine and Biology*, 23:1371–1382, 1997.

[48] F.L. Lizzi, M. Greenebaum, E.J. Feleppa, and D.J. Coleman. Theoretical framework for spectrum analysis in ultrasonic tissue characterization. *The Journal of the Acoustical Society of America*, 73:1366–1373, 1983.

[49] Z. Luo, Y. Wang, and W. Wang. Estimating coronary artery lumen area with optimization based contour detection. *IEEE Transactions on Medical Imaging*, 4(22):564–56, 2003.

[50] R. Malladi, J.A. Sethian, and B.C. Vemuri. Shape modeling with front propagation: A level set approach. *IEEE Transactions on Pattern Analysis and Machine Intelligence*, 17(2):158–175, 1995.

[51] C. D. Mario, S. Madretsma, D. Linker, S.H.K. The, N. Bom, P.W.J.C Serruys, E.J. Gussenhoven, and J.R.T.C. Roelandt. The angle of incidence of the ultrasonic beam, a critical factor for the image quality in intravascular ultrasonography. *The American Heart Journal*, 125:442–448, 1993.

[52] O.V. Michailovich and A. Tannenbaum. Despeckling of medical ultrasound images. *IEEE transactions on ultrasonics, ferroelectrics and frequency control*, 53(1):64–78, 2006.

[53] G.S. Mintz, S.E. Nissen, W.D. Anderson, S.R. Bailey, R. Erbel, P.J. Fitzgerald, F.J. Pinto, K. Rosenfield, R.J. Siegel, E.M. Tuzcu, and P.G. Yock. Clinical expert consensus document on standards for acquisition, measurement and reporting of intravascular ultrasound studies (ivus). *Journal of the American College of Cardiology*, 37:1479–1491, 2001.

[54] A. Murashige, T. Hiro, T. Fujii, K. Imoto, T. Murata, Y. Fukumoto, and M. Matsuzaki. Detection of lipid-laden atherosclerotic plaque by wavelet analysis of radiofrequency intravascular ultrasound signals: In vitro validation and preliminary in vivo application. *Journal of American College of Cardiology*, 45(12):1954–1960, 2005.

[55] A. Nair, D. Calvetti, and D.G. Vince. Regularized autoregressive analysis of intravascular ultrasound backscatter: Improvement in spatial accuracy of tissue maps. *IEEE Transactions on Ultrasonics, Ferroelectrics and Frequency Control*, 51(4):420–431, 2004.

[56] A. Nair, B.D. Kuban, N. Obuchowski, and D.G. Vince. Assessing spectral algorithms to predict atherosclerotic plaque composition with normalized and raw intravascular ultrsound data. *Ultrasound in Medicine and Biology*, 27, 2001.

[57] A. Nair, B.D. Kuban, E.M. Tuzcu, P. Schoenhagen, S.E. Nissen, and D.G. Vince. Coronary plaque classification with intravascular ultrasound radiofrequency data analysis. *Circulation*, 106:2200–2206, 2002.

[58] A. Nair, M. P. Margolis, B.D. Kuban, and D. G. Vince. Automated coronary plaque characterization with intravascular ultrasound backscatter: ex-vivo validation. *EuroIntervention*, 3:113–120, 2007.

[59] G.P. Nason and B.W. Silverman. The stationary wavelet transform and some statistical applications. 35:281–300, 1995.

[60] K. Nasu, E. Tsuchikane, O. Katoh, D.G. Vince, R. Virmani, J.F. Surmely, A. Murata, Y. Takeda, T. Ito, M. Ehara, T. Matsubara, M. Terashima, and T. Suzuki. Accuracy of in vivo coronary plaque morphology assessment: A validation study of in vivo virtual histology compared with in vitro histopathology. *Journal of the American College of Cardiology*, 47(12):2405–2412, 2006.

[61] S.E. Nissen and P. Yock. Intravascular ultrasound, novel pathophysiological insights and current clinical applications. *Circulation*, pages 604–616, 2001.

[62] T. Ojala, M. Pietikainen, and T. Maenpaa. Multiresolution gray-scale and rotation invariant texture classification with local binary patterns. *IEEE Transactions Pattern Analysis and Machine Intelligence*, 24(7):971–987, 2002.

[63] M. Okubo, M. Kawasaki, Y. Ishihara, U. Takeyama, T. Kubota, T. Yamaki, S. Ojio, K. Nishigaki, G. Takemura, M. Saio, T. Takami, S. Minatoguchi, and H. Fujiwara. Development of integrated backscatter intravascular ultrasound for tissue characterizationof coronary plaques. *Ultrasound in Med. and Biol*, 34(4):655–663, 2008.

[64] M. Okubo, M. Kawasaki, Y. Ishihara, U. Takeyama, S. Yasuda, T. Kubota, S. Tanaka, T. Yamaki, S. Ojio, K. Nishigaki, G. Takemura, M. Saio, T. Takami, H. Fujiwara, , and S. Minatoguchi. Tissue characterization of coronary plaques: Comparison of integrated backscatter intravascular ultrasound with virtual histology intravascular ultrasound. *Circulation Journal*, 72, 2008.

[65] M.E. Olszewski, A. Wahle, S.C. Mitchell, and M. Sonka. Segmentation of intravascular ultrasound images, a machine learning approach mimicking human vision. *International Congress Series*, 1268:1045–1049, 2004.

[66] S.M. OMalley, S.G. Carlier, M. Naghavi, and I.A. Kakadiaris. Image-based frame gating of ivus pullbacks, a surrogate for ecg. *ICASSP*, 1:l–433–l–436, 2007.

[67] M. Papadogiorgaki, V. Mezaris, Y.S. Chatzizisis, I. Kompatsiaris, and G.D. Giannoglou. A fully automated texture-based approach for the segmentation of sequential ivus images. *International Conference on Systems, Signals and Image Processing*, 8(2):461–464, 2006.

[68] P. Patwari, N.J. Weissman, S.A. Boppart, CH. Jesser, D. Stamper, J.G. Fujimoto, and M.E. Brezinski. Assessment of coronary plaque with optical coherence tomography and high frequency ultrasound. *The American Journal of Cardiology*, 85:641–644, 2000.

[69] M.E. Plissiti, D.I. Fotiadis, L.K. Michalis, and G.E. Bozios. An automated method for lumen and media-adventitia border detection in a sequence of ivus frames. *IEEE Transactions on Information Technology in Biomedicine*, 8(2):131–141, 2004.

[70] E. Regar, J.A. Schaar, R.L. Wilensky, E. McFadden, W.J. van der Giessen, P. de Feyter, and P.W. Serruys. Invasive detection, quantification and monitoring of plaque vulnerability: methods and implications for upcoming clinical trials. *Euro PCR*, 2004.

[71] J. Rieber, O. Meissner, G. Babaryka, S. Reim, M. Oswald, A. Koenig, T.M. Schiele, M. Shapiro, K. Theisen, M.F. Reiser, V. Klauss, and U. Hoffmann.

[72] G.A. Rodriguez-Granillo, E.P. McFadden, M. Valgimigli, C.A. Van Mieghem, E. Regar, P.J. De Feyter, and P.W. Serruys. Coronary plaque composition of nonculprit lesions, assessed by in vivo intracoronary ultrasound radio frequency data analysis, is related to clinical presentation. *The American Heart Journal*, 151(5):1020–1024, 2006.

[73] A. Roodaki, A. Taki, S.K. Setarehdan, and N. Navab. Modified wavelet transform features for characterizing different plaque types in ivus images; a feasibility study. *9th International Conference on Signal Processing(ICSP)*, pages 789 – 792, 2008.

[74] M. Rosales and P. Radeva. *Handbook of Biomedical Image Analysis: A basic model for IVUS image simulation*. Springer, 2006.

[75] F.J.R. Sales, J.L.A.A. Falcao, B.A.A. Falcao, S.S. Furuie, and P.A. Lemos. Estimation of coronary atherosclerotic plaque composition based only on gray scale intravascular ultrasound images. *Computers in Cardiology*, 2009.

[76] F.J.R. Sales, J.L.A.A. Falcao, B.A.A. Falcao, P.A. Lemos, and S.S. Furuie. Evidences of possible necrotic-core artifact around dense calcium in virtual histology images. *Computers in Cardiology*, 35:545–548, 2008.

[77] E. Dos Santos, M. Yoshizawa, A. Tanaka, Y. Saijo, and T. Iwamoto. Detection of luminal contour using fuzzy clustering and mathematical morphology in intravascular ultrasound images. *Annual International Conference of the IEEE Engineering in Medicine and Biology (EMBS)*, pages 3471–3474, 2005.

[78] G. Sapiro and A. Tannenbaum. Affine invariant scale-space. *International Journal of Computer Vision*, 11(1):25–44, 1993.

[79] O. Sertel, J. Kong, H. Shimada, U. Catalyurek, J. Saltz, and M. Gurcan. Computer-aided prognosis of neuroblastoma on whole-slide images: Classification of stromal development. *SPIE Medical Imaging*, 2008.

[80] A. Sethian. *Level Set Methods and Fast Matching Methods: Evolving Interfaces in Computational Geometry, Fluid Mechanics, Computer Vision, and Material Science*. Cambridge University Press, 2nd edition, 1999.

[81] K. Siddiqi, Y.B. Lauziere, A. Tannenbaum, and S.W. Zucker. Area and length minimizing flows for shape segmentation. *IEEE Transactions on Image Processing*, 7:433–443, 1998.

[82] L. Sorensen, S.B. Shaker, and M. de Bruijne. Texture classification in lung ct using local binary patterns. *Medical Image Computing and Computer-Assisted Intervention(MICCAI)*, pages 934–941, 2008.

[83] X. Tang. Texture information in run length matrices. *IEEE Transactions on Image Processing*, 7(11):1602–1609, 1998.

[84] D. Terzopoulos. On matching deformable models to images. *Topical Meeting on Machine Vision, Technical Digest Series*, 12:160–167, 1987.

[85] S. Theodoridis and K. Koutroumbas. *Pattern Recognition*. Elsevier Academic Press, 5th edition, 2006.

[86] A. Thrush and T. Hartshorne. *Peripheral Vascular Ultrasound How, Why and When*. ELSEVIER, 2nd edition, 2005.

[87] E. J. Topol. *Textbook of Cardiovascular Medicine*. Lippincott Williams & Wilkins, 3rd edition, 2007.

[88] G. Unal, S. Bucher, S. Carlier, G. Slabaugh, T. Fang, and K. Tanaka. Shape driven segmentation of the arterial wall in intravascular ultrasound images. *IEEE Transactions on Information Technology in Biomedicine*, 12(3):335–347, 2008.

[89] O.P. Vila. A semi-supervised statistical framework and generative snakes for ivus analysis. *Graficas Rey*, 2004.

[90] D.G. Vince, K.J. Dixon, R.M. Cothren, and J.F. Cornhill. Comparison of texture analysis methods for the characterization of coronary plaques in intravascular ultrasound images. *Journal of Computerized Medical Imaging and Graphics*, 24:221–229, 2000.

[91] R. Virmani, A.P. Burke, A. Farb, and F.D. Kolodgie. Pathology of the unstable plaque. *Progress in Cardiovascular Diseases*, 44(5):349–356, 2002.

[92] R. Virmani, A.P. Burke, A. Farb, and F.D. Kolodgie. Pathology of the vulnerable plaque. *Journal of the American College of Cardiology*, 47(8):c13–c18, 2006.

[93] R. Virmani, F.D. Kolodgie, A.P. Burke, A. Farb, and S.M. Schwartz. Lessons from sudden coronary death a comprehensive morphological classification scheme for atherosclerotic lesions. *Arteriosclerosis, Thrombosis, and Vascular Biology.*, 20:1262–1275, 2000.

[94] H. Wang and B. Ghosh. Geometric active deformable models in shape modeling. *IEEE Transactions on Image Processing*, 9(2):302–308, 2000.

[95] M. Welling. Fisher linear discriminant analysis. *Class notes, Department of Computer Science, University of Toronto*, 2007.

[96] G.W. Williams. Comparing the joint agreement of several raters with another rater. *Biometrics*, 32:619–627, 1976.

[97] D.J. Withey and Z.J. Koles. Three generations of medical image segmentation: methods and available software. *The 6th International Symposium on Biomedical Imaging*, pages 140–143, 2007.

[98] www.americanheart.org.

[99] www.heartpoint.com/coronarteries.html.

[100] www.volcanocorp.com.

[101] C. Xu, D.L. Pham, and J.L. Prince. *SPIE handbook of Medical imaging. Medical image processing and analysis*. SPIE press, 2000.

[102] C.H. Yian-Leng and L. Xiaobo. Adaptive image region-growing. *IEEE Transactions on Image Processing*, 3(6):868–872, 1994.

[103] X. Zhang, C.R. McKay, and M. Sonka. Tissue characterization in intravascular ultrasound images. *IEEE Transactions on Medical Imaging*, 17(6):889–899, 1998.